Energy regime of the geodynamo during the Cretaceous Normal Superchron via paleosecular variation and paleointensity

Julia Maria Kollofrath

München 2012

Energy regime of the geodynamo during the Cretaceous Normal Superchron via paleosecular variation and paleointensity

Julia Maria Kollofrath

Dissertation
an der Fakultät für Geowissenschaften
der Ludwig–Maximilians–Universität
München

vorgelegt von
Julia Maria Kollofrath
aus Ichenhausen

München, den 28. Februar 2012

Erstgutachter: Prof. Stuart Gilder
Zweitgutachter: Prof. Erwin Appel
Tag der mündlichen Prüfung: 15. Juni 2012

Bestimmt liegt das an der übermächtigen Magnetosphäre Spitzbergens, denn hier treibt sich der Magnetpol herum, stets ruhelos und auf Wanderschaft, weil er weiß, dass er gar nicht hierher gehört: Wissenschaftlich gesehen ist er nämlich der Südpol.

Herbert Feuerstein, "Das Logbuch einer Kreuzfahrt ins Eismeer" in "Feuersteins Drittes"

Summary

The Earth's magnetic field underwent hundreds of reversals during its history. But within a ∼40 Myr span (84-125 Ma) during the Cretaceous no reversal happened. For comparison, the second longest chron length during the last 167 Ma is ∼5 Myr. Thus, the ∼40 Myr long chron is known as a superchron and is called Cretaceous Normal Superchron (CNS). Two other superchrons are now established: the Permian-Carboniferous Reversed Superchron and the Ordovician Reversed Superchron.

Why do these superchrons exist? Are they an extreme chron duration of the same statistical distribution? Or, do superchrons reflect a distinct dynamo regime separate from an oft-reversing regime. Are the onset and end of superchrons triggered by changes in the physical conditions of outer core convection? For example, instabilities within the convection in the outer core are suspected to trigger reversals. A 'low energy' geodynamo during the superchron could stem from less turbulent convection. But also the concept of a 'high energy' geodynamo during a superchron is conceivable: stronger convection would stabilize the field and increase the field intensity. These different dynamo regimes could be be triggered by changing the temperature conditions at the core mantle boundary (CMB), for example with the eruption of deep mantle plumes or the descent of cold material such as subducted slabs.

Insights into past geodynamo regimes can be learned primarily from two paleomagnetic methods: paleosecular variation (variation in field directions) and paleointensity. For the former, we collected 534 samples for a paleosecular variation study from a 1400 m-long, paleontologically well-described section in northern Peru. Thermal demagnetization isolates stable magnetization directions carried by greigite. Arguments are equivocal whether this remanence is syn-diagenetic, acquired during the Cretaceous normal superchron, or a secondary overprint, acquired during a chron of solely normal polarity in the upper Cenozoic, yet pre-Bruhnes (>800 kyr). We explore the ramifications on the S value, which quantifies paleosecular variation, that arises from directional analysis, sun compass correc-

tion, bedding correction, sampling frequency, outlying directions and different recording media. The sum of these affects can readily raise the S value by more than 20%. S values from northern Peru are indistinguishable from other S values for the Cretaceous normal superchron as well as those for the last 5 Ma. Summing over all the potential uncertainties, we come to the pessimistic conclusion that the S value is an unsuitable parameter to constrain geodynamo models. Alternatively, no statistical difference in paleosecular variation exists during much of the Cretaceous normal superchron and during the last 5 Ma.

Even though the S value might be unsuitable, we wanted to understand why the S value is latitude dependent. The origin of this latitude dependency is widely attributed to a combination of time-varying dipole and non-dipole components. The slope and magnitude of $S(\lambda)$ are taken as a basis to understand the geomagnetic field and its evolution. Here we show that $S(\lambda)$ stems from a mathematical aberration of the conversion from directions to poles, hence directional populations better quantify local estimates of paleosecular variation. Of the various options, k is likely the best choice, and the uncertainty on k(N) was already worked out.

As we came to the pessimistic conclusion that the S value might not be the best parameter to quantify the 'energy state' of the geodynamo during a superchron, we also carried out a paleointensity study on 128 samples from volcanic rocks in Northern Peru and Ecuador. Oxidation of the remanence carriers was a problem. Only one site gave reliable results. Two methods of paleointensity determination were applied to these rocks. The results of both methods agree quite well with each other and also with previous studies from other sites. Our results suggest that the field intensity towards the end of the superchron seems to quite similar to today's magnetic moment. Thus, it can be concluded that the 'energy state' of the geodynamo was not substantially different during the Cretaceous Normal Superchron compared to reversing times.

Why do superchrons exist? One possible explanation is that paleomagnetism is not able to resolve different energy states of the geodynamo, neither with paleosecular variation nor with paleointensity. This was suggested by some dynamo simulations in which the heat flux across the core-mantle boundary was kept the same, but the resulting paleosecular variation, paleointensity and frequency of reversals differed a lot. Another possible explanation is that a superchron is an intrinsic feature of the distribution of magnetic polarity chron lengths. Thus, no changes of the convection in the outer core are needed to trigger a superchron.

Contents

1 Introduction

First observations of the Earth's magnetic field date back to the 2^{nd} or 1^{st} century B.C., when the compass was invented during the Chinese Han Dynasty. But until first systematic observations published by William Gilbert in his book *De Magnete* in 1628 the concept of a Earth's magnetic field was unknown. Gilbert also discovered the dipolar nature of this field, which is equivalent to a permanent magnet in the Earth's interior. The origin of this field was tentatively explained by differential rotation effect (Inglis, 1955), Hall effect (Vestine, 1954) or electromagnetic inductions by magnetic storms (Chatterjee, 1956) until the relatively recent geodynamo theory (Larmor, 1919; Elsasser, 1946; Bullard and Gellman, 1954) was widely accepted. Bullard also introduced the disk dynamo as a simple model with the Earth's outer core as a generator of a magnetic field.

Geodynamo theory requires a moving electrically conductive fluid. Based on iron meteorites, geochemists argued that the core, both inner and outer, consists of iron with 4% nickel. A lower density than expected for Fe and Ni signifies to the presence of some lighter elements (H, He, O, S, Mg and Si). As the Earth's outer core is a barrier for seismological shear waves it has to be liquid, while the inner core is composed of solid iron and grows with time (Labrosse *et al.*, 2001). Thermal convection induced by initial heat, latent crystallization heat, tidal friction and/or radioactive decay together with compositional convection forces the liquid iron in the outer core to move and thus create a magnetic field.

The Earth's magnetic field (EMF) is not stable but underwent hundreds of reversals during it's history. The frequency of these reversals is not constant, e.g. in the Jurassic the reversal rate was as high as 7 reversals per Myr (Pavlov and Gallet, 2005), while shortly after during the Cretaceous (84-125 Ma) no reversal happened for about 40 Myr, a time which is known as the Cretaceous Normal Superchron (CNS). This chron duration of ∼40 Myr seems to be remarkably longer than any other chron duration. The mean chron duration during the last 167 Ma (chron durations from oceanic magnetic anomalies in Gradstein *et al.*, 2004) was 0.2 Myr, the longest chron disregarding the Cretaceous Normal Superchron is ∼5 Myr long. Apart from this Cretaceous superchron two other superchrons were found later on: the Permian-Carboniferous Reversed Superchron (also known as Kiaman superchron) and the Ordovician Reversed Superchron (also known as Moyero Superchron Pavlov and Gallet, 2005). Their durations are more difficult to estimate, as they can only be found in continental rocks with a noncontinuous recording, while the CNS is continuously recorded in seafloor anomalies.

Why do these superchrons exist? Are they just an extreme chron duration of the same statistical distribution? Or are superchrons reflecting a distinct dynamo regime resulting in a more stable field, and is the onset and end of superchrons triggered by changes in the physical conditions of the outer core convection? Instabilities within the convection in the outer core are suspected to trigger reversals. Thus, a 'low energy' geodynamo during the superchron would stem from a less turbulent convection (Loper and McCartney, 1986). But also the concept of a 'high energy' geodynamo during a superchron is conceivable: a stronger convection would stabilize the field and increase the field intensity – in this model reversal triggering instabilities would be a result of a too weak geodynamo (Larson and Olson, 1991). These different dynamo regimes could be be triggered by changing the conditions at the core mantle boundary (CMB), for example with the eruption of deep mantle plumes (Loper and McCartney, 1986; Larson and Olson, 1991) or the descent of cold material (Hulot and Gallet, 2003) such as subducted slabs (Gallet and Hulot, 1997; Eide and Torsvik, 1996). CMB heat flux increases have been causally linked to changes of thermal mantle structure, as there are roughly common timescales of these changes and the length of superchrons (Glatzmaier *et al.*, 1999). In mantle convection models faster plate velocities at the surface were shown to precede an increased heat flux across the core-mantle boundary, when the subducted material begins to arrive at the base of the mantle (Buffett, 2007). Also, the production of ocean crust caused by hypothetical superplumes was correlated to the occurrence of superchrons (Larson and Olson, 1991). To compensate for this heat loss core convection increases and the reversal frequency

decreases until preexisting temperature gradients are reestablished (Larson and Olson, 1991). Also perturbations of the core convection caused by cold material sinking from the CMB and/or hot material rising from the inner core - outer core boundary (IOCB) can affect the geodynamo (McFadden and Merrill, 1986). This model implies a stable occasionally reversing regime and a perturbed uniform-polarity regime of the geodynamo.

Unlike other disciplines in geophysics like seismology for example, which can only take a snapshot of the today's state of the Earth outer core and core mantle boundary, paleomagnetism offers the chance to examine the past state of the IOCB and CMB. Insights into past geodynamo regimes can be gained by two paleomagnetic methods: the variations in field directions (i.e. paleosecular variation, Jackson and Bloxham, 1991) and paleointensity.

Rocks generally acquire a stable remanent magnetization (NRM) that is parallel to the prevalent direction of the geomagnetic field during their formation. Because of slow variations of the geomagnetic field, called secular variations, NRMs from the same rock formation with only slightly different ages might not be exactly parallel to each other. For this reason, and because of dating uncertainties, rocks of nominally same age taken from the same site might carry NRMs with different intensities and directions. Also today the magnetic north pole (dip pole) does not coincide with the geographic north pole (rotation axis), but is found northwest of the Canadian Arctic Archipelago and is moving with a velocity of 40 km per year northwestward. This change might seem rapid compared to human time scale; however, it only represents a small wiggle in the in the overall, long-term wobbling of the magnetic North Pole around the geographic North Pole in several thousand years (Butler, 1998). Because of the random nature of such wobbling, and in general of all non-axial dipole components of the geomagnetic field, averages of the field over sufficiently long periods (>10 kyr, Creer, 1962) result in a purely axial dipole field with magnetic poles coinciding with the Earth's rotation axis.

Modern time records of the geomagnetic field are performed by a network of geomagnetic observatories that cover continents, predominantly in the Northern hemisphere. Currently 128 magnetic observatories take part in the INTERMAGNET network, which provides data to model the Earth's magnetic field. Observatory records of the Earth's magnetic field of the last 200 years reveal a change in e.g. declination by 15° in Germany (Korte *et al.*, 2009).

The record before observatory times relies exclusively on rocks and pottery from archeological sites. The latter is based on the stable NRM acquired by pottery and kilns during firing, and covers the last ∼3 kyr. Records from older times rely exclusively on rocks containing magnetic minerals capable of preserving the

remanent magnetization acquired during their formation against later geological events (e.g. metamorphism) and lightning. Unfortunately, suitable outcrops are limited and unevenly distributed over the continents, especially in the case of very ancient rocks. Therefore the distribution of paleomagnetic information for a given time is very sparse and insufficient for a detailed reconstruction of the geomagnetic field, as it is possible with magnetic observatories. Additional uncertainties are added by the limited precision in the reconstruction of continental wandering.

A complete description of secular variation requires the knowledge of intensity and direction of the geomagnetic field at any point of globe. This is done by interpolating observatory field measurements with spherical harmonic functions. The coefficients of these functions, called Gauss-Schmidt coefficients g_l^m and h_l^m quantify the contributions of every spherical harmonic (e.g. axial dipole) to the total field. Spherical harmonics with an order $l = 0$ are physically interpreted ad axial dipole (g_1^0) or axial higher-pole (quadrupole g_2^0, etc.). Secular variations are expressed by the time derivative of coefficients with $l < 18$, while higher coefficients reflect crustal magnetization anomalies.

However, such an accurate reconstruction is not possible with paleomagnetic data for obvious reasons. Paleosecular variation is thus expressed by the dispersion of virtual geomagnetic poles (VGPs). A VGP is the location of a geomagnetic North poles calculated from the directions of a rock remanent magnetization from a given site for a given time, assuming that the geomagnetic field was that of a geocentric axial dipole (GAD). This inference is only sustainable if the paleomagnetic data cover a sufficiently long time (more than 10 kyr, see above)(Creer, 1962). The standard deviation of one pole

$$S = \sqrt{\frac{1}{N-1}\sum_{i=1}^{N}\Delta_i^2} \tag{1.1}$$

with respect to the VGP mean position is used as a index for paleosecular variation. In equation (1.1), N is the number of VGPs and Δ the angular distance between the individual VGP and the mean of the VGP distribution.

This S value is found to be latitude dependent (Fig. 1), meaning lower S values are observed near the equator than at the poles. McFadden *et al.* (1988) has explained the latitude dependency of S as the combined effect of two so-called geodynamo families.

As mentioned above the Earth's magnetic field can be described with spherical harmonics expressed by Gauss-Schmidt coefficients g_l^m and h_l^m of various orders l and degrees m. An axial dipole or octupole is asymmetric with respect to

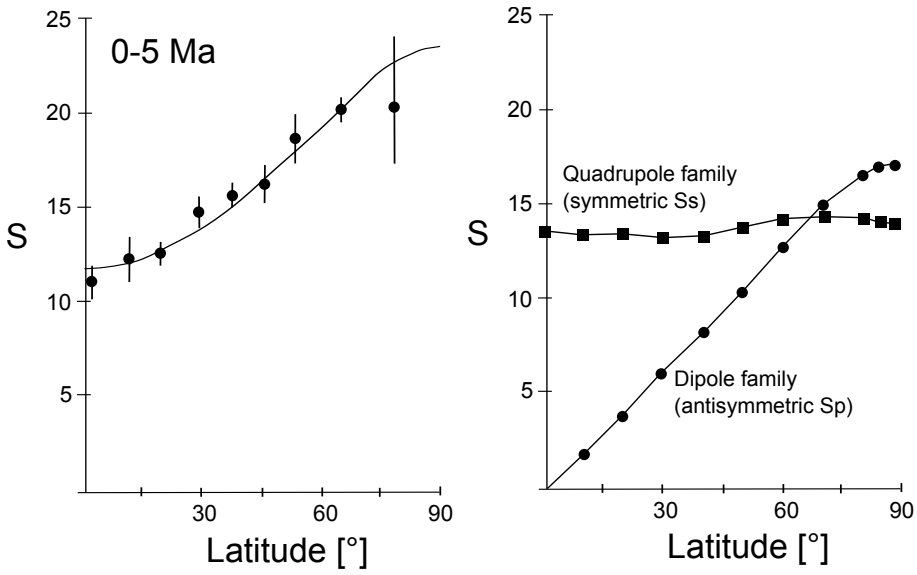

Figure 1.1: Left side: Paleosecular variation described by the S value for the last 5 Myr after McElhinny and Merrill (1975). Right side: S value or VGP scatter for IGRF65 separated into the contributions from the quadrupole family (solid squares) and the dipole family (solid circles) after McFadden *et al.* (1988).

the equator. This asymmetric geodynamo family consists of spherical harmonics with odd m+l and is also called primary or dipole family named after the most important spherical harmonic in this family. The other geodynamo family consists of symmetric spherical harmonics for which m+l is even, e.g. the axial quadrupole, also called secondary or quadrupole family. Paleosecular variation created by the by the asymmetric dipole family is expected to produce a latitude dependent S value, called S_p, which is zero at the equator and the highest at the poles (Fig. 1). On the other hand, paleosecular variation of the symmetric quadrupole family is expected to produce a latitude independent S value called S_s.

The slope of the S value with latitude is not constant with time (Fig. 1.2). During the last 200 Ma the contribution S_p/λ of the asymmetric geodynamo family was found to be higher at 80-100 Ma (about the time of the Cretaceous Normal Superchron) than compared to reversing times such as the last 5 Ma (McFadden *et al.*, 1991). This results in a steeper slope during the superchron than in reversing times. Correspondingly, the equatorial S value S_s was found to be lower during the superchron.

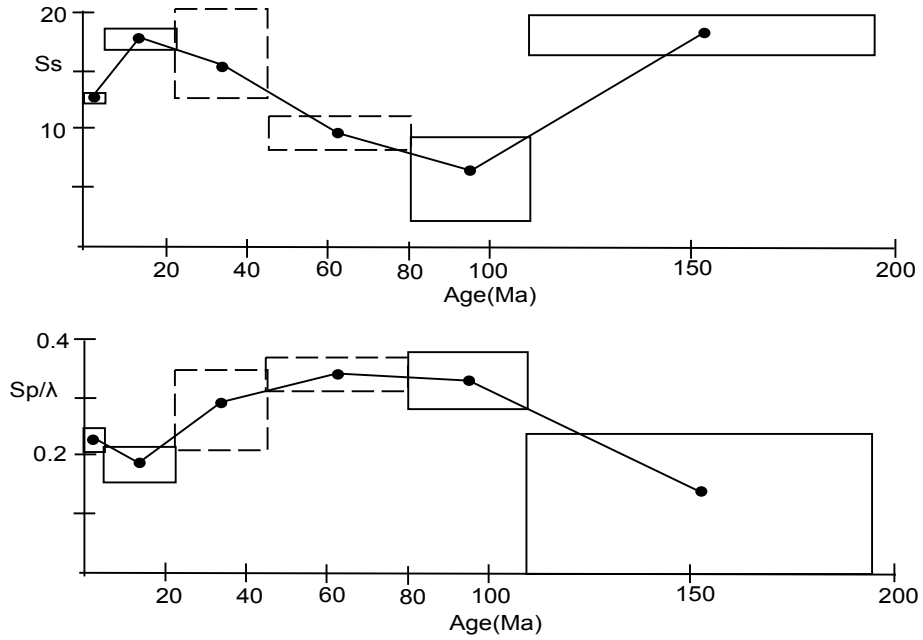

Figure 1.2: Variation of Ss and Sp/ from the present back to 190 Ma after McFadden *et al.* (1991). The boxes around the plotted points indicate the range of ages contributing to the estimated parameter and the 95% confidence limits on the estimate. A solid box indicates that the fit was acceptable and a dotted box indicate that the fit was not acceptable.

Paleosecular studies during the Cretaceous Normal Superchron were done on sediments (e.g. Cronin *et al.*, 2001) and volcanics (e.g. Tarduno *et al.*, 2001). Apart from the rock type, also the age within the superchron (85-89.5 Ma and ∼103 Ma), the length of the time sampled (4.5 Myr and not well known) and the latitude (about 20° and 40°) are different in these two studies and make the two S values of 9.9 and 11.7 basically incomparable.

We want to determine paleosecular variation from an equatorial site. This value will then be independent from the slope of the S-value and represent the minimum VGP scatter for all latitudes at a given time. Such equatorial records exist for the Permian Reversed Superchron (Kruiver *et al.*, 2002; Haldan *et al.*, 2009), but not for the Cretaceous Normal Superchron.

We chose a sedimentary section in Peru for our study of paleosecular variation, as Northern Peru was right at the equator during the Cretaceous Normal Superchron. Nearby in Northern Peru and Ecuador we also sampled contempo-

raneous volcanic formations for paleointensities to accomplish our record of the 'energy state' of the geodynamo in the Cretaceous Normal Superchron. Same as expected for the S value quantifying paleosecular variation, also paleointensity is to be minimum at the equator. A higher or lower energy state of the geodynamo should be reflected in a higher or lower paleointensity during the Cretaceous Normal Superchron. How paleointensity and paleosecular variation are connected is still a subject of debate. The combined examination of paleosecular variation and paleointensity during the Cretaceous Normal Superchron in this study should help to determine the geodynamo regime during the CNS.

2 Geodynamo energy regime via paleosecular variation

2.1 PSV from equatorial sediments

This section 2.1 was published in the special issue *Planetary Magnetism, Dynamo and Dynamics* of *Physics of the Earth in Planetary Interiors* in August 2011 under the title *Geomagnetic secular variation recorded by sediments deposited during the Cretaceous normal superchron at low latitude* (Linder and Gilder, 2011, doi:10.1016/j.pepi.2011.05.010). Supplementary data is given in Table A.1 in Appendix A.

Abstract

Paleosecular variation of the Earth's magnetic field reflects the convective vigor of the geodynamo. To investigate the energy regime of the geodynamo during the Cretaceous normal superchron, we collected 534 samples for a paleosecular variation study from a 1400 m-long, paleontologically well-described section in northern Peru. Thermal demagnetization isolates stable magnetization directions carried by greigite. Arguments are equivocal whether this remanence is syndiagenetic, acquired during the Cretaceous normal superchron, or a secondary

overprint, acquired during a chron of solely normal polarity in the upper Cenozoic, yet pre-Bruhnes (>800 kyr). We explore the ramifications on the S value, which quantifies paleosecular variation, that arises from directional analysis, sun compass correction, bedding correction, sampling frequency, outlying directions and different recording media. The sum of these affects can readily raise the S value by more than 20%. S values from northern Peru are indistinguishable from other S values for the Cretaceous normal superchron as well as those for the last 5 Ma. Summing over all the potential uncertainties, we come to the pessimistic conclusion that the S value is an unsuitable parameter to constrain geodynamo models. Alternatively, no statistical difference in paleosecular variation exists during much of the Cretaceous normal superchron and during the last 5 Ma.

2.1.1 Introduction

Geomagnetic field reversals constitute one of Earth's most intriguing phenomena. That reversal frequency fluctuates through Earth's history is equally fascinating yet equally unexplained. Magnetic polarity reversals have occurred roughly five times per million years over the past five million years; however, the geologic record contains a few exceptionally long periods (> 30 Myr) of uniform geomagnetic polarity. Two of these so-called superchrons are well documented in the Phanerozoic: the Cretaceous normal superchron (CNS), which lasted from 124 Ma to 83 Ma, and the Permo-Carboniferous (Kiaman) reversed superchron, which lasted from 317 Ma to 265 Ma (Gradstein *et al.*, 2004; Menning *et al.*, 2006). A third superchron potentially exists within the Ordovician (Pavlov and Gallet, 2005). Just why the field remained so stable during these periods is hotly debated.

To better define the meaning of a superchron, we plotted the log-normal distribution of the magnetic chron durations over the last 167 Ma using the geomagnetic time scale of Gradstein *et al.* (2004) (Figure 2.1). Seen this way, field reversal frequency resembles a Gaussian distribution. The mean geomagnetic chron lasts for 0.17 Myr, close to the mean chron length of 0.2 Myr over the last 5 Myr. A slight skewness of the distribution toward longer chrons is likely an artifact of underrepresented short chrons, as they are harder to detect and date.

One chron, the CNS, lies more than four standard deviations away from the mean. The question arises whether this chron marks the end-member of a statistical distribution of polarity lengths (Jacobs, 2001; Hulot and Gallet, 2003; Fabian *et al.*, 2010) and is thus an intrinsic feature of the geodynamo, or whether the absence of chrons with durations between 6 and 41 Myr makes the CNS some-

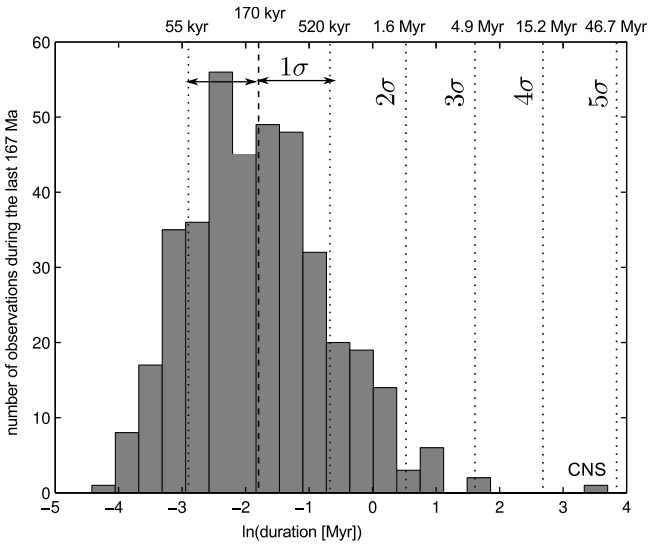

Figure 2.1: Semilogarithmic histogram of magnetic chron durations during the last 167 Ma. Also shown are the mean and the one to five standard deviations (σ) of this distribution converted into Myr. The Cretaceous normal superchron (CNS) lies more than 4σ away from the mean. The so-called ISEA chron (Vandenberg *et al.*, 1978) within the CNS was not considered as its existence remains uncertain. Including the ISEA-chron still results in a CNS farther than 4σ away from the mean duration.

how unique (McFadden and Merrill, 1986; Larson and Olson, 1991; McFadden and Merrill, 1995, 1997; Gallet and Hulot, 1997; Pavlov and Gallet, 2005). This latter scenario would suggest that two different energy regimes govern the Earth's magnetic field, with a superchron regime being independent of a reversing regime. If a so-called superchron is indeed distinct, then its definition should be defined as a chron of duration lying four or more standard deviations away from the mean, a definition which is also true for the Permo-Carboniferous and the Ordovician superchrons.

Most workers that describe superchrons as unique events agree that changes in the thermal structure at the core-mantle boundary are the cause. This is because changes in the heat flux at the core-mantle boundary occurs over plausible mantle convection rates (Larson, 1991; Glatzmaier *et al.*, 1999). A few potential mechanisms can account for these thermal, and hence geodynamo, perturbations at the core-mantle boundary. One can remove heat via mantle plumes (Loper and McCartney, 1986; Courtillot and Besse, 1987) or add cold, subducted lithosphere

(Eide and Torsvik, 1996; Gallet and Hulot, 1997). Alternatively, the origin may lie in the outer core itself due to stirring of the liquid iron by dense material sinking down from the core-mantle boundary or by less dense material rising from the inner core (McFadden and Merrill, 1986).

There are several theories explaining the core's activity during superchrons. The two end-member hypotheses are the high and low energy state, both stemming from different convection vigor during superchrons compared to times with frequent reversals. Larson and Olson (1991) proposed that enhanced core convection would stabilize the geodynamo and thus result in a superchron. This model predicts less variability of the geomagnetic field, and potentially higher field strength, during the superchron. On the other hand, Loper and McCartney (1986) argued that stronger core convection would generate chaotic flow, resulting in geomagnetic reversals. With this model, superchrons represent times of weaker core convection, characterized by greater variations in direction and potentially lower field intensity.

One way to resolve this problem is to study the variability of the geomagnetic field, called paleosecular variation, which measures the convecting state in the outer core and reflects the time constants of the geodynamo (Cox, 1975; Jackson and Bloxham, 1991; Bloxham and Gubbins, 1985). If paleosecular variation during a geomagnetic superchron is high, the low-energy state of the geodynamo is favored; less paleosecular variation would support a high-energy state. Paleosecular variation is accessible from paleomagnetism via the angular standard deviation of virtual geomagnetic poles, called the S-value, which is the mean angular distance Δ of the individual virtual geomagnetic poles away from the mean pole defined as

$$S = \sqrt{\frac{1}{N-1}\sum_{i=1}^{N}\Delta_i^2} \tag{2.1}$$

(Cox, 1970). Thus, in a given time window, high scatter reflects high geomagnetic activity while low S, low activity.

Interestingly, the S value is latitude-dependent, being about twice as high for sites near the geographic poles than near the equator. The cause of this latitude-dependency remains an open question, yet most workers evoke combinations of dipole and non-dipole components that vary in proportion, intensity and direction (Creer *et al.*, 1959; Irving and Ward, 1964; Cox, 1962, 1970; McElhinny and Merrill, 1975; McFadden and McElhinny, 1984; Constable and Parker, 1988; Harrison, 1995). McFadden *et al.* (1988) explained the latitude dependence by dividing the geomagnetic field into its spherical harmonic coefficients. They named the coeffi-

cients that are asymmetric about the equator (e.g., the axial dipole) the primary geodynamo family, and those that are symmetric about the equator (e.g., the axial quadrupole) the secondary geodynamo family. Contributions from the primary geodynamo family are latitude-dependent whereas contributions from the secondary family are constant over all latitudes. Thus, the secondary family serves as a baseline value for paleosecular variation at any specified time. S-values determined at the geomagnetic equator would therefore represent the minimum scatter for that specific time, which contributes to S at all latitudes. S values derived from equatorial latitudes can then be easily compared to values from other times without needing information to constrain the slope of S.

Theoretical work by Roberts and Stix (1972) showed that a violation of symmetry conditions having higher ratios of the secondary to primary geodynamo families forces the two geodynamo families to interact, which would increase the chance of a reversal to occur. They concluded that the relative contribution of the secondary geodynamo family to the total field is low when the reversal rate is low. To test the theoretical work of Roberts and Stix (1972), McFadden *et al.* (1991) used an unpublished dataset compiled in the PhD dissertation of Lee (1983) to calculate the contributions of the two geodynamo families to the S value in specific time windows over the past 200 Ma. During the Cretaceous normal superchron, they found a subdued contribution from the symmetric family and an enhanced contribution of the primary family. This means that equatorial sites should experience lower paleosecular variation, and thus lower S, during the CNS than any other time in the last 200 Ma. For this reason, we studied paleosecular variation at the geomagnetic equator within a ca. 23 Myr span of the Cretaceous normal superchron. To date, studies concentrating on paleosecular variation (PSV) during the CNS (e.g., Cronin *et al.*, 2001; Riisager *et al.*, 2001; Tarduno *et al.*, 2002; Biggin *et al.*, 2008b) have been carried out at middle and high latitudes, in sections whose average time span is 4 Myr.

2.1.2 Geology

Our samples come from a sequence of marine sediments in northern Peru (Figure 2.2). The Cretaceous tectonic setting there was dominated by a series of back-arc basins that formed near a subduction zone (Jaillard *et al.*, 1995; Jaillard, 1996a; Jaillard *et al.*, 2005). Relative sea-level fluctuations during Albian to Campanian times led to continuous deposition of marine sediments with variable terrigenous contribution in sections whose thicknesses range from 1000 to 3000 m (Benavides-Cáceres, 1956; Wilson, 1963; Macellari, 1988; Dhondt and Jaillard, 2005).

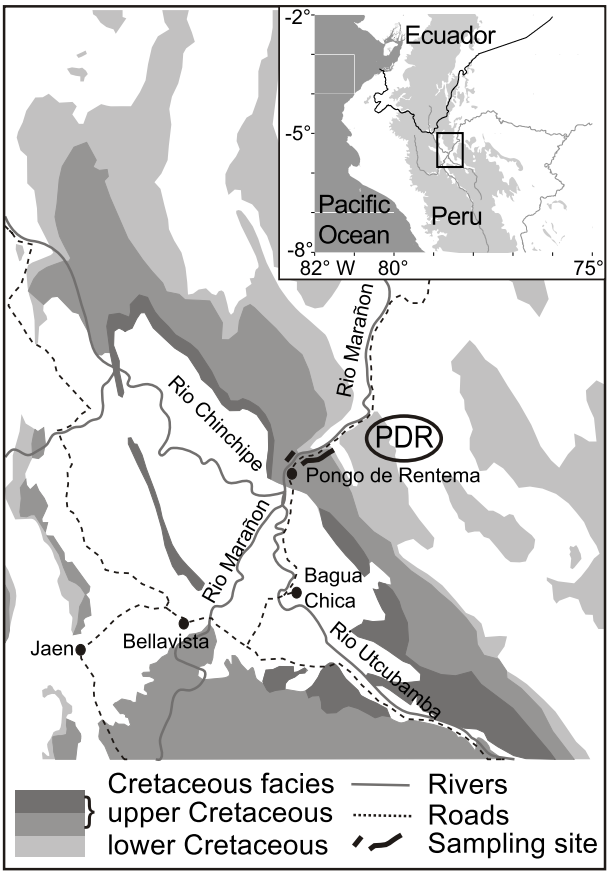

Figure 2.2: Insert: Location map of northern Peru and southern Ecuador. Gray shading represents topography higher than 1000 m. The box at the confluence of the three main rivers delineates the sampling region shown in the main figure. Main figure: Map showing the Pongo de Rentema section (bold black lines on both sides of the Rio Marañon). Light and dark gray shading denote Lower and Upper Cretaceous facies, respectively, (from de la Cruz Wetzell *et al.*, 1995; de la Cruz Wetzell and Leon Lacaros, 1995; Pilatsig *et al.*, 2008).

Samples were collected near the the village of Pongo de Rentema, along the road from Bagua Chica to Chiriaco/Santa Maria de Nieva, just north of the confluence between the Marañon, Chinchipe and Utcubamba rivers (Figure 2). Along this road, incision by the Rio Marañon exposed a fairly continuous series of southwest dipping, Late Jurassic to Paleocene rocks. Deformation of this section occurred after the Paleocene, and perhaps as recently as the upper to middle

Miocene (Rousse *et al.*, 2003). The base of our section (site PDR01, 5°29'22.11"S, 78°32'54.25"W) lies on the east side of the Rio Marañon. We sampled up-section (westward) to site PDR466 (5°29'47.35"S, 78°33'23.20"W), until we switched to the west side of the river at site PDR467 (5°29'41.00"S, 78°33'28.71"W) and continued sampling south-westwards until site PDR534 (5°29'52.98"S, 78°33'32.22"W). The stratigraphic thickness of our section is 1.4 km.

Fossils, found in abundance in this section, are described by Benavides-Cáceres (1956), Robert (2001), Dhondt and Jaillard (2005), Jaillard *et al.* (2005), Jaillard and Arnaud-Vanneau (1993) and Jaillard (1987). Paleontological age correlation mainly follows Robert (2001) and Robert *et al.* (2003) for the lower part of the section and Dhondt and Jaillard (2005) for the upper part. The lowest horizon we sampled (site PDR01) corresponds to bed N° 72 in Robert (2001) (Figure 2.3) within the Chulec Formation, which consists of shallow marine limestone and marl (Jaillard, 1987). Sample PDR31 (bed N° 115 of Robert, 2001) marks the boundary between the Chulec and the overlying Pariatambo Formation and is also the boundary between the Peruvian Pseudolyelli and Ulrichi regional biostratigraphy stages at the transition between the lower and middle Albian (Robert, 2001; Robert *et al.*, 2003, and personal communication, 2009). Thus, PDR31 can be placed into absolute time at 108.8 Ma according to Gradstein *et al.* (2004) and is the best-dated horizon of the section.

Sites PDR31 and PDR395 enclose the Pariatambo, Yumagual and Mujarrun formations. The 52 m-thick Pariatambo Formation (PDR32- PDR76) consists of bituminous limestone and fossiliferous marls and directly overlies the Chulec Formation. Its upper boundary with the Yumagual Formation is identified by the onset of rhythmic bedding. This formation change lies within the Ulrichi biostratigraphic stage (Robert, 2001). The transition from the Yumagual to the Mujarrun formation at site PDR371 is marked by the onset of sand and silt-rich banks intercalating with limestone (Benavides-Cáceres, 1956). This boundary lies within the late Albian (Robert, 2001). Site PDR395 marks the limit between the Mujarrun and Romiron formations, which lies at the middle to late Cenomanian boundary (94.6 Ma) (Benavides-Cáceres, 1956). Thus, for the Pariatambo, Yumagual and Majuarrun formations, a mean sedimentation rate of 4.5 cm/kyr was calculated, which is reasonable for marine limestones and similar to the 5 cm/kyr sedimentation rate from 108 to 100 Ma measured by Jaillard (1996a). Extrapolating to the base of the section places the oldest sample at 109.7 Ma.

There is broad agreement in the published literature that the change from the Romiron to the Coñor formations lies at the Cenomanian to Turonian boundary (Macellari, 1988; Benavides-Cáceres, 1956; Dhondt and Jaillard, 2005; Jaillard

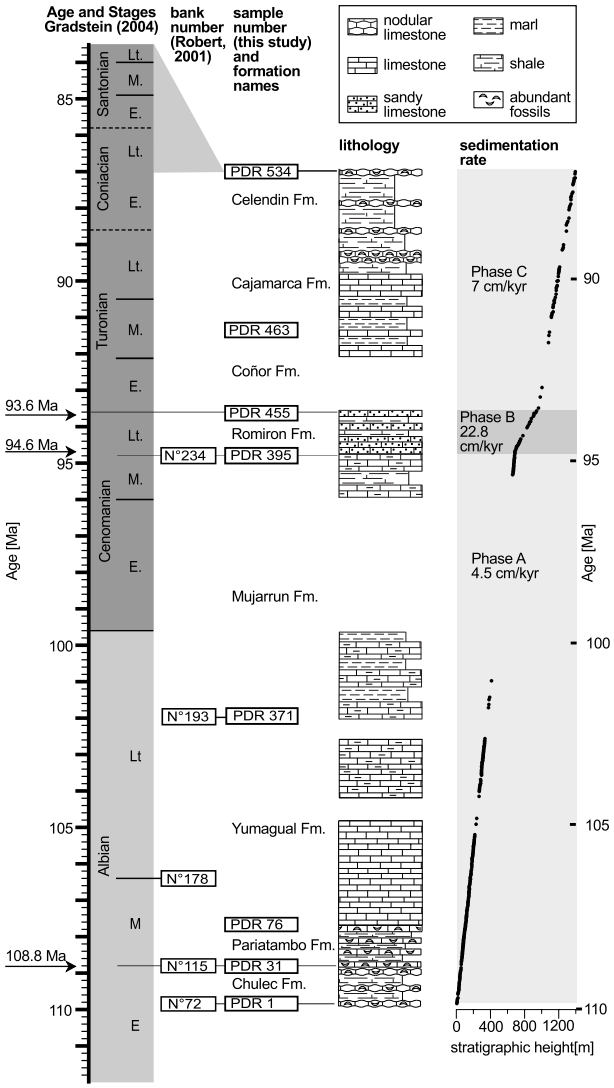

Figure 2.3: Log of the Pongo de Rentema section. Ages in millions of years and stages are based on the geologic time scale of Gradstein *et al.* (2004); the gray shades of the stage boxes corresponds to the gray shades in Figure 2.2. Sites that are directly correlated to a bed described in Robert (2001) or to an age on the time scale of Gradstein *et al.* (2004) are indicated with a straight black line. Also shown are the numbers of our sites that lay at formation boundaries (GPS coordinates of all samples are provided in Supplementary Data, Table 1) and a lithological log of the section. The plot to the right shows stratigraphic thickness versus age. Sedimentation rates, calculated from the interpolated parts of the section and extrapolated for sites below PDR31 and above PDR455, show three distinct phases. Phase A and C correspond to deeper water facies, while Phase B, marked by a higher sedimentation rate, is more marly.

et al., 2005), a stage boundary that is dated at 93.6 Ma (Gradstein *et al.*, 2004). This yields an average sedimentation rate of 22.7 cm/kyr for the Romiron Formation, which agrees well with the published sedimentation rate of 25 cm/kyr of Jaillard (1996a) and reflects the greater input of terriginous material. The Coñor Formation is conformably overlain by the Cajamarca Formation, which is in turn conformably overlain by the Celendin Formation. As the lithostratigraphy of these two latter formations is so similar (massive limestone to thinly bedded limestone), the distinction between them is ambiguous (Benavides-Cáceres, 1956; Dhondt and Jaillard, 2005; Jaillard *et al.*, 2005). We did not sample the Campanian-Maastrichtian Bagua Formation (Mourier *et al.*, 1988b), so our last site PDR534 lies well within the Celendin Formation. The section continues upwards but we stopped sampling as faulting made the stratigraphy uncertain. Since the Celedin Formation is clearly pre-Campanian, the youngest possible age for PDR534 is 83.6 Ma. Macellari (1988) and Jaillard *et al.* (2005) proposed the upper boundary of the Celendin Formation to be late Coniacian, thus the oldest possible age for PDR534 is 87 Ma. Based on these upper and lower bounds for the age of our youngest sample, the sedimentation rate for the upper part of the section thus varies between 5 cm/kyr and 7 cm/kyr. Because the upper part of the section has more continental detritus than the lower part, we favor the higher estimate of 7 cm/kyr, which places the youngest sample of our section PDR534 at 87.0 Ma. Our sampled sections thus spans 22.7 Myr of time from 109.7 to 87.0 Ma.

2.1.3 Methods

Sample collection and magnetization components

We drilled 534, 2.5 cm-diameter cores and oriented them using a homemade computerized system that also measures the local magnetic field vector and the GPS location at each core. Sun compass measurements were taken whenever possible. The average declination anomaly is $1.1^\circ \pm 3.7^\circ$ (N= 72) which compares well with that predicted by the international geomagnetic reference field (IGRF) (0.8°) at Pongo de Rentema. We applied the average declination anomaly to correct cores that did not have Sun compass measurements.

One sample per horizon was drilled with an average distance between each horizon of 2 m. Locally, the sampling density reaches as high as 18 samples per meter, while in other places gaps exist up to 255 m due to lack of outcrop. Higher sampling density was intentionally carried out to calculate S values under different time constants. Bedding dip directions and dips define a mean of 238.1°/58.6° (N= 82, the radius that the mean direction lies within 95% confidence $[\alpha_{95}]$=1.2°,

Figure 2.4). When cut into equal portions or using a running mean, bedding attitudes are identical within 95% confidence limits throughout the section. We conclude that the mean value is the best estimate for paleohorizontal, with individual bedding measurements reflecting slight irregularities in the ocean floor morphology, lithological inhomogeneities, etc. Thus, the bulk correction was applied in converting directional data from geographic to stratigraphic coordinates. This subtle point has a significant, yet mostly overlooked, impact on the calculation of scatter, as will be discussed below.

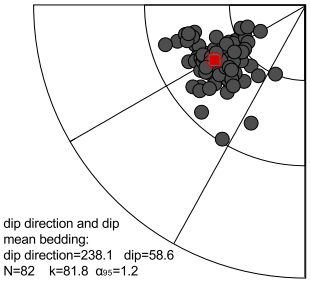

Figure 2.4: One stereonet quadrant with 82 measured dip and dip directions of the bedding planes from this study. The mean dip and dip direction is shown as a red square with a red α_{95} confidence ellipse.

One sample per core was thermally demagnetized over 13 steps using a Schonstedt oven (Figure 2.5). Magnetic remanence was measured with a 3-axis, 2G Enterprises cryogenic magnetometer. Both instruments are housed in a magnetically shielded room at the LMU-Munich paleomagnetic laboratory. The average natural remanent magnetization (20°C) intensity of the sediments is $6.17 \pm 8.61 \cdot 10^{-4} Am^{-1}$. The mean direction of declination (D) of 352.2° and inclination (I) of 15.0° (N= 534, α_{95}= 2.6°) lies close to the present day field direction at the site (D= 359.2°, I= 12.9°) and is likely a recent overprint (Figure 2.6a). For 104 samples (19%), magnetization directions were erratic upon progressive stepwise demagnetization (Figure 2.5 rejected), so best-fit line segments were not applied; this particularly concerns samples from the upper part of the section on the west side of the Rio Marañon. For the remaining 430 samples (81%) the mean direction of the natural remanent magnetization is D= 352.2° and I= 13.9° (α_{95}= 2.7°). Beginning above the first or second demagnetization step, magnetization directions move along great circle trajectories until 160°C, whereafter they reach a stable end-point direction that persists until ∼400°C (Figure 2.5 accepted). Magnetic susceptibility markedly increases above 430°C, which suggests magnetomineralogical alteration sets in. The magnetization component between ca. 200°C and 400°C trends univectorally toward the origin (Figure 2.5 accepted). Best-fit line segments were anchored to the origin for all steps in this temperature interval.

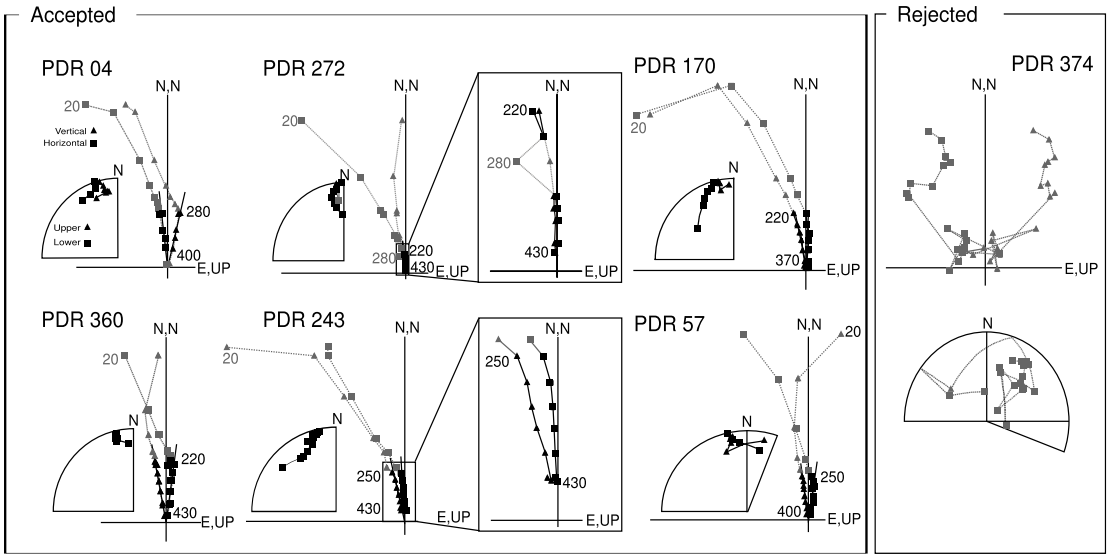

Figure 2.5: Orthogonal projections and corresponding stereonets of the thermal demagnetization experiments divided into accepted and rejected samples (in stratigraphic coordinates). Triangles represent vertical components, squares horizontal components. Demagnetization steps in degrees Celsius are given for the natural remanent (20°C) directions and the minimum and maximum temperature steps fit with line segments for the high temperature component in the principal component analysis routine (shown using black symbols and corresponding black lines). Steps not used for principal component analysis of the high temperature component are in gray. Unfilled triangles in the stereonet plots show the upper hemisphere and solid squares, the lower hemisphere.

The average in situ direction for the high temperature component lies at D= 336.5° and I= -17.6° (N= 430, α_{95}= 2.0°) (Figure 2.6b), significantly different at 95% confidence limits from the present day, geocentric axial dipole, or the mean of the natural remanent magnetization (20°C) directions. To test whether the high temperature magnetization component was contaminated by an unremoved overprint component, we compared the direction obtained from a single demagnetization step lying in the middle (300° or 310°C) of the temperature steps used to define the high temperature component (Figure 2.6c). If the high temperature component directions were contaminated by a recent viscous overprint, then one would expect a curvature in the directions from low to high temperatures. That the average directions defined by the single step and the high temperature component (Figure 2.6) are indistinguishable at 95% confidence limits (McFad-

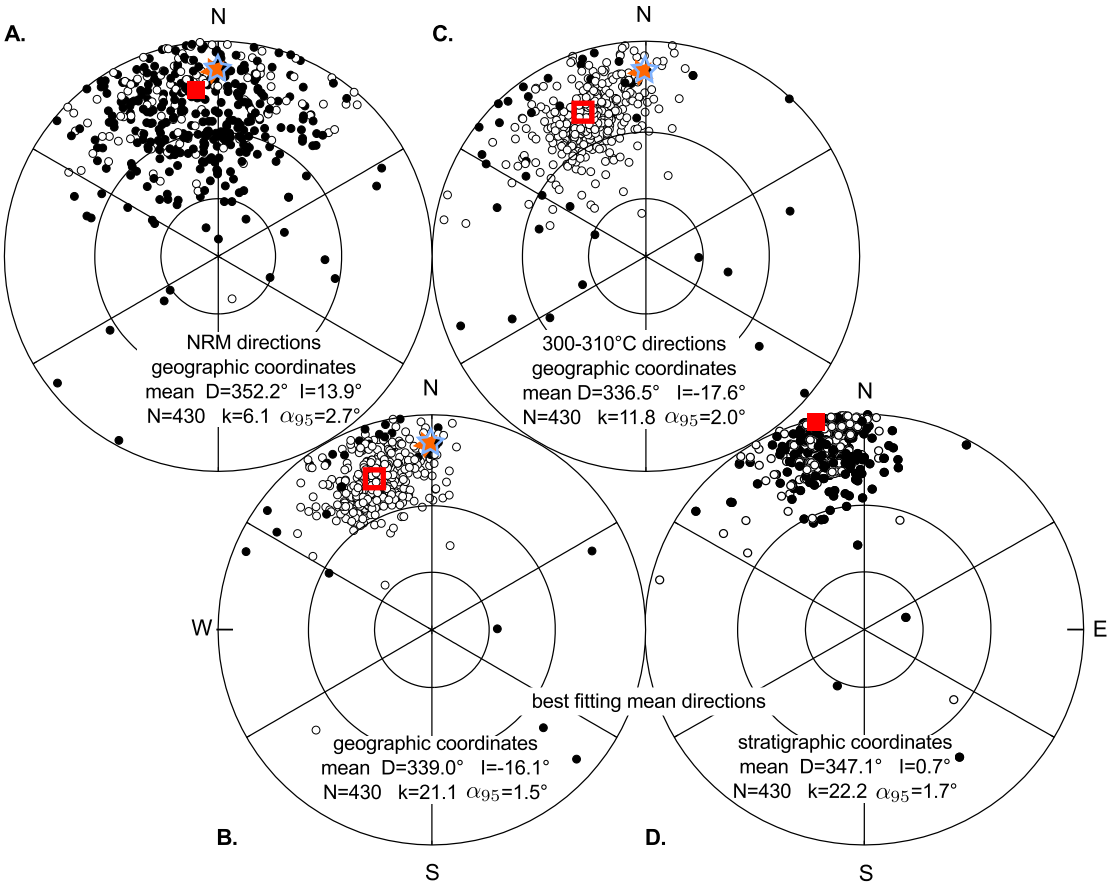

Figure 2.6: Stereonet projections in geographic coordinates of individual sample directions from (A) the natural remanent magnetization (20°C), (B) the high temperature magnetization component in geographic coordinates and (C) from a single (300° or 310°C) temperature step, (D) same population as in (B) but in stratigraphic coordinates. Transformation from geographic to stratigraphic coordinates uses the mean dip and dip direction shown in Figure 2.4. Solid symbols denote positive inclinations, unfilled symbols negative inclinations. The mean directions are shown in red (α_{95} ellipses are too small to be seen); a orange star represents the international geomagnetic reference field direction at the sampling site (D= 359.2°, I= 12.9°), a light blue star indicates the geomagnetic axial dipole direction (D= 0°, I= -10.9°).

den and Lowes, 1981) lends support that the high temperature component is not contaminated by recent overprinting. This emphasizes the good linear demagnetization trajectories of the high temperature component and that the line fitting procedure is independent of operator bias.

The mean tilt corrected direction for the high temperature magnetization component lies at D= 347.1° and I= 0.7° (N= 430, α_{95}= 1.7°) (Figure 2.6d). Except for six samples that come from a 3 m thick horizon, the high temperature magnetization component directions are solely of normal polarity. The propensity of normal directions is consistent with acquisition of magnetic remanence during the Cretaceous normal superchron, compatible with the age of the sediments. On the other hand, paleomagnetism of Cretaceous sedimentary and volcanic rocks in the Cajamarca region, 120 km to the south of Pongo de Rentema, pass the fold test and yield overall study mean directions in tilt corrected coordinates with declinations ranging from 325° to 346° and inclinations from -15° to -26° (Mitouard *et al.*, 1990, 1992), within the range of the mean in-situ direction from Pongo de Rentema (D= 336.5°, I= -17.6°, α_{95}= 2.0°). The average tilt corrected direction of seven sites of Neogene sediments from Cajamarca (D= 335.4°, I= -13.1°, α_{95}= 5.1°; Rousse et al., 2003) likewise yield a similar direction as the tilt-corrected Cretaceous direction.

If the high temperature component at Pongo de Rentema is not a primary Cretaceous remanence, then the entire section must have been overprinted during a normal polarity chron. The age of folding is clearly post-Paleocene as Paleocene sediments at Pongo de Rentema conformably overlie the Cretaceous rocks and are folded together with the Cretaceous rocks. One folding event in the Cajamarca area was constrained between 44 and 39 Ma because folded rocks below an observed angular unconformity yielded K-Ar dates from sanidine as young as 44.2 Ma while those above gave 39 Ma (Ar/Ar on sanidine) to 35.4 Ma (K-Ar on plagioclase) dates (Noble *et al.*, 1990). Other deformation events in the region have been recognized during the Oligo-Miocene and thereafter, but their relative importance on the development of the Andes is unclear (Sébrier *et al.*, 1988). Rousse *et al.* (2003) argued that the age of deformation and paleomagnetic rotations in northern and central Peru likely occurred in a brief time window between 8 and 4 Ma. Just east of Pongo de Rentema is a tectonic province called the Subandean zone, which represents a thin-skinned fold and thrust belt that initiated during the upper Miocene (circa 11 Ma) (Audebaud *et al.*, 1973; Noble and McKee, 1977) and is active today as evidenced by high levels of crustal seismicity (Jordan *et al.*, 1983; Dorbath, 1996). Thus, if the Pongo de Rentema section was remagnetized, the event must have occurred well after the Cretaceous and before the Bruhnes,

thus likely in a time span within 0.2 Myr, which is the average chron duration, or perhaps as long as ca. 1 Myr, which is the longest normal polarity chron since 40 Ma.

Rock magnetism

We characterized the magnetic mineralogy of the section on 22 samples (4%) using a Magnetic Measurements variable field translation balance, which measures hysteresis loops, back field magnetization and the temperature dependence of the in-field magnetic moment on 6 mm diameter cylindrical samples (about 300 mg of material). Hysteresis loops are noisy, being dominated by a paramagnetic component that made it impossible to resolve hysteresis parameters with any certainty. Magnetization intensity measured in a 30mT field decreases from room temperature to ∼450°C whereafter it markedly increases, peaks at 520°C, and then completely decays by 580°C (Figure 2.7a). The increase in magnetization signals the creation of a magnetic phase, which is likely magnetite given the Curie point of 580°C. The creation of a new magnetic phase at ∼450°C is compatible with a marked increase in magnetic susceptibility above 430°C as noted in the stepwise demagnetization experiments.

Because the variable field translation balance data were inconclusive, we carried out low temperature magnetization measurements on eight samples using a Quantum Design magnetic property measurement system (University of Bremen). The sample was cooled from room temperature to 10 K either in a zero field (ZFC) or in a 5 T applied field (FC). At 10 K, a 5 T field was applied, turned off, and then the magnetization of the sample was measured while heating to room temperature (Figure 2.7b). For all samples, both ZFC and FC experiments reveal a steep initial decrease in magnetization from 10 to 300 K and then a more gradual decrease; no prominent transitions are prevalent characteristic of magnetite (∼120 K), hematite (∼255 K) or pyrrhotite (∼34 K). Interpretation of the low temperature curves is ambiguous, yet reminiscent of oxidized, single domain magnetite (see Figure 3.6 in Dunlop and Ozdemir, 1997).

Scanning electron microprobe element mapping reveals the presence of iron and sulphur in the same minerals. Along with pyrrhotite, greigite (Fe_3S_4), the thiospinel counterpart of magnetite, is the only iron sulphide which can carry a remanence. Marcasite, a polymorph of pyrite, was unequivocally identified based on its star-like shape. It especially occurs in the more sandy horizons of the Romiron Formation. We also observed framboidal iron sulphides, which are likely pyrite and/or greigite (Suk *et al.*, 1990; Tudryn and Tucholka, 2004; Roberts,

2005; Wignall *et al.*, 2005). Pyrite and/or marcasite can account for the prominent paramagnetic component seen in the hysteresis loops. Moreover, pyrite and greigite can transform into magnetite upon heating (Tudryn and Tucholka, 2004), as we observed. A diagnostic property of greigite is its propensity for gyromagnetic remanence during alternating field demagnetization (Fu *et al.*, 2008). To test this, 12 samples were stepwise demagnetized up to a peak alternating field of 150 mT. The prevalence of a gyroremanent magnetization is readily observed by the systematic increase in magnetic moment above 40 to 60 mT (Figure 2.7c). Thus, the carrier of magnetic remanence is likely greigite and is likely not detrital in origin. The question then becomes, when did the greigite form?

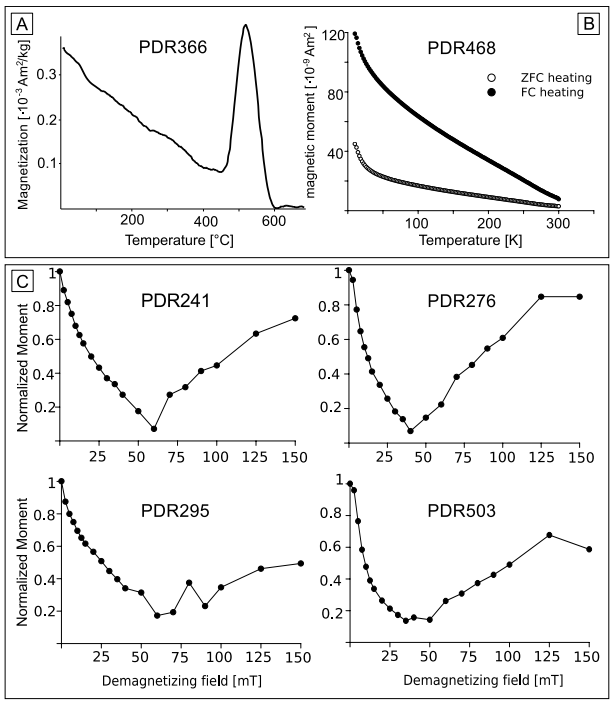

Figure 2.7: (A) Magnetic remanence in a 30 mT direct current field measured on heating from room temperature to 700°C. (B) Magnetic moment measured in a null field upon warming from 10 to 300 K. Samples were cooled from room temperature to 10 K either in a zero field (zero cooling, or ZFC) or in a 5 T field (field cooling, FC). (C) Stepwise alternating field demagnetization of the natural remanent magnetization for four samples. A continuous increase in magnetization above 40 to 60 mT likely signals the existence of a gyroremanent magnetization, characteristic of greigite.

The details of greigite formation are controversial. Besides the formation of greigite by anaerobic oxidation of methane (Fu *et al.*, 2008) or its neoformation from pyrite (Jiang *et al.*, 2001), greigite (Fe/S=0.75) is also thought to form authigenically as a intermediate step of the sulphidization of mackinawite ($FeS_{0.9}$ Fe/S=1.1) and/or pyrrhotite ($FeS_{1.1}$ Fe/S=0.9) (Heunemann, 1998; Roberts and Weaver, 2005) to pyrite (FeS_2 Fe/S=0.5) (Roberts, 1995). This conversion occurs

in anoxic sedimentary environments with the help of sulphate-reducing bacteria and usually happens during deposition (Roberts *et al.*, 1996; Roberts, 2005; Frank *et al.*, 2007) with a minimal delay between deposition and remancence acquisition as short as 100 yr (Tric *et al.*, 1991). On the other hand, late diagenentic greigite growth can happen as long as sulphide-rich porewater is available (Roberts and Weaver, 2005). Additionally complicating is the metastability of greigite, which decomposes within decades or less to pyrite in marine waters with restricted circulation and/or anaerobic conditions (Roberts and Weaver, 2005). However, under certain conditions greigite can be preserved. A lower content of dissolved sulphur due to restricted circulation or finer-grained sediments with lower permeability may inhibit the pyritization of greigite (Heunemann, 1998). Greigite has been found as the dominant remanence carrier at several places on the globe (Roberts *et al.*, 2011). The oldest preserved greigite reported is Cretaceous (Reynolds *et al.*, 1994), which was later confirmed to be of diagenetic orgin (Reynolds *et al.*, 1999).

Magnetostratigraphy

Figure 2.8 plots the bedding corrected directions versus stratigraphic height. One site clearly protrudes from this record with much wider directional swings compared to the rest of the section. This 3 m-thick unit represents a time span of about 13 kyr at 94.4 Ma, which is far too young to coincide with the ISEA reversed horizon (Vandenberg *et al.*, 1978; Tarduno, 1990; Gilder *et al.*, 2003; Zhu *et al.*, 2004) or other potential reversed horizons in the Cretaceous normal superchron (e.g., Tarduno *et al.*, 1992; Gradstein *et al.*, 2004). Besides this horizon, individual sample directions cluster fairly coherently with slightly more variability in the upper part of the section.

We subdivided the section into five groups (A to E) based on the breaks in the record (Figure 2.8). Paleomagnetic directions from the lower two groups (A and B) are distinct from groups C and D, which are in turn distinct from the upper part (E). Although the upper part has more directional variability, its maximum angular deviation (MAD) values are no different than the others (Figure 2.8), suggesting that there is no systematic difference in demagnetization behavior. However, Figure 2.8 reveals a systematic trend from high to low values of magnetic moment/magnetic susceptibility from bottom to top. This arises both from a decrease in moment and increase in susceptibility, which likely signals a progressive change in relative grain size, with the top of the section being dominated by more multi-domain greigite. The gradual yet systematic change in these parameters argues for a progressive development of the greigite and against a punctual

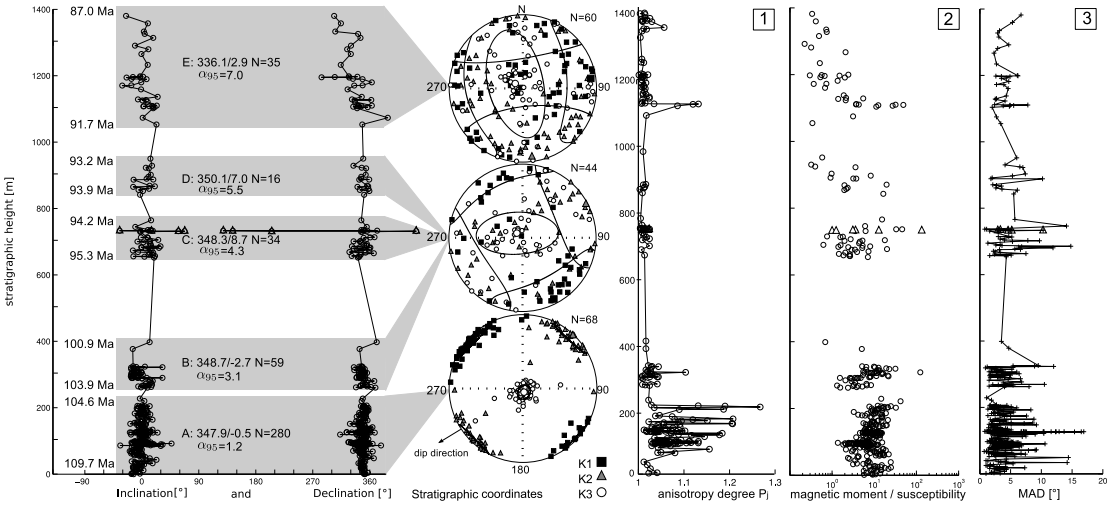

Figure 2.8: Declination and inclination versus stratigraphic height – triangles denote data from the 3 m thick horizon that shows wide swings in magnetization direction compared to the rest of the section. Gray shading indicates groups A to E shown together with their mean directions (samples from 3 m-thick horizon omitted from calculation for Group C). Stereonets to the right of the magnetostratigraphic profile plot the principle axes of the anisotropy of magnetic susceptibility ellipsoid in stratigraphic coordinates together with the mean directions and confidence ellipses (Hext, 1963). The dip direction is indicated with an arrow on the group A stereonet. Plots to the right show (1) anisotropy degree (P_j), (2) magnetization at 20°C divided by susceptibility, and (3) the maximum angular deviation (MAD) derived from the best fit line segments that define the high temperature component as a function of stratigraphic height.

remagnetization. Moreover, one observes no striking difference in magnetic moment or magnetic susceptibility in the samples from the 3 m-thick horizon, so magnetomineralogic differences do not appear to explain the origin of the highly variable directions.

We measured the anisotropy of magnetic susceptibility (AMS) on 172 sister samples using either an AGICO KLY2 Kappabridge at the Munich laboratory or with an AGICO MFK1-FA at the University of Tübingen. No intra-laboratory instrument bias was observed. In stratigraphic coordinates, minimum principal axes lie orthogonal to the bedding plane while maximum and intermediate axes lie in the bedding plane (Figure 2.8), typical of sedimentary fabrics. Especially toward the lower part of the section, maximum and intermediate axes are segregated, with maximum axes lying parallel to the strike direction, typical of a weak tec-

tonic fabric (Parés *et al.*, 1999). Definition of the tectonic fabric roughly correlates with anisotropy degree, which is $1.07 \pm 0.04\%$ for Group A and $1.03 \pm 0.04\%$ for the other four groups. No link exists between remanence and anisotropy parameters – including for the 3 m-thick unit with dispersed directions. Differences in magnetic anisotropy along the stratigraphic profile argue against a section-wide pulse of remagnetization. Moreover, the carriers of the anisotropy signal must have existed in the rock prior to folding otherwise no sedimentary fabric would be prevalent, nor would those contributors be slightly reoriented to yield a tectonic fabric with maximum principal axes parallel to bedding strike. Since greigite is intimately associated with the assemblage of grains contributing to magnetic susceptibility, then the likelihood that it formed prior to folding must be considered as a possibility.

Tilt corrected directions from Pongo de Rentema transferred to virtual paleomagnetic poles yield a mean pole at a latitude of 76.1° and longitude of 216.6° (A_{95}=1.2°, N=430) (Figure 2.9). This mean pole lies an angular distance 9 to 12° away from the 90 to 110 Ma part of the synthetic apparent polar wander path for South America (Besse, 2002). The 90 to 110 Ma part of the synthetic apparent polar wander path predicts the most equatorial paleolatitudes for Pongo de Rentema (-6 to -12°) than any time after 90 Ma (-9.8 to -22.1°). This ca. 8° discrepancy in paleolatitude between the mean tilt corrected paleolatitude of Pongo de Rentema and the synthetic path is likely not resolved by inclination shallowing. In the vicinity of the equator, inclination shallowing is negligible: even a flattening factor of 0.7 on expected inclinations of 5° or 15° yields measured inclinations of 3.5° and 10.6°, respectively. These are in most cases within the α_{95} confidence bounds, as it is in our case for I= 0.7° (α_{95} = 1.7).

At this point we are confronted with a dilemma. If the high temperature magnetization component is a primary remanence, then why is the mean inclination ∼10° shallower than both the expected and nearby (120 km) site mean inclinations? And why is the in situ direction so similar to other study mean directions in the vicinity? Conversely, if the high temperature magnetization component is a secondary, post-40 Ma yet pre-0.8 Ma remanence, then why is the vast majority (98.6%) of all directions solely of normal polarity, why do magnetic parameters vary fairly systematically with stratigraphic height, and why is the magnetic fabric characteristic of sedimentary deposits? If greigite formation occurred after the Cretaceous normal superchron, then we would expect more complex demagnetization trajectories, sometimes with superimposed normal and reversed components. As this point we do not favor either scenario. Instead, we explore the ramifications of paleosecular variation scatter curves derived from sediments and juxtapose

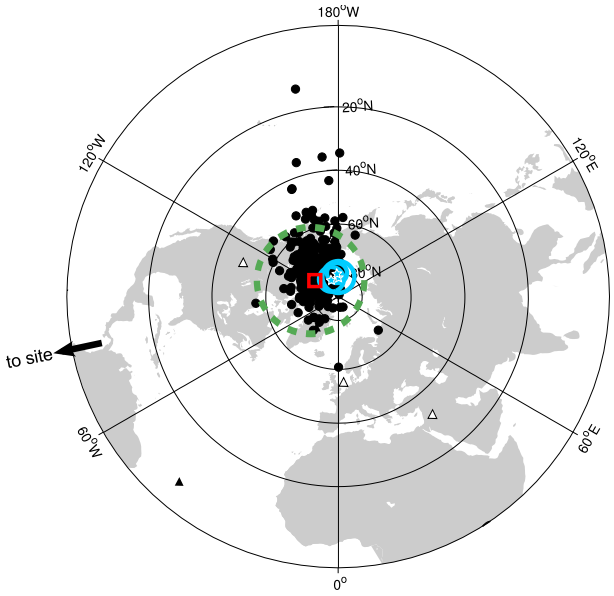

Figure 2.9: Virtual geomagnetic poles from Pongo de Rentema (black dots), the mean is shown as a red square. The A_{95}-cone is smaller than the symbol. Also shown are the synthetic paleomagnetic poles for South America (white stars) for 90, 100 and 110 Ma (Besse, 2002) with their A_{95}-cones in blue. The green dashed line denotes the Vandamme cut-off colatitude. Triangles denote samples from the 3 m thick horizon.

them with paleosecular variation scatter curves derived from volcanic rocks. We then compare the scatter values against other studies from the Cretaceous Normal Superchron and with the 0-5 Ma time period.

2.1.4 Discussion

Calculation of S values and extraneous (non-geomagnetic) influences on Δ

The S-value for the Pongo de Rentema section based on the entire record of 430 samples is $16.8^{17.6}_{16.0}$ (95% confidence limits after Cox, 1969) (Figure 2.11). If one rejects the six samples from the 3 m-thick unit that has the highly divergent directions, then S reduces to $11.2^{11.8}_{10.7}$ (N= 424). Such a large difference between the two highlights the sensitivity of the S value to a few outlying points due to

the square of the angular distances used in the calculation. Six of 430 samples, or 1.4% of the total, changes S by 33%.

Several factors must be considered before drawing conclusions from the average S value of the entire section. We first investigated the affect that Sun compass corrections and bedding attitudes have on the S value. Of the samples possessing a high temperature component, 62 had Sun compass measurements. Applying either individual Sun compass corrections for the local declination anomaly or correcting each sample for the average local declination anomaly had essentially no influence on S: 8.24 versus 8.26, respectively. However, assigning individual or bulk bedding corrections has a greater influence on S. For N= 424, S is $11.2^{11.8}_{10.7}$ as above for the bulk bedding correction. To apply individual corrections we recall that 82 bedding attitudes were measured throughout the section. We linearly interpolated the bedding attitudes to assign each sample a discrete dip and dip direction. This resulted in an S value of $14.2^{14.9}_{13.5}$, amounting to a 20% difference. Such a difference often constitutes a significant part of the discrepancies in field models that account for the latitudinal dependence on S as will be discussed below. Moreover, bedding corrections are sometimes neglected when calculating S from volcanic rocks, where paleohorizontal is often ambiguous; the gradual steeping of flank slope might also change bedding conditions from flow to flow (Watkins and Walker, 1977).

Uncertainty limits on the S value (Cox, 1969), which are solely dependent on N, can give a misleading view about the distribution of the data about the mean. For N= 424, the bootstraped 95%-confidence limits on a S of $11.2^{12.6}_{10.0}$ are wider, but data-specific. Uncertainty limits about S could increase from poorly defined data (coarse demagnetization steps, high uncertainties on best-fit line segments, etc.). For volcanic rocks, intra-site corrections help compensate for this (Lee, 1983). However, sedimentary datasets often have only one sample per horizon, so calculating the within-site scatter is impossible and another method must be sought to estimate data quality.

Scatter due to orientation error was assessed via the Sun compass corrections to have no affect. We then assessed scatter due to data quality by weighting each sample by its maximum angular deviation (MAD) obtained from principal component analysis (Kirschvink, 1980). Applying a quality factor of $q = 1/MAD$ to the N= 424 data using $S_{MAD} = \sqrt{\sum (q_i * \Delta_i^2)/\sum q_i}$ results in a S_{MAD} of 10.6 as opposed to 11.2. Considering the uncertainties, this 5% difference seems fairly inconsequential, as there is no correlation between MAD and Δ (Figure 2.10a). Excluding data points with MAD $> 10^\circ$ (N=22) yields an S_{MAD} of 11.3, which is essentially the same as when applying no correction. One can use a more

sophisticated weighting factor $q = \frac{r*n}{MAD}$, where (r) is the temperature range used for the best-fit procedure times the number of steps (n) divided by MAD. Inserting into the weighing equation results in a S_q of 10.2, making a difference of 9% with respect to the non-corrected value.

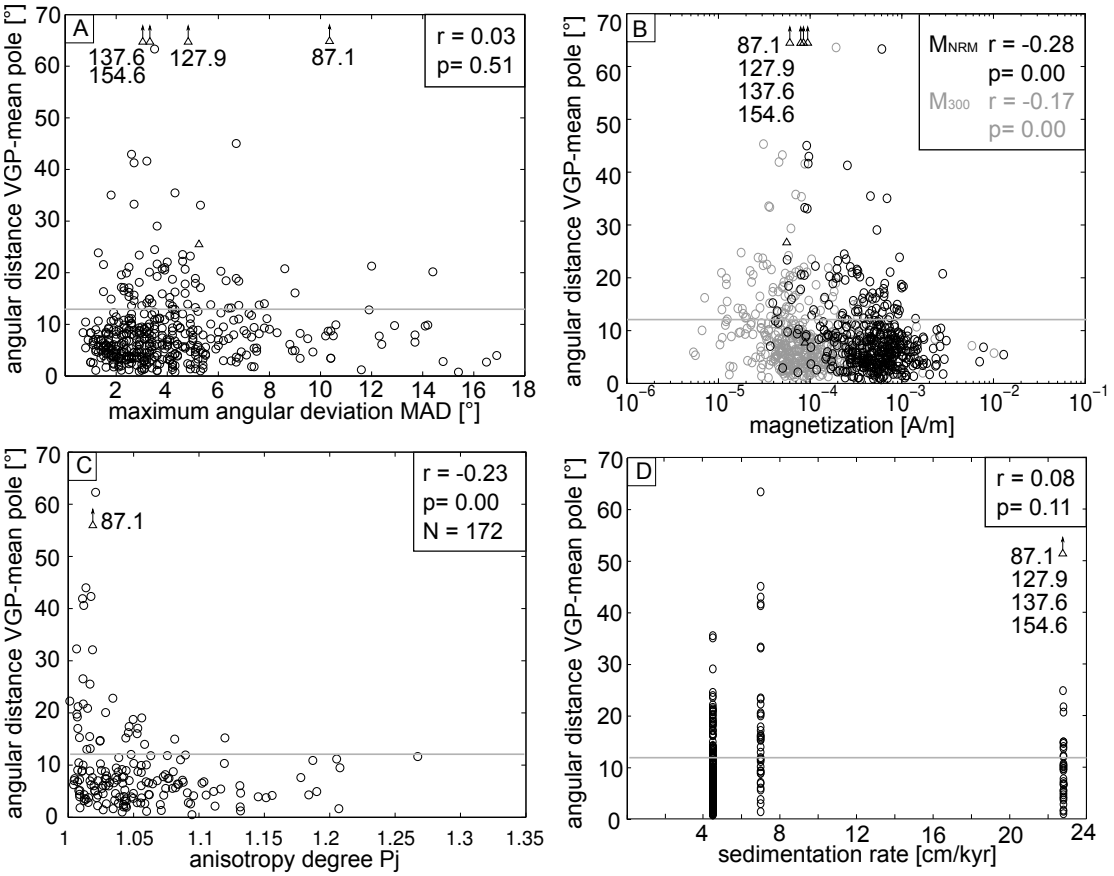

Figure 2.10: Angular distance of the virtual geomagnetic pole (VGP) of each sample with respect to the mean pole (Δ) versus (A) the maximum angular deviation (MAD) determined from best-fit line segments, (B) the magnetic moment of the NRM M_{NRM} and at the 300°C or 310°C demagnetization step M_{300}, (C) the anisotropy degree, and (D) sedimentation rate. The grey line indicates an S value of 11.2 (N=424). Each diagram lists the correlation coefficient (r) and the probability of getting a correlation by random chance (p).

One can also question whether correlations exist between rock magnetic properties and Δ. For example, weaker magnetizations could indicate more intra-

sample field variation or poorer aligning efficiency of the remanence carrying grains. This is dispelled as both the magnetic moment of the 20°C step and the 300-310°C demagnetization steps have only small correlation (correlation coefficient < 0.3) with angular distances (Figure 2.10b). Similarly, only a slight influence (correlation coefficient < 0.3) from the magnetic fabric can be identified, such as between the degree of anisotropy of magnetic susceptibility (P_j) and Δ (Figure 2.10c). It is noteworthy that all samples with Δ greater than 25 have relatively low ($< 3\%$) anisotropy degrees.

Data selection criteria also play a significant role on the S value. For example, McFadden *et al.* (1991) arbitrarily rejected all poles whose colatitudes were greater than 40° away from the mean. Applying this rule reduces our data set from N= 430 to N= 421 and yields an S value of $10.0^{10.6}_{9.6}$. A method using a dataset-specific cut-off colatitude was proposed by Vandamme (1994). Employing this method to Pongo de Rentema imposes a cut-off colatitude of 19.8° (N=399), which reduces S to $8.4^{8.9}_{8.0}$ (Figure 2.9). Because transitional field directions are less likely to be found than stable polarity directions, Biggin *et al.* (2008b) argued in favor of outlier cut-offs. On the other hand, unless the outlying directions are proven not to be of geomagnetic origin (such as due to lightning, etc.), there is no reason to omit them as they reflect the behavior of the magnetic field itself. If the excursions and/or short-lived reversals are kind of an exaggerated paleosecular variation and driven by the same mechanism, they should naturally contribute to the S value that quantifies paleosecular variation (Gubbins, 1999; Wicht, 2005).

The calculation of a standard deviation is underlain by the assumption of a Gaussian distributed population, so certain datasets, especially those based on small numbers, might not fulfill this condition. Such distributions can also be described by quantiles. For a Gaussian distribution, 68.2% of the population lie within one standard deviation (1 σ) from the mean. The calculation of a 68.2-quantile ($q_{68.2}$) is the same as finding the value that separates the lower 68.2% of the angular distances from the upper 31.8%. Using quantiles on the Pongo de Rentema data results in $q_{68.2} = 9.09$ for N= 430 and $q_{68.2} = 9.14$ for N= 424. Thus, employing the 1-σ quantile seems to be a more meaningful method to quantify the standard deviation of the angular distances. $q_{68.2}$ values resemble S values derived using cut-off co-latitudes, except the former has a statistical meaning whereas the latter is arbitrarily assigned.

Time Averaging I

Pongo de Rentema constitutes one of the longest sections directly sampled for a paleosecular variation study. Seen over sufficiently long (>5 Myr) time scales, paleomagnetic directions and their corresponding poles may slowly evolve due to plate motion, true polar wander, etc. Because the Pongo de Rentema section is substantially longer than 5 Myr, such effects should be accounted for (Lee, 1983), especially since the paleomagnetic directions vary significantly from bottom to top of the section (Figure 2.8). Indeed, this observation could favor the high temperature component as a primary remanence, for if it was overprinted in less than 0.2 Myr, or even 1Myr, then we would expect paleomagnetic directions to be more uniform. In particular, latitudinal motion of South America of 5 cm/yr would only change inclination by <0.5°, yet the measured inclination varies by ca. 8°.

Different strategies can reduce the affect of apparent or true polar wander on S, such as applying a sliding window with window lengths shorter than 5 Myr (Figure 2.11). On the other hand, sampling density can differ widely among each time window, so one might apply a sliding window based on the number of observations. For Pongo de Rentema (N= 424), S varies depending on the window size, with S values ranging between 6.1 and 19.3 for a window 51 data points wide and between 8.9 and 12.0 when averaging over 301 samples. Observed in this way, window length impacts the calculated S value. A higher sampling density also bears on the probability to observe short-lived, high amplitude swings. We investigated the influence of sampling frequency in several different ways, but we concluded that this effect is essentially impossible to quantify, as the true S is unknown at any given time. Defining population subsets from the most densely sampled horizon (N= 37), where S should be fairly constant, yields no striking correlation.

S varies significantly within the 1400 m (Figure 2.11). Based on N= 424, S remains fairly constant at ca. 9 in the lower three-quarters of the section, and then increases markedly to ca. 21 in the upper fourth. A critical issue is whether the directional variability in the 3 m-thick horizon in Group C owes its origin to the geomagnetic field or not. Rock magnetic analyses failed to distinguish this population from the rest, but we still remain suspicious. On the other hand, if the remanence is primary, the 3 m thick horizon was sampled during the time when sedimentation rate was the highest, and thus the chance of observing quickly varying field directions is greater. The rise in paleosecular variation toward the end of the superchron could make sense as some dynamo models suggest higher paleosec-

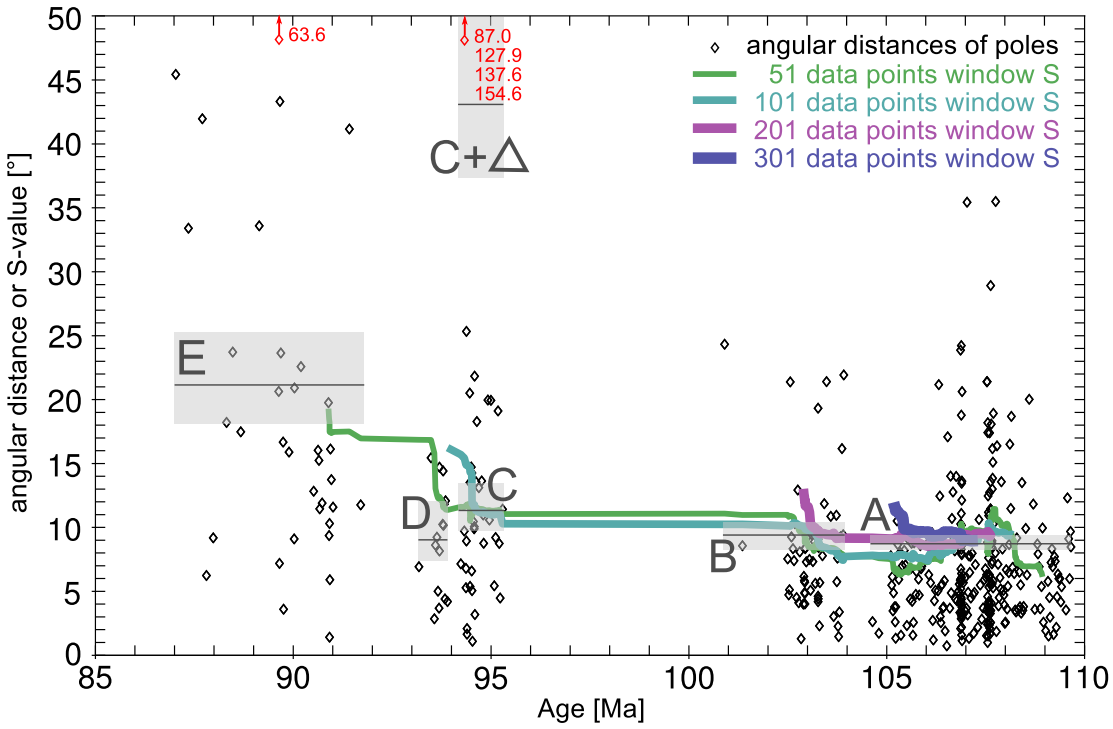

Figure 2.11: Angular distances to mean pole (diamonds) and S values as a function of time. S values calculated with a sliding window, with window lengths of 51, 101, 201 and 301 data points, are plotted against age of the window mid point. Grey boxes refer to the 95% uncertainty limits on S values (black line) calculated from the five groups (A to E) in Figure 2.8. Box C is shown twice, one that includes the highly diverging directions (shown as triangles in Figure 2.8) and one without.

ular variation preceding reversals (Pétrélis *et al.*, 2009), although 8 Myr before the end of the superchron seems fairly remote from the end of the superchron.

Time Averaging II

Sedimentary and volcanic rocks record the paleo-field over different time scales. Depending on their thickness, volcanic flows tend to take a brief snapshot of the Earth's magnetic field. Moreover, limits in absolute dating methods make it difficult to know the eruption frequency of multiple flows, leading to the potential overrepresentation of specific times within a paleosecular variation cycle, as volcanic eruptions tend to occur in short pulses. On the other hand, sediments

smooth the paleosecular variation record like a sliding window. Neglecting post-depositional effects, inch cores, which represent much larger time averages (500 years for a sedimentation rate of 5 cm/kyr), should "despike" the magnetic record. Thus for sediments, S should be sensitive to the sedimentation rate, but the correlation between Δ and sedimentation rate is unclear (Figure 2.10d). A general positive trend exists if one considers the outliers; if not, then no correlation is discernable. From 14 lake records, Kruiver *et al.* (2002) found an insignificant correlation between S and sedimentation rates greater than 10 cm/kyr; yet they discerned a possible positive relationship between S and sedimentation rates less than 10 cm/kyr.

We modeled the influence of the sedimentation rate on S by creating an artificial Gaussian-distributed population (N= 10000) of angular distances with a mean S of 10. These 10000 data points are considered to represent a complete record of the magnetic field. In reality, not all horizons in a section are sampled. To simulate sedimentary recording, subsets of 500 windows (5%) of 5 samples were randomly drawn from these 10000 and averaged. 500 was chosen to resemble the data volume of our study. We compared these with a simulated volcanic "snap-shot" recorder by calculating paleosecular variation from the 500 randomly drawn samples directly, without averaging over multiple horizons. The drawing of 500 samples was repeated 1000 times and the expected S of 10 was subtracted from the calculated S values.

Figure 2.12a shows that the dispersion of S calculated from volcanic rocks is larger than that from sedimentary rocks, whereas sediments clearly underestimate S and have less dispersion. We quantified the extent that sediments can underestimate S by varying the width of the averaging window (Figure 2.12b), where larger windows mimic lower sedimentation rates. This relationship becomes invariant with respect to window width, consistent with Kruiver *et al.* (2002). We repeated this calculation with 100, 200 and 1000 sub-samples out of the original 10000. Above a window half width of 10, the amount of underestimation becomes constant regardless of the number of samples. Below 10 window half widths, the more the samples, the less the underestimate.

To complete the exercise, we varied the expected S value of the artificial dataset in steps from 1 to 25 (Figure 2.12c) using window half-widths up to 50. Interestingly, a typical marine sediment consistently underestimates the "true" S-value by 20% (Figure 2.12d). Thus, S values derived from sediments can be corrected for the true value by multiplying the measured S value by 1.2. At Pongo de Rentema, the number of possible time horizons clearly exceeds 10000, but as the maximum underestimate is independent of the ratio of the drawn subset size to total num-

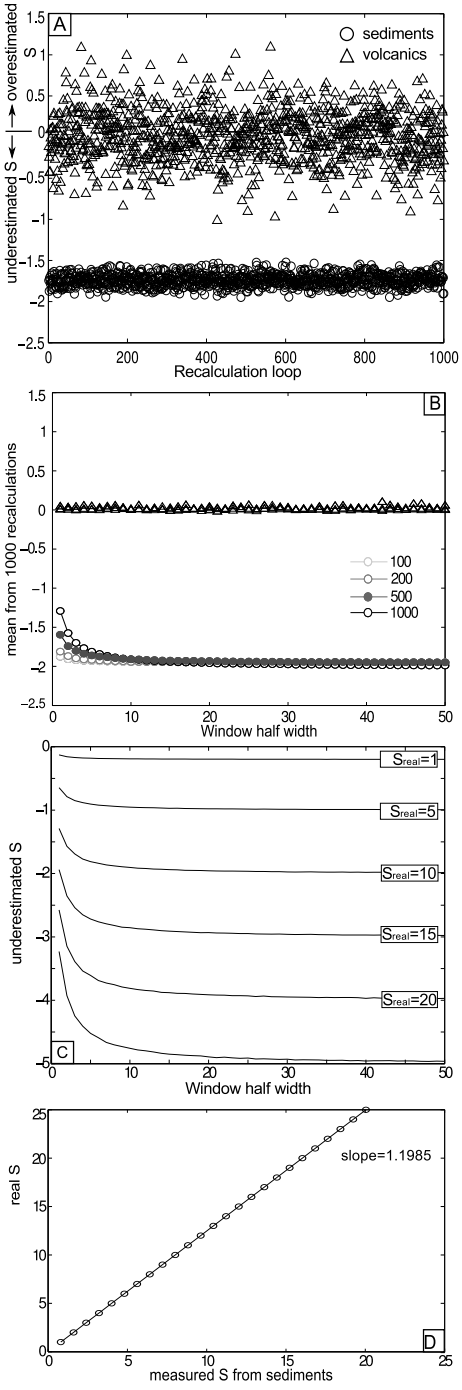

Figure 2.12: (A) From an artificial Gaussian distributed set of angular distances (N= 10000), subsets of 500 samples were drawn 1000 times. S was calculated to mimic volcanic (triangles, no sliding window applied) and sedimentary (circles, window half-width of 2 or total of 5 samples in the window) recorders. The plot shows the difference of the observed S with respect to the expected S. (B) Dependency of the window length, which mimics sedimentation rate, on the observed S value. Above 10 window half-widths, the amount that S is underestimated becomes invariant with respect to number of samples included in the window (curves for drawn subsets of 100, 200, 500 and 1000 samples shown). Triangles represent volcanic recorders fit with a sliding window. (C) The amount that S is underestimated versus window half-width (S= 1, 5, 10, 15, 20 and 25). (D) The difference between expected and observed S assuming the hypothetical sediment averages at least 250 years of secular variation. Observed S values will systematically underestimate the "true" value by 20%.

ber of horizons, we can apply this simple model to our data. This results in an increase of S (N= 424) from 11.2 to maximum of 13.4 or S (N= 430) from 16.8 to a maximum of 20.2.

Pongo de Rentema compared to other S values in time and space

Most studies on paleosecular variation during the Cretaceous normal superchron come from volcanic records (see Biggin *et al.*, 2008b, for a comprehensive compilation) (Figure 2.13). Only one study during this time period was carried out on sediments by Cronin *et al.* (2001), who collected 923 samples of carbonates within ∼32 m. The 32 m is thought to represent 4.5 Myr of time, for a sedimentation rate of 0.7 cm/kyr – about an order of magnitude less than Pongo de Rentema. If the high temperature magnetization component from Pongo de Rentema represents a primary remanence, then we can compare the S values of the five groups from Figure 2.8 with the other studies. Although we condone its use, a Vandamme cut-off was applied for comparison to remain consistent with previous work (Figure 2.13b). Observed solely in the time domain, there appears to be significant variation in S during the Cretaceous normal superchron; however, no latitudinal dependency on S is taken into account in Figure 2.13b. Considering only Pongo de Rentema, and if those data indeed reflect primary remanences, then we find significant variability of paleosecular variation during the Cretaceous normal superchron ranging from 8.8 to 21.1. Biggin *et al.* (2008b) derived a mean S of $9.9^{11.3}_{7.8}$ for the entire Cretaceous normal superchron based on a compilation of sites (N= 445) from volcanic rocks. A Vandamme cut-off S value of $8.4^{8.9}_{8.0}$ for the whole Pongo de Rentema section is quite compatible with this, when accounting for a 20% increase, raises the S-value to $10.1^{10.6}_{9.6}$.

S is plotted as a function of latitude in Figure 2.13c for the individual studies from the Cretaceous normal superchron together with compilations for time periods from 0 to 5 Ma and from 80 to 110 Ma (Lee, 1983; McFadden *et al.*, 1991; Johnson *et al.*, 2008; Biggin *et al.*, 2008b). No S values were available for the 80-110 Ma interval for latitudes <10°, so McFadden *et al.* (1991) linearly extrapolated the data from the 10-35° latitude band (S of $8.7^{11.3}_{7.0}$) to the equator to predict an equatorial S of $6.8^{9.4}_{2.3}$. Pongo de Rentema group E overlaps in time with the Italian carbonates (Cronin *et al.*, 2001) yet has a higher S value (Figure 2.13b). Taking latitude dependency of the S value into account, one would expect the opposite – a lower S value at the equator. The difference could be due to the extreme difference in sampling density and/or sedimentation rate, or to a longitudinal asymmetry of paleosecular variation (Wicht, 2005), which is not canceled

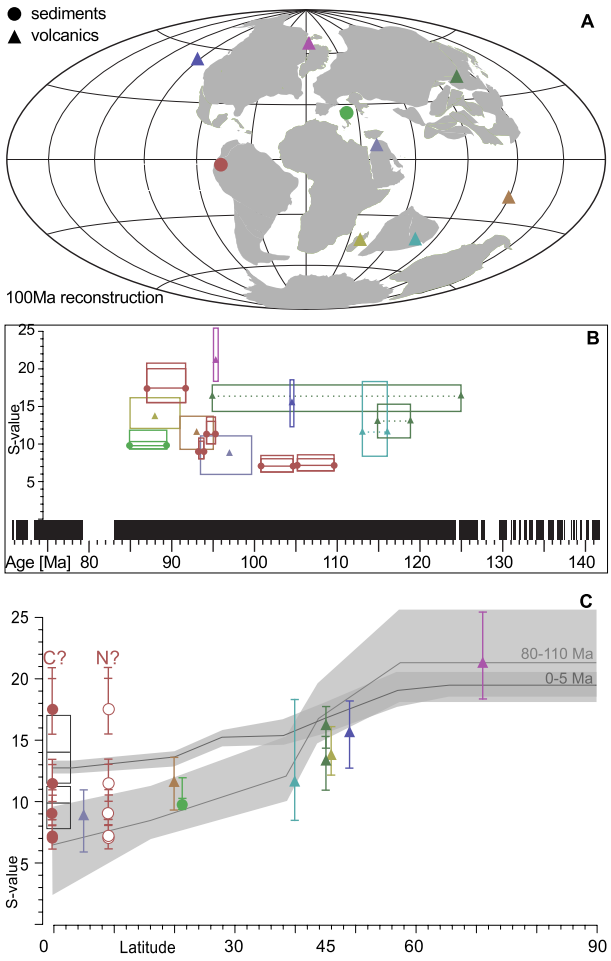

Figure 2.13: (A) Sites from paleosecular variation studies placed onto a paleogeographic reconstruction at 100 Ma. Triangles (volcanics from Biggin et al, 2008) and dots (sediments from Cronin at al, 2001 and this study) are color-coded to link with subplots B and C. (B) S value as a function of absolute time with 95% confidence limits. Dashed time lines for studies on volcanic rocks represent uncertainty on age determinations. For sediments, the length of the solid line shows the age range of the sampled section; the height of the corresponding box denotes the 95% uncertainty limits. The additional line on top represents the maximum recorder corrected value. (C) S value as a function of latitude of individual studies from the Cretaceous normal superchron (colors and symbols are same as above plots). Red circles represent the average S values of the five groups from Pongo de Rentema; solid circles represent the case of a primary (Cretaceous C?) remanence and open circles for the case of a secondary (Neogene N?) remanence. The dark and light gray curves show the variation in S (with 95% confidence limits) for 0 to 5 Ma and 80 to 110 Ma, respectively (from McFadden *et al.*, 1991). Dark lines with surrounding boxes are equatorial S-values from Biggin *et al.* (2008b) for the Cretaceous normal superchron and Johnson *et al.* (2008) for the last 5 Myr with their 95% confidence limits.

out in individual studies as it would be when summing over latitude bands (Lee, 1983).

On the other hand, the bulk S value from Pongo de Rentema resembles the near-equatorial S values for the last 5 Myr (Figure 2.13c) – $12.8^{13.2}_{12.6}$ (N= 2382 sites in McFadden *et al.*, 1991) and $14.0^{17.0}_{11.6}$ (N= 46 studies in Johnson *et al.*, 2008). Indeed, almost all S values from the Cretaceous normal superchron, especially those from latitudes higher than 30°, are virtually indistinguishable from those during 0 to 5 Ma. As more data become available, this distinction becomes increasingly blurred. Moreover, the S value of sediments ($12.5^{13.6}_{11.3}$) deposited near the equator during the Permian-Carboniferous Reversed Superchron also resembles the equatorial S value for 0 to 5 Ma (Haldan *et al.*, 2007). Summing over all the potential uncertainties discussed above, we are extremely pessimistic that S values can ever be used to distinguish field models. With these uncertainties, we find that S varies in time such that testable hypotheses based on S are essentially irretrievable.

2.1.5 Conclusions

Our goal was to study the paleosecular variation of the geomagnetic field during an interval of Earth's history where the polarity remained remarkably stationary. Our first question was whether this period was statistically distinct or exists as an end-member of a Gaussian-distributed population. A log-normal plot of polarity lengths for the last 167 Ma led us to define a polarity superchron as a chron lying more than 4σ away from the mean polarity duration. If the Cretaceous normal superchron was clearly distinct from this distribution, it would underpin the idea of two distinct energy regimes of the geodynamo – one reversing regime and one stable superchron regime. These regimes should differ in the vigor of their core convection, paleomagnetically measurable via paleosecular variation.

We then studied the paleosecular variation of a 1400 m-thick section of marine carbonates in northern Peru. We chose this section specifically because it was paleontology well described, allowing us to correlate it both in relative and absolute time scales, and because the outcrop conditions allow for fairly continuous sampling. Moreover, paleogeographic reconstructions place this area near the geomagnetic equator. This has the distinct advantage to avoid inclination shallowing effects on the recorded directions. Moreover, S values determined at the geomagnetic equator represent the minimum, or baseline, scatter for any specific time. One can thus directly compare S derived from equatorial latitudes for all time periods without needing to know how S varies as a function of latitude.

Stepwise demagnetization isolated a well-defined magnetization component, likely carried by syn- or post-depositional greigite in 81% (430) of the samples. Polarities of 424 out of 430 samples are normal, with the other six samples coming from a 3 m-thick horizon. A regional fold test is negative. We could not conclude whether the magnetic remanence is primary, recorded during a 22.7 Myr span within the Cretaceous normal superchron, or secondary, recorded during a ca. 0.2 Myr period of normal polarity, likely in the last 11 Myr, but surely pre-Brunhes. Both possibilities were considered in the subsequent discussion.

Before comparing with other studies, we examined possible extraneous contributions to S and how S itself should be calculated. For example, whether instantaneous or averaged bedding corrections are applied modify S by 20% in this study. Weighting samples by their maximum angular deviation (MAD) values obtained in the line fitting procedure had no discernable effect on S. Neither an influence of sun compass corrections nor influences of sampling frequency on S could be detected. This latter result is likely due to the averaging effect of short wavelength field variations in marine sediments. Because S values are strongly biased by outliers, cut-off procedures have been advocated in several studies. But unless these outliers are proven not to be of geomagnetic origin, we argue that there is no reason to disregard them, even if the time represented by the outliers is much shorter than the total duration of the whole section. Quantiles are a statistically more rigorous way to treat outliers than simple cut-off colatitudes and should be used in the future to quantify paleosecular variation rather than the S value.

Modeling how sedimentary and volcanic rocks record the Earth's magnetic field revealed that S values from volcanic rocks are six times more dispersed than from sedimentary rocks, whereas sedimentary rocks will systematically underestimate S by up to 20% of the "true" value. Any paleosecular variation study using the S value as a comparative parameter should add 20% to sedimentary records when sedimentation rates are less than 10 cm/kyr.

If the magnetic remanence from Pongo de Rentema is primary, then S is quite variable during the Cretaceous normal superchron. S values are fairly constant at ca. 9 from 109.7 to 100 Ma and more variable, yet higher (ca. 21) from 96 to 87 Ma. An average S calculated by applying the Vandamme cut-off, shows no marked dissimilarly with predicted S values from the compilation of Biggin *et al.* (2008b), but slightly higher than that of McFadden *et al.* (1991) during the Cretaceous normal superchron. On the other hand, the average S value from Pongo de Rentema is indistinguishable from that expected for equatorial S values for the last 5 Ma (McFadden *et al.*, 1991; Johnson *et al.*, 2008), which is in

turn similar to an equatorial S value measured in sediments deposited during the Permian-Carboniferous Reversed Superchron (Haldan *et al.*, 2007). In conclusion, given the sum of all uncertainties contributing to an S value, we find it questionable whether S is a suitable parameter for characterizing paleosecular variation, and hence, unworthy to constrain geodynamo models. Otherwise, we find no statistical distinction between Cretaceous and recent fields.

Acknowledgements

We thank Javier Jacay and Jose Castillo Campos from the Universidad Nacional Mayor de San Marcos in Lima, Peru for their help in the field. The Institut pour la Recherche et la Développement in Lima, Peru and in Quito, Ecuador are thanked for the provision of a field vehicle and logistical support. Emmanuel Robert is thanked for significant aid in constraining the age profile of the section. Discussions with Ramon Egli and Rob Coe were highly valuable. We also thank Erwin Appel and Greig Paterson for helpful reviews and Yongxin Pan and Keke Zhang for editorial handling. Open access to the Kappa Bridge MFK1-FA was given by the Geophysik section of the University Tübingen. Thomas Friedrichs and Tilo von Dobeneck from the University Bremen greatly assisted with the MPMS and AGFM. Funding was provided by IDK 31 THESIS of the Elite Network of Bavaria (ENB) and grants from the Deutsche Forschungsgesellschaft (DFG-GI712/2-1 and DFG-GI712/2-2).

2.2 Addendum

The slope of the latitude dependency of the S value is traditionally attributed to varying contributions of multipolar components of the Earth's magnetic field (McFadden *et al.*, 1991). But how would specific multipolar contributions influence the shape of this S curve? Inspired by a work of Van der Voo and Torsvik (2001) Tarduno *et al.* (2002) presents a simple relationship between latitude and magnetic inclination based on varying axial octupolar fields. Here this equation is now extended to also contain the contributions of quadrupolar fields and used to model how the slope of the S value is sensitive to contributions of persistent multipole components of the Earth's magnetic fields.

The potential of the Earth's magnetic field is described by

$$\Psi(r,\theta,\phi) = \frac{R_\oplus}{\mu_0}\sum_{l=1}^{\infty}\sum_{m=1}^{\infty} P_l^m(\cos\theta)\left(\frac{R_\oplus}{r}\right)^{l+1}\left(g_l^m\cos m\phi + h_l^m \sin m\phi\right) \tag{2.2}$$

with the radius, latitude and longitude r, θ, ϕ, the Earth's radius $R_\oplus$, the magnetic vacuum permeability μ_0, polynomial P_l^m and Gauss-Schmidt coefficients g_l^m and h_l^m. For simplicity we only consider axial contributions ($m = 0$), which drops out of the non-axial term $h_l^m \sin m\phi$ and $\cos m\phi$ and reduces equation (2.2) to

$$\Psi(r,\theta,\phi) = \frac{R_\oplus}{\mu_0}\sum_{l=1}^{\infty} P_l^m(\cos\theta)\left(\frac{R_\oplus}{r}\right)^{l+1} g_l^m \tag{2.3}$$

Today's Earth's magnetic field is not purely dipolar but has multipolar contributions. For 1990 the International Georeference Field (IGRF) is modeled to contain about 10% axial quadrupolar and 5% octupolar contributions, higher multipoles can be neglected. Thus, also here only dipolar, quadrupolar and octupolar components ($l = \{1,2,3\}$) shall be considered. Together with the polynomials $P_1^0 = \cos\theta$, $P_2^0 = \frac{1}{4}(3\cos(2\theta)+1)$ and $P_3^0 = \frac{1}{8}(5\cos(3\theta)+3\cos\theta)$ the potential is

$$\begin{aligned}\Psi(r,\theta,\phi) = \frac{R_\oplus}{\mu_0} \quad [\quad & \cos\theta g_1^0\left(\frac{R_\oplus}{r}\right)^2 + \\ + \quad & \frac{1}{4}(3\cos(2\theta)+1) g_2^0\left(\frac{R_\oplus}{r}\right)^3 + \\ + \quad & \frac{1}{8}(5\cos(3\theta)+3\cos\theta) g_3^0\left(\frac{R_\oplus}{r}\right)^4]\end{aligned} \tag{2.4}$$

The tangent of the magnetic inclination is defined as

$$\tan I = \frac{Z}{H} = \frac{-B_r}{|B_\theta|} \tag{2.5}$$

The components of the magnetic field can be deduced from the magnetic potential with

$$B_r(r,\theta,\phi) = -\mu_0 \frac{\partial \Psi}{\partial r} \tag{2.6}$$

$$B_\theta(r,\theta,\phi) = -\mu_0 \frac{1}{r}\frac{\partial \Psi}{\partial r} \tag{2.7}$$

$$B_\phi(r,\theta,\phi) = 0 \tag{2.8}$$

B_ϕ is zero as axial quadrupoles and octupoles do not vary zonally. Deriving equation (2.4) gives

$$\begin{aligned} B_r = \frac{\partial \Psi}{\partial r} = \mu_0 \frac{R_\oplus}{\mu_0} \quad [\quad & \cos\theta g_1^0 \frac{-2R_\oplus^2}{r^3} + \\ + \quad & \frac{1}{4}(3\cos(2\theta)+1) g_2^0 \frac{-3R_\oplus^3}{r^4} + \\ + \quad & \frac{1}{8}(5\cos^3\theta + 3\cos\theta) g_3^0 \frac{-4R_\oplus^4}{r^5}] \end{aligned} \tag{2.9}$$

and

$$\begin{aligned} B_\theta = \frac{\partial \Psi}{\partial \theta} = \mu_0 \frac{1}{R_\oplus}\frac{R_\oplus}{\mu_0} \quad [\quad & -\sin\theta g_1^0 (\frac{-2R_\oplus}{r})^2 + \\ + \quad & \frac{1}{4}(3(-\sin(2\theta))\cdot 2) g_2^0 (\frac{R_\oplus}{r})^3 + \\ + \quad & \frac{1}{8}(5(-\sin^3\theta)\cdot 3 + 3(-\sin\theta)) g_3^0 (\frac{R_\oplus}{r})^4] \end{aligned} \tag{2.10}$$

On the Earth's surface ($r = R_\oplus$) equation (2.5) can be expressed as

$$\tan I = \frac{-B_r}{|B_\theta|} = \frac{2\cos\theta g_1^0 + \frac{3}{4}(3\cos(2\theta+1) g_2^0 + \frac{1}{2}(5\cos(3\theta+3\cos\theta) g_3^0}{|-sin\theta g_1^0 - \frac{3}{2}\sin(2\theta) g_2^0 - \frac{3}{8}(5\sin(3\theta) + sin\theta) g_3^0|} \tag{2.11}$$

It is more convenient to work with the latitude λ instead of the colatitude $\theta = \frac{\pi}{2} - \lambda$. Inserting this into equation (2.11) will interchange cosine and sine.

$$I = atan \frac{2\sin\lambda - \frac{3}{2} f_{21}(3\sin^2\lambda - 1) - 2 f_{31}(3\sin\lambda - 5\sin^3\lambda)}{|\cos\lambda - 3 f_{21}\cos\lambda\sin\lambda - \frac{3}{2}(cos\lambda - 5\cos\lambda\sin^2\lambda)|} \tag{2.12}$$

f_{21} and f_{31} are the fractions of the quadrupole to dipole and octupole to dipole dependent on g_2^0 and g_3^0.

With equation (2.12) for each latitute the adjunct inclination is found for the desired combination f_{21} and f_{31} and these inclinations are then transformed into poles. Of course this transformation to VGPs implies the assumption of a GAD field, but VGP calculations are also done on transitional fields to determine the VGP path of a reversal. S curves were generated for different multipolar contributions using an artificial set of directions (see Fig. 2.14).

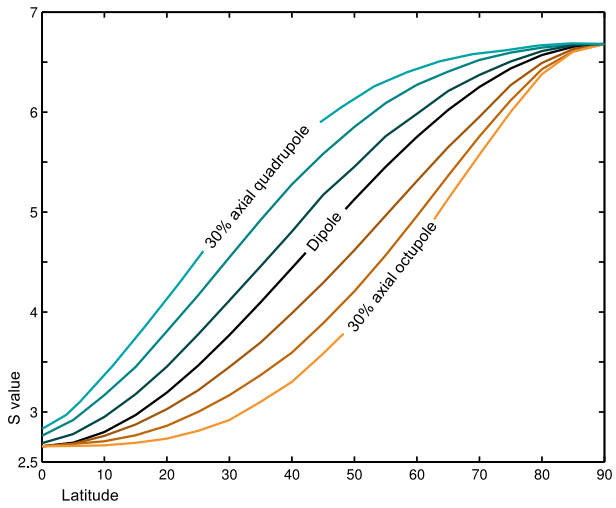

Figure 2.14: S curves for a purly dipolar field (black) and increasing axial quadrupolar (blue) and octupolar (orange) contributions.

For a growing percentage of an axial quadrupole the equatorial S value slightly rises and the slope gets shifted to lower latitudes, but the polar S value stays the same as for a pure dipolar field. For a growing axial octupole the S values at the equator stay the same, the slope also gets shifted to higher latitudes and again the polar S value stays the same.

Changes in the slope of S value are commonly attributed to a different geodynamo regime. Of course, on short timescales, the geocentric axial dipole (GAD) hypothesis is not sustainable as the Earth's magnetic field is not purely dipolar but has multipolar contributions. For the year 1990 the IGRF lists about 10% quadrupole component and 5% octupole component. But how persistent are such multipolar contributions? Does the observation of multipolar contributions in paleomagnetic studies mean that there were persistent multipoles or that a not long enough time window was sampled, for which the assumption of a GAD is

not true? And if the slope of the S(λ) does not change substantially but only gets shifted in our example, what does this slope mean and where does it stem from?

2.3 Outlook

In the study on sediments from Northern Peru we determined the equatorial paleosecular variation during the Cretaceous Normal Superchron using the S value. We chose Northern Peru, because it was at the equator in the Cretaceous. The S value we determined for this superchron is expected to be the minimum S as the S increases with latitude λ. The slope of S(λ) changes with time. McFadden *et al.* (1991) examined the different slopes for different times with studies from all over the globe being grouped into latitude bands. For example the slope S(λ) was found to be steeper during the Cretaceous Normal Superchron (here 80-110 Ma) compared to 110-195 Ma (McFadden *et al.*, 1991). However, a more robust determination of this slope could be ensured by several paleosecular variation studies on the same continent. To complement our study from Northern Peru more studies in the Cretaceous strata of the Western Cordillera southward of Peru would be perfect. The longitude would stay about the same, while only the latitude changes. Especially Cretaceous strata from Chile seems to be suitable for such a study as also the distance between possible sites stayed the same during the last 100 Ma.

But why the S value is in fact latitude dependent remained enigmatic to date. We will lift this secret in the next chapter.

3

Problems and pitfalls of the geomagnetic S-value

3.1 Latitude dependency of the geomagnetic secular variation S parameter: A mathematical artifact

This section 3.1 was published in *Geophysical Research Letters* in January 2012 under the title *Latitude dependency of the geomagnetic secular variation S parameter: A mathematical artifact* (Linder and Gilder, 2012, doi: 10.1029/2011GL050330).

Abstract

Secular variation, the change in the Earths magnetic field through time, reflects the energy state of the geodynamo. Secular variation is commonly quantified by paleomagnetists as the standard deviation of the angular distances of the virtual geomagnetic poles to their mean pole, known as the S value. This parameter has long been thought to exhibit latitude dependence [$S(\lambda)$], whose origin is widely attributed to a combination of time-varying dipole and non-dipole components. The slope and magnitude of $S(\lambda)$ are taken as a basis to understand the geomagnetic field and its evolution. Here we show that $S(\lambda)$ stems from a mathematical aber-

ration of the conversion from directions to poles, hence directional populations better quantify local estimates of paleosecular variation.

3.1.1 Introduction

Whether Earth or planetary dynamos can function in distinct regimes remains a fundamental yet unanswered question. For example, was the geodynamo acting during the Cretaceous normal superchron, when no reversal happened for ∼40 Myr, somehow unique or rather part of a statistical end-member from that acting over the past five Myr when one reversal occurred every ∼200 kyr? One way to solve this problem is to study the variability of the geomagnetic field, called paleosecular variation, which measures the convecting state in the outer core and reflects the time constants of the geodynamo (Cox, 1970; Bloxham and Gubbins, 1985). In contrast to a global description of secular variation provided by geomagnetic observatories or satellite records for a precise time or time interval, the paleomagnetic community is largely restricted to a local measure of paleosecular variation from single localities with poorly known temporal resolution. This way to define paleosecular variation is quantified via the dispersion in virtual geomagnetic poles, called the S parameter, defined as

$$S = \sqrt{\frac{1}{N-1}\sum_{i=1}^{N}\Delta_i^2} \tag{3.1}$$

which is the angular variance (in degrees) that each individual pole lies from the mean pole (Δ) (Cox, 1970). The S parameter has long been observed to vary with latitude [$S(\lambda)$], being about twice as high for sites near the poles than near the equator. Paleomagnetists commonly use S in two contexts. First, as a test of whether a population of paleomagnetic directions sufficiently averaged paleosecular variation, such that the average direction can be considered as being derived from a geocentric axial dipole field ((for some recent examples, see Opdyke *et al.*, 2006, 2010; Lawrence *et al.*, 2009; Kent *et al.*, 2010; Calvo-Rathert *et al.*, 2011)). In this case, workers calculate a local S value and compare it against S from a field model, usually that from McFadden *et al.* (1991), at the observed paleolatitude. Agreement of the two is used as proof that secular variation was sufficiently averaged. Second, changes in the slope of $S(\lambda)$ over geologic time are used as evidence that changes occurred in the energy state of the geodynamo (e.g. Irving and Pullaiah, 1976; McFadden *et al.*, 1988; Biggin *et al.*, 2008b,a; Haldan *et al.*, 2009) or to track the history of inner core growth (Smirnov *et al.*, 2011). Since

its introduction by Cox (1970), the reason for the latitude-dependency on S has remained an open question. Most workers evoke combinations of dipole and non-dipole components that vary in proportion, intensity and direction (Cox, 1970; Roberts and Stix, 1972; Baag and Helsley, 1974; McElhinny and Merrill, 1975; McFadden and McElhinny, 1984; Constable and Parker, 1988; Hulot and Gallet, 1996). For example, McFadden *et al.* (1988) explained the latitude dependency by dividing the geomagnetic field into its spherical harmonic coefficients based on whether they are asymmetric (e.g., the axial dipole) or symmetric (e.g., the axial quadrupole) about the equator. They argued that contributions from the asymmetric family are considered latitude-dependent whereas contributions from the symmetric family are constant over all latitudes. We show here that the latitude dependency of S actually stems from the non-linear conversion from directions to poles.

3.1.2 Demonstration of a Mathematical Artifact

To elucidate the problem, we generated a circular-symmetric distribution of directions on a stereonet (Fig. 3.1). The mean declination of this distribution was held constant while the mean inclination was shifted every 10°, going from 0 to 90°. In each case, we used the same number (N) of data points and the same precision parameter (k), which measures the dispersion of the population of directions from which the sample data set was drawn. At each inclination step, we converted the individual directions to virtual geomagnetic poles, and then calculated the corresponding S value. One observes that the geometrical configuration of the poles generated from circular-symmetric directions systematically deforms from circular at the geographic pole (ellipticity = 1) to oblate (ellipticity = 2) at the equator (ellipticity = [maximum axis minimum axis] / maximum axis). The maximum elongation direction is perpendicular to the site-pole meridian and the minimum elongation direction is parallel to it (Fig. 3.1). Importantly, it is seen that S mimics this pattern.

We then performed a similar test on Fisherian-distributed [Fisher, 1953] directions by varying k in steps of 6, 12, 25 and 125 (N held constant at 30). Eleven different Fisherian-distributed populations were generated for a fixed k value at ten different mean inclinations (0° to 90°). Each time, the directions were converted to poles and the S value was calculated. As seen above with the perfectly symmetrical distributions, the magnitude of S at a given latitude and the slope [S(λ)], are again dependent on k (Fig. 3.2): the smaller the k, the greater the pole to equator difference in S. Since Fisherian-distributed directions behave in the

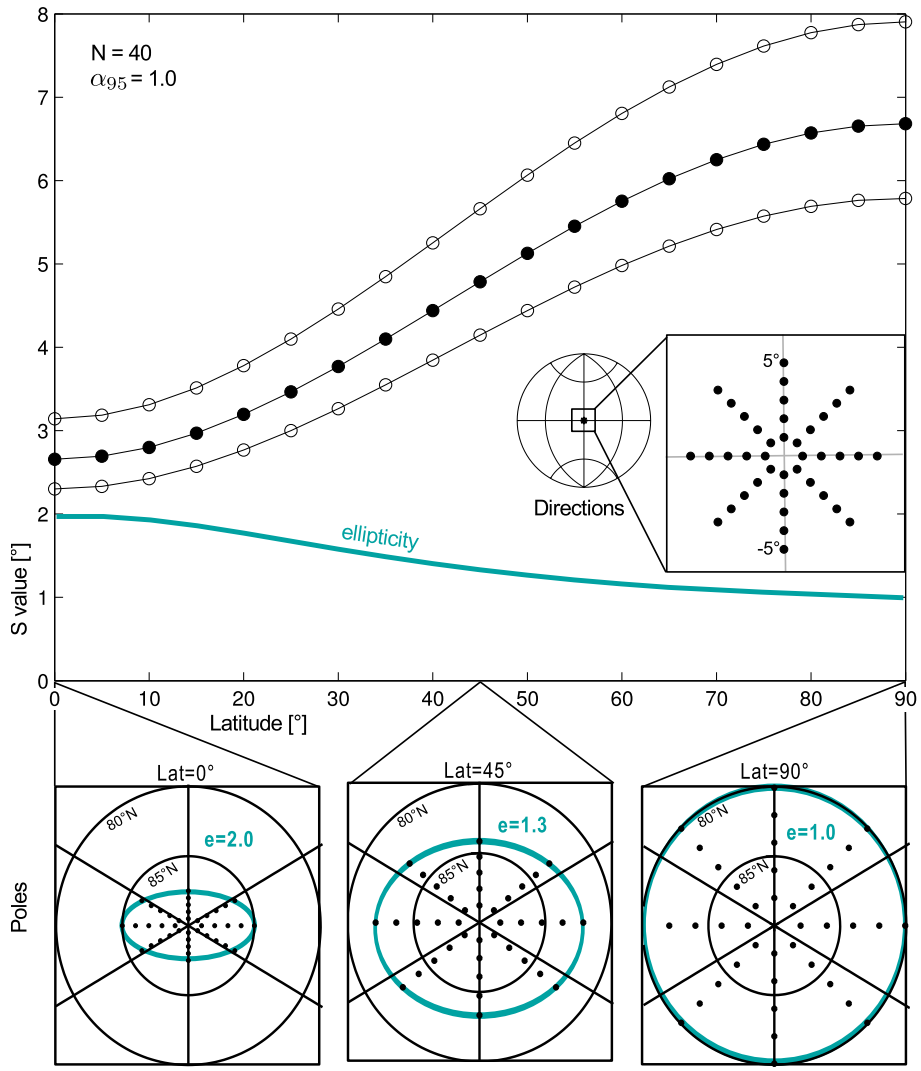

Figure 3.1: Circular-symmetric directions (N= 40) consist of rings of 8 points with the half-angle that the cone of confidence that the true mean direction lies within 95% confidence (α_{95}) fixed at 1°. The S values (solid black symbols) are shown together with their corresponding 95% confidence values (unfilled symbols calculated after Cox (1969)). Note that the Cox (1969) formulation for the uncertainties about S depends solely on N. Both S and the uncertainty about S increase with latitude. The geometrical distribution of the virtual geomagnetic poles calculated from these directions is also latitude dependent, with ellipticity ranging from 2 (latitude= 0°) to 1 (latitude= 90°) (blue line). Three virtual geomagnetic pole distributions, generated from directions at latitudes 0°, 45° and 90°, demonstrate the change in ellipticity and enlargement of the area encompassed by the mean pole.

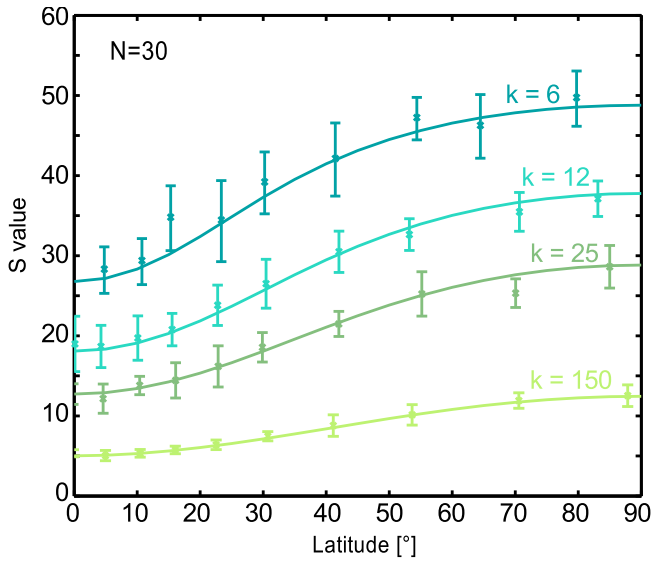

Figure 3.2: S value as a function of latitude calculated from directions with different k at constant N (N= 30). Solid lines are calculated from circular symmetrical distributions (same as in Figure 3.1); points are averages calculated from 11 Fisherian-distributed directions together with 1σ uncertainties of the 11 runs.

same way as synthetic symmetrical distributions, our next step was to examine real data. Only directions measured at geomagnetic observatories can fulfill the condition where the cadence in N remains constant over an identical time window. For this, we used monthly averages (Chulliat and Telali, 2007), which avoid diurnal signals and dampen the influence of magnetic storms. Moreover, there are enough observatories spread over sufficient latitude whose number of monthly averages span a duration long enough to perform a meaningful test. With this in mind, we chose a 26 year window from 1981 to 2006, corresponding to N= 312 monthly means from 74 observatories. We subdivided observatories into two categories based on gaps in the data: high N observatories (55 of 74) have less than 6 monthly averages missing, while low N observatories (19 of 74) have more than 6 monthly averages missing. The observatory directions were treated in the same way as paleomagnetic data: convert directions to virtual geomagnetic poles and calculate the S value as a function of geomagnetic latitude (Figure 3.3a). A 26-year magnetic record is substantially shorter than typical paleosecular variation timescales: directions and poles from the observatory records do not resemble Fisherian distributions. Nonetheless, the mathematical aberration during the conversion to virtual geomagnetic poles that produces the latitude dependency of the S value also affects these observatory data. As a verification, we calculated the mean N and k from the 74 observatories to calculate the expected latitude dependency on S. The observed and theoretical curves match quite well (Figure 3.3a).

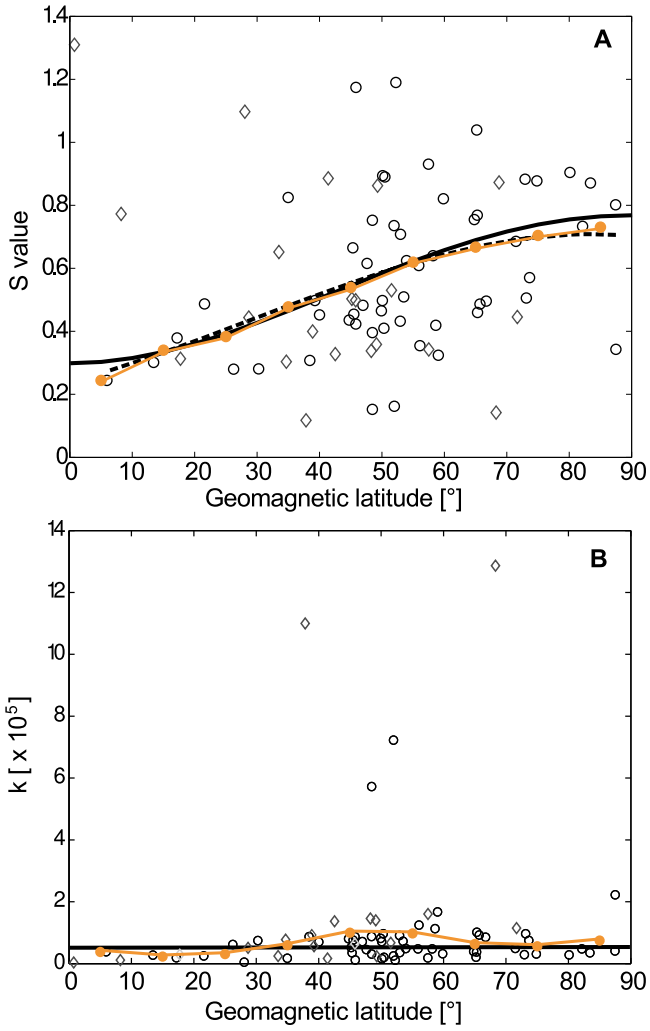

Figure 3.3: (A) S values calculated from monthly averages from 74 observatories from 1981 to 2006 as a function of geomagnetic latitude. Unfilled black circles represent high N observatories (less than six monthly averages missing) while unfilled grey diamonds observatories represent low N observatories (more than six monthly averages missing). Black dashed line shows the degree 2 polynomial fit of all data; orange circles connected by an orange line are average S values binned every 10° for high N observatories. Black solid line represents the expected S value as a function of latitude calculated from the average N (300) and k (53,000) from all observatories. (B) k versus geomagnetic latitude for the same observatory data with the same labeling as in 3.3A.

3.1.3 Discussion and Conclusion

Problems surrounding the conversion from directions to poles have long been recognized (Cox, 1970; Brock, 1971; Kono, 1997; Khokhlov *et al.*, 2001; Tauxe and Kent, 2004), but they were never associated with the S value. Our exercise implies that the latitude dependency of S owes its origin to a geometrical aberration from the mathematical conversion of directions to virtual geomagnetic poles and is not related to geomagnetic phenomena. This finding hearkens back the

oft-posed question whether poles or directions are more Fisherian distributed—a fact that is traditionally (Cox, 1962), yet arbitrarily (Kono, 1997), attributed to poles. Moreover, the conversion from directions to poles has the assumption of a dipolar field geometry built into it–defining secular variation directly from directional populations eliminates this assumption. So, which parameter should now be used to quantify secular variation from directions? Of the various options, k is likely the best choice, and the uncertainty on k(N) was already worked out (Cox, 1969). As long as N $\geq$15, uncertainties become low enough to make meaningful comparisons with k values from other studies. To confirm this, we return to the observatory data (Fig. 3.3b), where one observes that k remains constant as a function of latitude. Whether this remains true over geologic time needs to be confirmed. More certain is that k makes it easier than S to resolve the exact secular variation behavior. k has the advantage over S in that the squared term used to define S gives more weight to outlying points and S suffers from the ambiguity of virtual geomagnetic pole cut off latitudes. When enough paleomagnetic data are acquired in space for a given time, the local estimate of secular variation based on k can ultimately be replaced by a more accurate and global method to describe secular variation (e.g. Khokhlov *et al.*, 2006). That latitude dependence in virtual geomagnetic pole scatter curves owes its origin to a mathematical artifact has important implications for geomagnetism. In particular, it dispenses the notion that symmetric and asymmetric families are necessarily decoupled (e.g. McFadden *et al.*, 1988, 1991). Another implication of this study concerns the elongation/inclination (E/I) method that corrects paleomagnetic datasets for inclination shallowing (Tauxe and Kent, 2004). The foundation of this now widely used technique is based on a geomagnetic field model satisfying a specific latitudinal dependence on a circular distribution of virtual geomagnetic poles. Circular-symmetry of poles can be derived when directional populations come from a global distribution of site longitudes–this is not the case for individual studies. Converting poles back to directions distorts the geometric distribution of directions in the opposite way as shown in Figure 1; hence how the E/I correction works depends on S(λ). Future implementation of the E/I method could assume a Fisherian distribution of directions, regardless of latitude, based on k determined either directly from the site or from an average k value from several paleomagnetic studies covering a similar time range. Indeed, whether directional populations sufficiently average secular variation can be tested by their conformity to a Fisherian distribution.

Acknowledgements

We gratefully acknowledge the helpful and insightful reviews by Gauthier Hulot and an anonymous reviewer, as well as editorial handling by Michael Wysession. Financial support was provided by Deutsche Forschungsgemeinschaft grant GI712-2/2 and the THESIS Program of the Elite Network of Bavaria.

3.2 Addendum

Using today's observatory records secular variation is quantified using three different parameters: westward drift of the non-dipole parts of the field, changes in the non-drifting parts of the non-dipole field and changes in the strength of the dipole part of the magnetic field. For pre-observatory time this detailed description is not possible as the paleomagnetic data available are by far sparser and less spatially distributed.

Paleodirections measured in the laboratory are usually transformed to virtual geomagnetic poles (VGPs). These are the poles which would generate to the measured direction at the sampling site location under the assumption of a geocentric axial dipole (GAD). This transformation is done to be able to compare data sets from different sampling sites, as the inclination varies with latitude. Among other things VGPs are used to calculate the paleosecular variation. Traditionally, paleosecular variation is quantified by the S value, the standard deviation of the VGPs (Cox, 1962). This is clearly another procedure compared to the definition of secular variation from magnetic observatories. Thus, we treated the observatory data the same way a paleomagnetist would treat his directions and we could show that also today's observatory records reveal a latitude dependency of the S value.

However, we proposed to quantify paleosecular variation using directions and not poles (Linder and Gilder, 2012). Compared to poles directions have two advantages. The dispersion of directions from studies from different latitudes can be directly compared as no latitude dependency has to be accounted for. And also the assumption of a purely dipolar field when converting paleomagnetic directions to VGPs can be neglected. This assumption is only true when averaging of long enough time spans (>10 kyr). Volcanics might have erupted in less time. This basic assumption of a GAD contradicts to the conclusions commonly drawn from several paleosecular variation studies: If a S value is found lower than expected a common conclusion is that the field was less dipolar during this time, even though a purely dipolar field which was assumed to determine the poles from the directions in the first place.

Thus quantifying paleosecular variation using directions minimizes the unknowns. But which parameter should now replace the S value? The presentation of several parameters in the following paragraphs is mainly based on books of Butler (1998), Tauxe (2005) and Stahel (2009).

Different approaches to quantify dispersion of directions (or points on a unit sphere) exist. Most of them are based on the resultant vector R of a collection of

N declinations D and inclinations I (D_1, D_2, D_3, ..., D_N and I_1, I_2, I_3, ... I_N). The sum of the unit length vectors in cartesian coordinates from the origin of the unit sphere to the points on its surface is defined as the resultant vector

$$R = \sqrt{(\sum_{i=1}^{N} x_i)^2 + (\sum_{i=1}^{N} y_i)^2 + (\sum_{i=1}^{N} z_i)^2} \tag{3.2}$$

with $x_i = \cos I_i \cos D_i$, $y_i = \cos I_i \sin D_i$ and $z_i = \sin I_i$ being the direction cosines of the i vector with respect to north, east and down. In paleomagnetism dispersions of data are mostly described using parameters from Fisher statistics. The Fisher probability density function (Fisher, 1953) is defined as

$$F_{dA(\theta)} = \frac{\kappa}{4\pi \sinh \kappa} exp(\kappa \cos \theta) \tag{3.3}$$

and describes the probability to find a direction in a unit area dA which is θ away from the center of the distribution. However, the precision parameter κ is only defined for a Fisher distribution with an infinite number of samples, for a real collection of data with a finite number of samples the best estimate k of κ is defined as

$$k = \frac{N-1}{N-R} \tag{3.4}$$

with the number of samples N and the resultant vector R from equation (3.2). This parameter k is used in paleomagnetism to quantify the dispersion of directions. From equation (3.4) it is obvious that for a R approaching N, a denser clustering of the data, k increases. A problem with k is its exponential character: Two loose dispersed data sets with for example $k = 10$ and $k = 25$ have a difference of of 15 and can be easily distinguished by eye, but two denser clustered data sets with $k = 400$ and $k = 600$ have very different ks but look essentially the same to a human eye. Another parameter from Fisher statistics usually used in paleomagnetics is the half-angle of the cone of 95 % confidence (confidence limit)

$$\alpha_{95} \approx \frac{140^\circ}{\sqrt{kN}} \tag{3.5}$$

This parameter can be seen as an analogue to the 2σ standard deviation in Gaussian statistics to the mean direction of the sample collection. Thus, even though often assumed, α_{95} is not a direct measure of dispersion but a measure of how well the mean of a data set is defined. Also, α_{95} is only reasonably reliable for a $N \geq 10$ and $k \geq 10$ or 25 (Butler, 1998; Tauxe, 2005) The more seldom used

circular standard deviation (also called angular dispersion in some literature) is approximated by

$$s \approx \frac{81^\circ}{\sqrt{k}} \tag{3.6}$$

Within this angle from the true mean 63 % of the data of a Fisherian distribution are contained, which differs from the 68.3 % which lie within the 1σ standard deviation of a one dimensional normal distribution.

Another analogue to normal distributions is the angular standard deviation

$$S = \sqrt{\frac{1}{N-1}\sum_{i=1}^{N}\Delta_i^2} \tag{3.7}$$

with Δ being the angular distance of an individual pole to the mean pole. S is traditionally used to quantify paleosecular variation using poles. The angular dispersion factor

$$\delta = \cos^{-1}\frac{R}{N} \tag{3.8}$$

was introduced by Wilson (1959) and takes a value of $\delta = 0^\circ$ when all vector are parallel, thus it is proportional to the scatter

One more parameter which is not related to a Fisherian distribution is the to the parameter circular variance

$$\sigma = 1 - \frac{R}{N} \tag{3.9}$$

As the mean resultant length $\bar{R} = \frac{R}{N}$ will approach 1, when the vectors are tightly clustered to the maximum, mean exactly parallel. Thus, a σ close to zero is a dense data set and sigma increases with the scatter of the data.

Another concept to quantify the scatter of directions on a sphere is based on the eigenvalues. For this the declinations D and inclinations I are converted to cartesian coordinates.

$$x_i = \cos D_i \cos I_i \qquad y_i = \sin D_i \cos I_i \qquad z_i = \sin I_i \tag{3.10}$$

The "center of mass" of each component is determined

$$\bar{x} = \frac{1}{N}\sum_{1}^{N} x_i \qquad \bar{y} = \frac{1}{N}\sum_{1}^{N} y_i \qquad \bar{z} = \frac{1}{N}\sum_{1}^{N} z_i \tag{3.11}$$

and used as a new origin of the transformed data

$$x'_i = x_i - \bar{x} \qquad y'_i = y_i - \bar{y} \qquad z'_i = z_i - \bar{z} \tag{3.12}$$

The orientation tensor of the transformed data set is

$$O = \begin{pmatrix} \sum x'_i x'_i & \sum x'_i y'_i & \sum x'_i z'_i \\ \sum y'_i x'_i & \sum y'_i y'_i & \sum y'_i z'_i \\ \sum z'_i x'_i & \sum z'_i y'_i & \sum z'_i z'_i \end{pmatrix} \tag{3.13}$$

The maximum eigenvalues of **O** is the mean direction and the intermediate and minimum eigenvalue are the confidence ellipse around this mean direction. However, for small data sets, which are frequent in paleomagnetic studies, the calculation of the eigenvalues can be erroneous. This procedure is used in paleomagnetism in the principal component analysis (PCA) and the maximum angular deviation (MAD).

Which of all those parameters is now best used to quantify the dispersion about the mean direction? A perfect parameter to quantify paleosecular variation would be

- independend on latitude
- independend on the number of samples N
- robust to single outliers
- without any assumption of the underlying distribution e.g. Fisherian distribution
- not dependent on models like GAD

Creer (1962) quantified the dispersion of directions using δ (see equation 3.8). He also found δ to be latitude dependent. However, the directions for this study were derived from the interpolated field measured at observatories in 1945. This means that the directions were calculated from the poles. Because of the conversion problem between directions and poles, of course these calculated directions end up to be latitude dependent.

σ seems to be a more straightforward parameter compared to δ, due to its simplicity and the proportionality to the scatter of the data.

When comparing paleomagnetic studies the number of samples is seldom the same. Several methods to deal with this problem exist. The most frequent used

method is the F-test (Snedecor and Cochran, 1989), which compares the variances of two distributions S_a^2 and S_b^2 by calculation of the ratio

$$\hat{F} = \frac{S_a^2}{S_b^2} \tag{3.14}$$

for $S_a^2 > S_b^2$. This ratio is compared to a tabled critical F-value, which depends on the degrees of freedom and a significance level. If $\hat{F}$ is smaller than the critical F-value the two variances are not significantly different. Applied to paleomagnetism, this would mean the paleosecular variation determined from two different studies is the same. However, the problem with the F-test is that the sample sizes should be above N=30, which is seldom realistic, especially for volcanic studies.

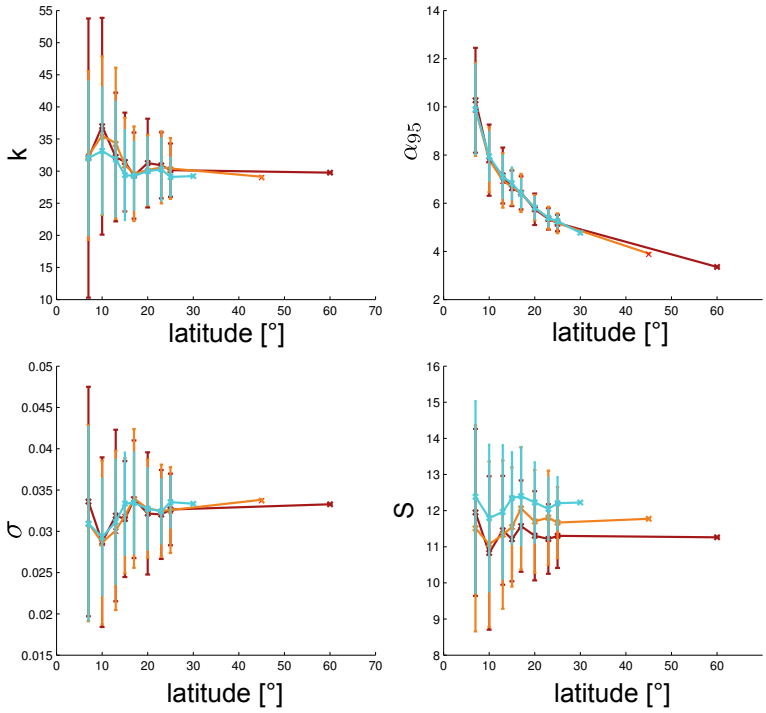

Figure 3.4: Delete-m jackknife method on three starting populations (N=60 red, N=45 orange, N=30 blue). Resampling $N_r = 30, ..., 7$ and calculation of the four dispersion parameters k,α_{95}, σ and S.

Another method are the confidence limits for the S value and k (Cox, 1969) which are based on the number N of records. Here for each study error bars of the S value or k a determined, which are solely dependent on N. But especially for small numbers the error bars can get as large as double to initial value.

If the paleomagnetic community could agree on a reference N, meaning a minimum N needed for a study to be taken into account for paleosecular variation

records, a Monte-Carlo technique could be applied to data sets with larger $N > N_{reference}$. This method will artificially reduce the data volume of the study with high N, if a record is longer than $N_{reference}$ and thus making it possible to compare these two studies.

Using this method the independence of some of some dispersion parameters from the number of samples (N) will now be tested. We chose σ and the well established parameters k and α_{95} for this. Data sets with different N (30, 45 and 60) were created and were resampled with smaller N_r (Fig. 3.4). What can be seen is that α_{95} is not robust to the number of samples N, as it increases with decreasing number of samples in the subset. Thus, k or σ are likely the best choice. Here we decide for k to be the parameter to use to quantify the dispersion of paleomagnetic directions, as N-dependent error bars have already been worked out for k (Cox, 1969).

However, comparing paleosecular variation from different studies has more problems involved than just deciding what is the best parameter to describe paleosecular variation from directions and also what should be the minimum N. A not so trivial question is what time window should be represented. Obviously, two data sets which consist of the same sample number N but represent different time spans, e.g. 10 kyr or 3 Myr, cannot be compared as also the paleosecular variation has a temporal variation. One possibility would be to also agree on a minimum time span represented.

3.3 Outlook

When decisions about minimum sample numbers and time represented are made the paleomagnetic database can be used to study temporal variation of paleosecular variation of the last 200 Ma similar to McFadden *et al.* (1991), but using directions. Especially with the exact time length represented in a study a lot of literature work has to be done.

4

Geodynamo energy regime inferred from paleointensity

4.1 Cretaceous paleointensity from Ecuador and Northern Peru

Abstract

The paleointensity of the Cretaceous Normal Superchron has been studied using volcanics from Ecuador and Northern Peru. Two different methods of paleointensity determination were used, a modified Thellier-Thellier method and the Dekkers-Böhnel method. 15 of 16 sampled sites were affected by maghemitization of the remanence carriers. However, one single site of the Piñon Formation (88.8 ± 1.6 Ma) gave reliable results. A weighted mean paleointensity of 28.2 ± 8.1 μT was determined with the Thellier-Thellier method and 35.1 ± 8.7 μT with the Dekkers-Böhnel method. The virtual dipole moments are calculated to be 68 ± 20 ZAm^2 and 85 ± 21 ZAm^2, respectively. These two values agree well with each other, as the error bars are overlapping and contain the mean value of the other method. Thus, a reliable paleointensity result is suggested. Our obtained virtual dipole moments do not differ from today's magnetic moment of the Earth.

This suggests that there was no special geodynamo regime during the Cretaceous Normal Superchron.

4.1.1 Introduction

The Cretaceous Normal Superchron (CNS, about 84-125 Ma) represents a time in Earth's magnetic history, when the field did not reverse its polarity for about 40 million years. In contrast the mean reversal rate during the past 5 million years is about 5 times per million years. A common theory is that the geodynamo was in a different 'energy state' during this superchron, triggered by changes of the heat flux across the core-mantle boundary. The primary goal of this thesis is to determine the energy state of the geodynamo during the CNS. Both, paleosecular variation and paleointensity are supposed to be a window into past energy regimes of the geodynamo. From paleosecular variation of sediments from Northern Peru, we could not conclude a different energy regime for the CNS (Linder and Gilder, 2011). However, a lot of open questions remained, especially whether paleosecular variation is a suitable parameter to characterize the Earth's magnetic field at all. Here we concentrate on the other parameter used to infer the energy regime of the Earth's magnetic field: the absolute paleointensity. To complement the Northern Peru sedimentary study we chose to sample nearby volcanic rocks in Northern Peru and Ecuador. Most previous paleointensity studies on the South American continent were done in Brazil, Uruguay and Argentina (Cejudo Ruiz *et al.*, 2006; Goguitchaichvili *et al.*, 2008; Cejudo Ruiz *et al.*, 2009; Cervantes Solano *et al.*, 2010). Out study on the contrary is on volcanics from the western margin of the continent and the Cordillera. The ages of the Cretaceous strata we sampled correspond to both, the beginning and the end of the CNS, which offers a look into the very interesting energy regime that possibly marked the end of the superchron.

4.1.2 Geology

Cretaceous geology of Ecuador is closely related to the geology of the Caribbean. 90-87 Ma ago the large igneous province (LIP) Colombian Caribbean Oceanic Plateau (CCOP) extruded in equatorial to shallow latitudes (2°N to 5°S) (Luzieux, 2007) within the Farallon plate, presumably above the Galapagos hotspot, and drifted towards the east. The oblique collision with the western margin of the South American continent fragmented this LIP. Proposed ages for this collision range from early Campanian to Eocene (80-35 Ma (Benitez, 1995)) or 73-70 Ma (Luzieux, 2007). Accreted terranes were left behind along South American coast

when the bulk of the CCOP moved N-NE. The CCOP could not be subducted at the Middle-America Trench, but overrode the Atlantic plate. It moved through the gap between the North American and South American continents (Pindell and Kennan, 2009) and forms the Caribbean plate today.

In Ecuador strata of CNS age can be found today in the form of mafic basement rocks (see Fig. 4.1). The Pallatanga Formation in the Sierra (87.1 ± 0.8 Ma, U/Pb zircon age from Vallejo Cruz, 2007) and the Piñon Formation in the Costa (88.8 ± 1.6 Ma, 40Ar/39Ar analysis of hornblende from Luzieux, 2007) have indistinguishable ages and similar geochemistry, suggesting that both are fragments of the same accreted terrane. Additionally, these Ecuadorian basement rocks show almost the identical shallow inclinations (Luzieux, 2007), geochemical characteristics and ages (91-88 Ma) as rocks from the Caribbean (Sinton *et al.*, 1998).

Even though the geological history of the CCOP does not sound very promising for preserving a magnetic signal, Luzieux (2007) showed that the Cretaceous strata in the Costa could be used for the determination of paleomagnetic directions. In the Western Cordillera the stratigraphic setting of the Cretaceous strata often remained unclear (Vallejo Cruz, 2007), which does not hinder the determination of the intensity of the Cretaceous magnetic field from unoriented hand samples of this area.

A detailed description of all Ecuadorian sites with maps, photographs and rockmagnetic characterization can be found in the Appendix B.

Piñon Terrane

In the Ecuadorian Costa the strata of Cretaceous Normal superchron age consist of mafic basement rock with gabbros, columnar basalt and pillow lavas. This Piñon Formation (88.8 ± 1.6 Ma, 40Ar/39Ar analysis on hornblende from Luzieux, 2007), which represents this mafic basement of the accreted Piñon Terrane, is overlain by volcanic arc rocks and marine hemipelagic depositions. These younger island arc volcanics (Las Orquideas Formation, $\sim$84 Ma, from magnetostratigraphic dating and macropaleontology, Luzieux, 2007) document the collision (Luzieux, 2007). The Las Orquideas Formation and the Piñon Formation cannot be distinguished unequivocally in the field (Luzieux, 2007), which means there is a risk of sampling rocks younger than 88.8 Ma.

We focused on sampling the Piñon Formation in the Costa and followed mainly the sites described in (Luzieux, 2007). Near Guayaquil we took samples of 4 sites (LMC, SAB, CGE, CCO), another 3 sites were sampled in the Manta region (CMC, CHW, CHE) and 3 more sites in the Pedernales region (PED, VEN, SRO).

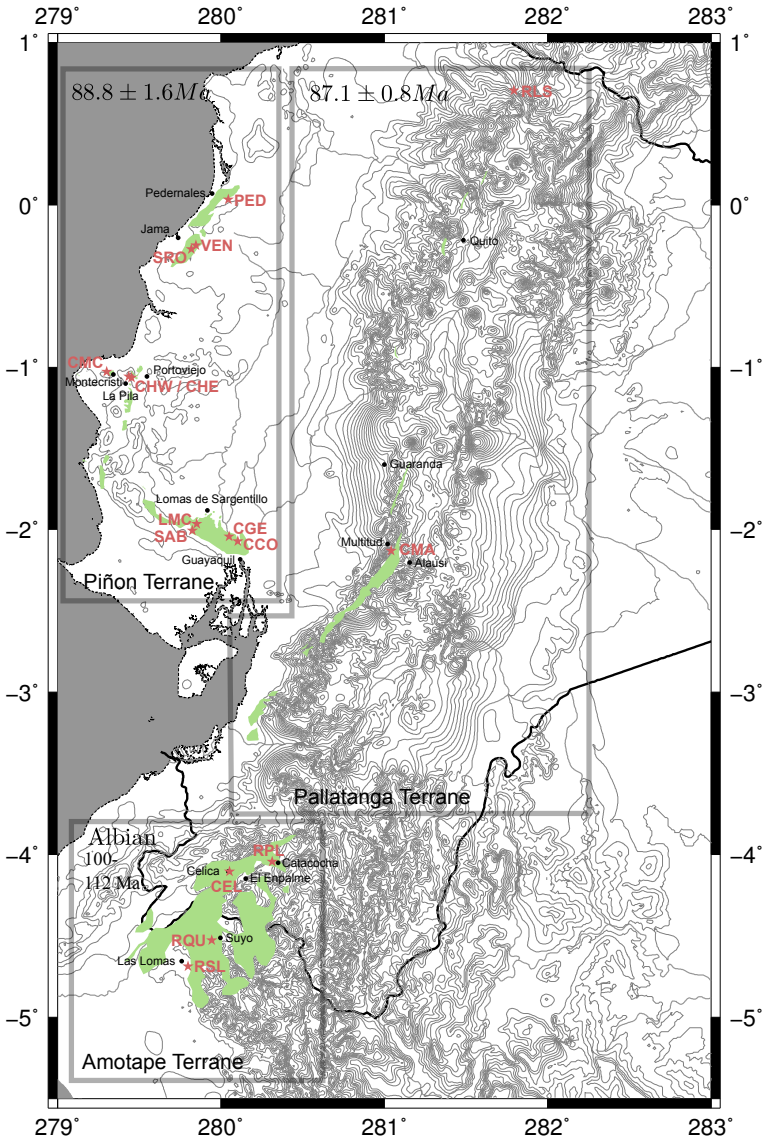

Figure 4.1: The border between Ecuador and Northernmost Peru is marked by a thick black line. Grey lines denote the contour lines in 200 m intervals. Simplified in green are the sampled formations from the Cretaceous Normal Superchron: the Piñon Formation (Luzieux, 2007), the Pallatanga Formation (Vallejo Cruz, 2007) and the Celica Formation (Pilatsig *et al.*, 2008). Grey boxes border the three different Piñon, Pallatanga and Amotape terranes and the ages of their Cretaceous strata. Red stars denote our sampled sites Pedernales (PED), Venado (VEN), San Rocque (SRO), Cerro Montecristi (CMC), Cerro de Hoja West and East (CHW and CHE), Las Mercedes (LMC), Sabaneta (SAB), Cerro Germania (CGE), Cerro Colorado (CCO), Rio Liot Salinas (RLS), Cordillera Multitud Alausi (CMA), Rio Playas (RPL), Celica (CEL), Rio Quiroz (RQU) and Represa San Lorenzo (RSL). Black dots denote nearby cities and villages to our sites.

Pallatanga Terrane

Cretaceous strata in the Western Cordillera with ages within the Cretaceous Normal Superchron consist of mafic basement rock overlain by late Cretaceous volcanic arc rocks and sediments. The Pallatanga Formation (87.1 ± 1.66 Ma, U/Pb SHRIMP on zircons in layered gabbro from Vallejo Cruz, 2007) is part of the basement rocks. We sampled one site of Pallatanga Formation at the road from Multitud to Alausi (CMA, Fig. 4.1). Additionally, we took samples north of Quito from the La Portada Formation at the road alongside Rio Liot near Salinas (RLS). The Pallatanga Terrane and the Piñon Terrane are presumably the same (Luzieux, 2007).

Amotape terrane

The Ecuadorian-Peruvian border region between the Huancabamba Fault and the Grijalva Fracture Zone is not part of the North-Andean Piñon Terrane. During the Albian (Hungerbuhler *et al.*, 2002) a subduction related volcanic arc developed at the western margin of the South American continent between the Paleozoic Amotape massif and the Olmos massif, a prolongation of the Cordillera Occidental (Mourier *et al.*, 1988a). Today rocks from this volcanic arc can be found in the Celica-Lancones basin. The Celica Formation consists of andesitic, basic-intermediate volcanic rocks. The age is estimated to be Aptian-Albian, concluded from a crosscutting batholith (K-Ar ages from plagioclase and hornblendes: 114-110 Ma Jaillard, 1996b). This age places these volcanics at the beginning of the superchron, which makes them an interesting supplement to the volcanics from the Piñon Terrane from the end of the superchron. We sampled 4 sites in these Albian volcanics, two in Ecuador (RPL, CEL) and two in Peru (RQU, RSL).

4.1.3 Paleomagnetic methods and results

Paleointensities I: Thellier-Thellier method

For the determination of paleointensity subcores of the samples were subjected to the classical Thellier-Thellier method (Thellier and Thellier, 1959; Coe, 1967) with alteration, additivity and tail checks (Leonhardt, 2004). 5 mm diameter subcores were heated to 14 temperature steps using a laboratory field of 30 μT in the Shaw furnace and measured at the 2G Cryogenic Magnetometer in the laboratory at Niederlippach.

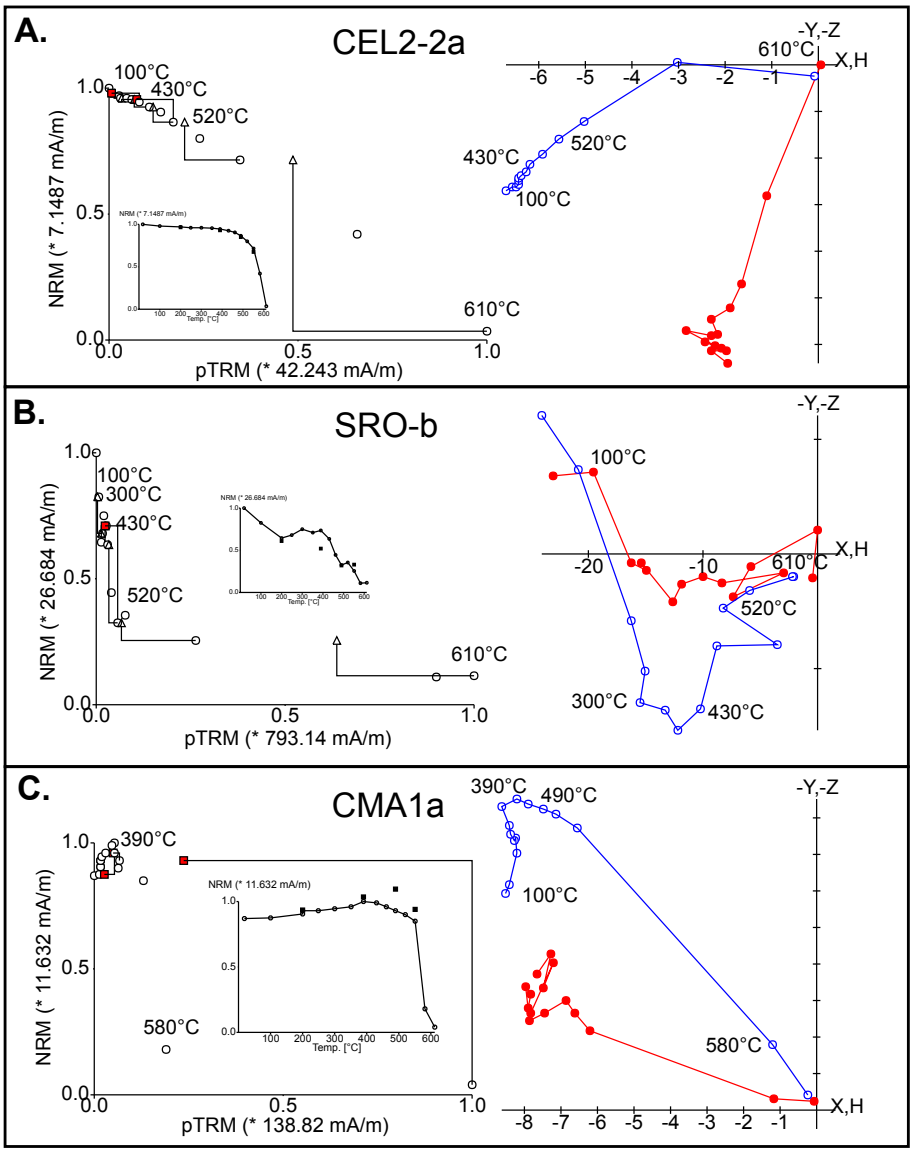

Figure 4.2: Shown are Arai, thermal decay and orthogonal plots of direction during the Thellier-Thellier experiments for three representative samples, from which no paleointensities could be determined. The orthogonal plots did not show a stable component to the origin for the samples CEL2-2a and SRO-b. Also for all three samples the check corrections were not successful.

The success rate of the Thellier-Thellier method on the 57 Ecuadorian-Peruvian samples was only 18%. For 35% the orthogonal plots showed no stable remanence component (Fig. 4.2 a and b). Mostly the problem was an overprint: only the last few demagnetization steps made up the characteristic remanence pointing to the origin. For another 4% of the samples incomplete demagnetization (final step was 610°C) was the problem. For 13% strong alterations as indicated by deviating partial thermal remanences (pTRM) were observed and check correction failed to improve the Arai plots (Fig. 4.2). Check corrections assume that all deviations of the alteration checks from the best fit line are generated by a newly formed mineral phase while the original remanence carrier stays unaffected (Leonhardt, 2004). However, it seems that in our samples the main remanence carrier is affected by an uncorrectable alteration and thus these samples should not be used for paleointensity determination.

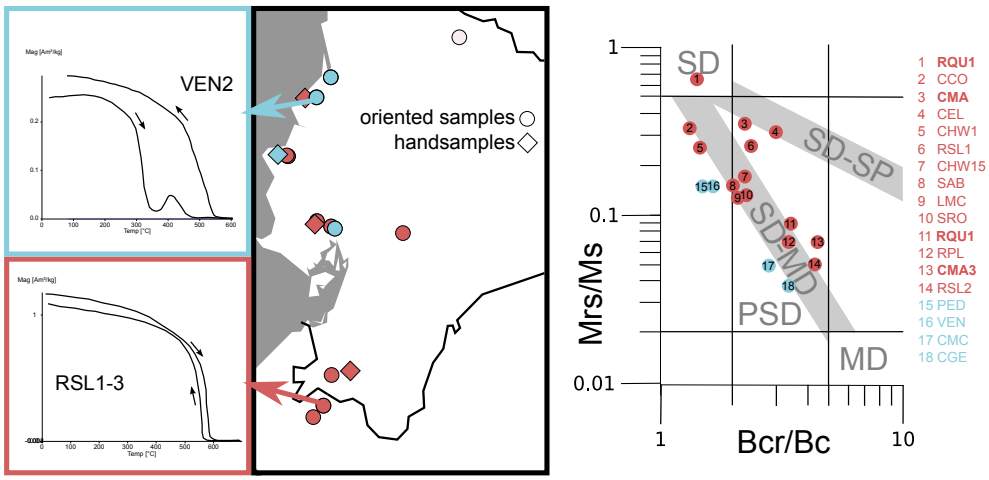

Figure 4.3: Red dots on the map of Ecuador are sites for which thermomagnetic experiments show a magnetite-like Curie temperature. Blue dots are sites with lower Curie temperatures. White dots sites where strong paramagnetism masked the Curie temperature. To the left thermomagnetic heating and cooling curves for some representative sites are shown. To the right rock magnetic results are plotted in a Day plot with the SD-MD and SD-SP mixing lines shown in gray.

In 25% of the cases alteration occurred early during the measurements. Thermomagnetic measurements with the VFTB (Magnetic Measurements) should help to identify the remanence carriers. In most cases it is magnetite, indicated by a Curie temperature of 580°C determined with the second deviation of the thermal

decay. But also lower Curie temperatures were found for some sites with a subsequent alteration to magnetite above 400 °C (PED, VEN, CMC, CHW/CHE; see fig. 4.3). This could be interpreted as an indication of pyrrhotite, a iron sulphide occasionally occurring in basic igneous rocks or formed in high-temperature hydrothermal systems. Ore microscopy offers the chance to observe the remanence carrier directly. Both, cruciform and euhedral structures typical for titanomagnetite were observed (see Appendix B) as well as shrinkage cracks. These indicate low-temperature oxidation with an associated volume reduction of the titanomagnetites (Petersen and Vali, 1987). The Curie temperature of MORB titanomagnetites is ∼150°C. We observe higher Curie temperatures between 300-400°C. Due to these Curie temperatures, the mineral shapes and shrinkage cracks we argue for metastable titanomaghemites, which invert to magnetite upon heating above ∼300°C (Özdemir and O'Reilly, 1982), to be the remanence carrier. These titanomaghemites might have formed during the low-temperature oxidation from MORB titanomagnetites. From the elevated Curie temperatures the oxidation parameter z can be estimated to be 0.4-0.8 (Özdemir and O'Reilly, 1982)

Often our measurements sag below the ideal single domain (SD) line in the Arai diagram – a hint to the prevalence of multi-domain (MD) particles. This complicates the determination of a robust paleointensity value using the Thellier method. Hysteresis measurements can unveil the domain state. Most samples plot in the pseudosingle domain (PSD) range along the SD-MD mixing line in the Day plot (see Fig. 4.3). Thus, the real domain state of the samples does not need to be PSD, but instead a mixture of SD and MD grains can make them appear like PSD. Apart from the samples of the sites VEN and PED, no visible grouping of samples from the same area could be observed. On the contrary, even within one site a wide spectrum of domain states can appear (see e.g. RQU and CMA in Day plot of Fig. 4.3). Thus, most likely a mixture of SD and MD particles prevail in the samples.

Only from the site CCO almost all samples could be used to successfully determine a paleointensity (Fig. 4.4). The values show a high dispersion, but the mean $\bar{F}$ for those 4 lava flows is 26.2 μT (see Table 4.1). Using the quality factor q the weighted mean $\bar{F}_q = \frac{\sum F \cdot q}{\sum q}$ for this site is 28.1 μT.

Paleointensities II: Dekkers-Böhnel method

Recently, an alternative method to determine paleointensities was developed, which does not need the samples to be single domain (Dekkers and Böhnel, 2006). As opposed to the Thellier-Thellier method, which keeps the laboratory field con-

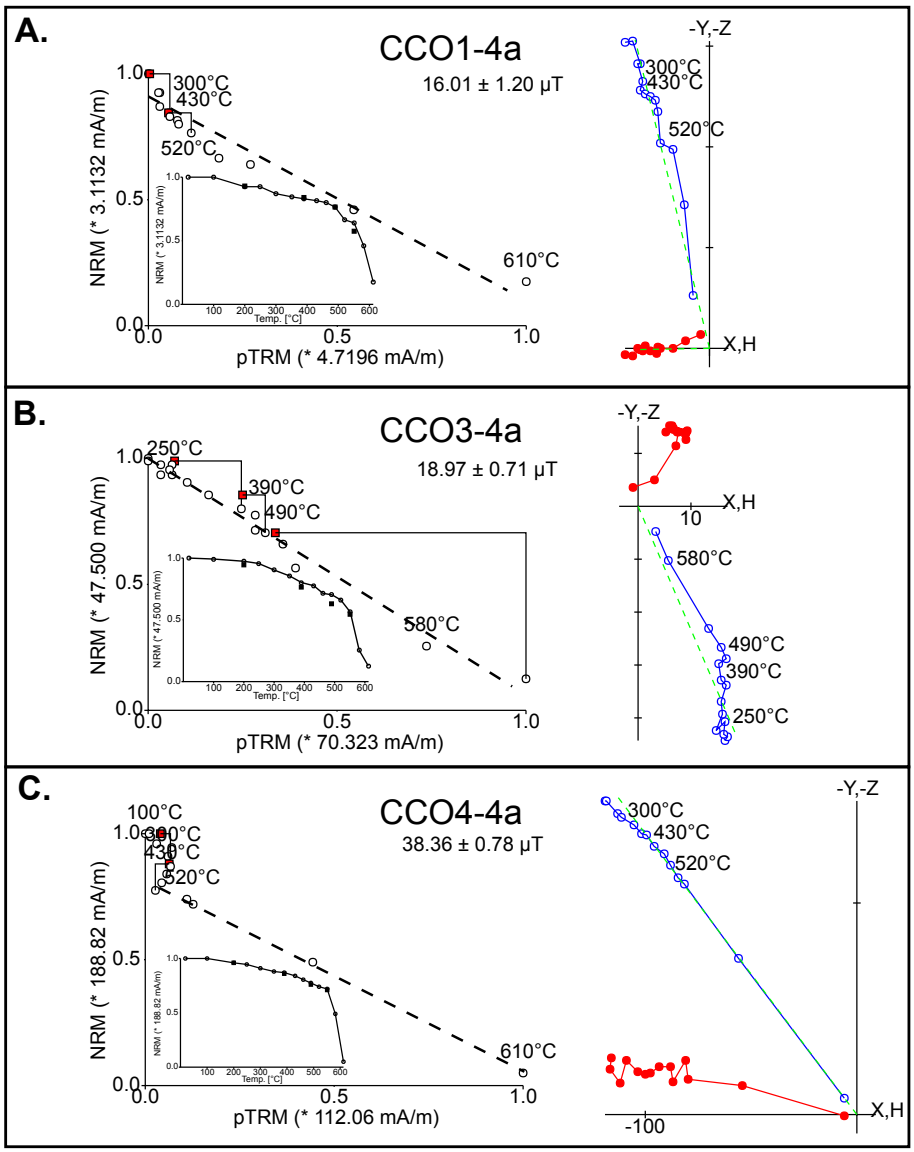

Figure 4.4: Shown are Arai, thermal decay and orthogonal plots of the direction during the Thellier-Thellier experiments for three representative samples from site CCO with the calculated paleointensity. Subcores were drilled unoriented, thus no paleodirectional information can be extracted from the orthogonal plots.

Sample	F [μT]	σF [μT]	class	T_{min} – T_{max}	N	f	g	q	δ_{AC}	δ_{TR}
CCO1-1	20.5	2.6	B	20 – 550	12	0.30	0.86	2.05	0.12	8.80
CCO1-4	16.1	1.1	B*	300 – 580	9	0.48	0.70	4.72	0.35	7.74
CCO2-3	38.2	4.6	B*	20 – 580	13	0.63	0.88	4.59	2.64	8.09
CCO3-4	20.7	0.8	B*	20 – 580	14	0.74	0.77	14.17	8.89	7.58
CCO4-4	35.5	1.1	B	460 –610	6	0.91	0.58	17.34	0.45	2.38
$\bar{F}$	26.2	8.1								
$\bar{F}_q$	28.2	8.1								

Table 4.1: Results of the Thellier-Thellier experiments for Site CCO. Shown are sample name, paleointensity F with standard deviation σF, Arai plot class after Leonhardt (2004), temperature range of evaluated segment of Arai plot, number N of measurement point used for the determination of paleointensity, and various parameters after Leonhardt (2004) and Coe *et al.* (1978): fraction parameter f representing the used fraction of the NRM, gap parameter g ranging from 1 to 0 describing the width of the gaps between successive measurement steps, quality parameter q calculated to be f multiplied by g divided by the scatter of data points around the regressed line, additivity check error δ_{AC} and thermal repeat check error δ_{TR}. Below the line the mean and q-weighted mean are given.

stant during the experiment but changes the applied temperature steps, the alternative method works the other way round: the laboratory temperature is kept constant and varying field steps are applied. Additionally, a new subcore is used for each field step to prevent alteration effects by multiple heating of the samples during the measurement.

A problem with the multi-specimen method for us was that sister-samples from the same drillcore are needed. For the majority of sites drillcores were too short for sister-samples or they were already used for other measurements. The paleodirections of 25 samples from 8 sites directions were measured on oriented cores using the ASC Oven and the SushiBar in the Munich paleomagnetic laboratory. Results of paleodirections will be presented in the Discussion.

19 samples were chosen to be eligible for the Dekkers-Böhnel method as they showed a stable characteristic remanence. From their sister-samples subcores of 7mm diameter were drilled in the direction of the characteristic remanences. The wider 7mm diameters were chosen for the Dekkers-Böhnel method as this facilitates to orient the subcores and they are more representative of the bulk rock. When measured in the 2G cryogenic magnetometer the NRM of the subcores can now deviate from I=90° as viscous overprints had to be removed by heating the subcores to a core-specific temperature in the ASC oven in the laboratory Munich.

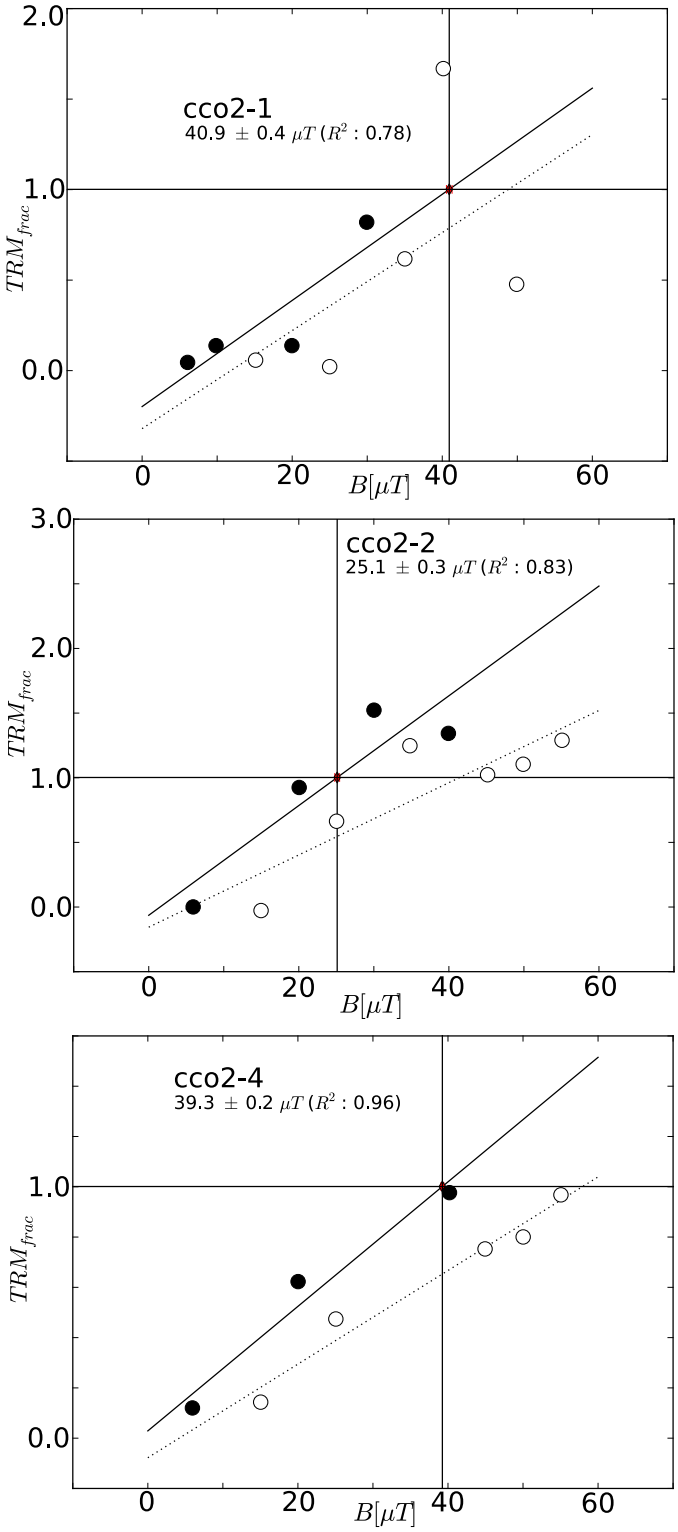

Figure 4.5: Results of the Dekkers-Böhnel method to determine paleointensity. Shown as black circles are the fractions of thermal remancence (TRM) imprinted at a specific laboratory field. The black line shows the best fit through these points. A red symbol denotes the calculated paleointensity with the 1-σ error. The white symbols with the dotted fit line are additional steps on reheated samples but were not used for the evaluation, as they would induce an overestimation of the paleointensity.

The cleaned remanence is used for normalization of the pTRM imprintment. A laboratory temperature of 350°C was chosen, which was within the characteristic remanence (ChRM) of all samples or at least the best compromise. Laboratory field steps from 5μT to 60 μT were applied to the samples with a solenoid in the ASC oven. For each field step 5 different measurements were made: the magnetization without any field applied (m0), with the laboratory field applied in z-direction (m1), anti-parallel to the z-direction (m2), parallel to the z-direction with zero field heating (m3) and the repeat of step m1 (m4) (Fabian and Leonhardt, 2010).

As for each field step a new subcore is needed, we tried to improve the number of measurement steps by reusing subcores for different pTRM. These repeat-steps are marked with open symbols in Fig. 4.5 as opposed to solid symbols for first steps. Interestingly, the reheated steps gave higher paleointensites than the initially heated steps. This could be due to alteration or improper alignment of the field with the z-direction. The alteration error ϵ_{alt} is calculated from the steps m1 and m4. For the m4 step a sample was heated to T_{lab} three times before. The high alteration errors (see Tab. 4.2) make our check steps unusable, but we still rely on our m0 and m1 steps for the classical Dekkers-Böhnel protocol, as the alteration might have taken place during the reheated steps.

Sample	F [μT]	σF [μT]	R^2	N	I_c [°]	ϵ_{alt} [%]
CCO2-1	40.9	0.4	0.78	4	75.0	25.6
CCO2-2	25.1	0.3	0.83	4	82.0	32.9
CCO2-4	39.3	0.2	0.96	3	84.5	30.2
$\bar{F}$	35.1	8.7				
$\bar{F}_{R^2}$	35.2	8.7				

Table 4.2: Results of the Dekkers-Böhnel experiments for site CCO. Shown are sample name, paleointensity F with standard deviation σF, correlation coefficient R^2, the number of primary heating steps, the inclination I in core coordinates, and the alteration error ϵ_{alt} after Fabian and Leonhardt (2010).

Also with the Dekkers-Böhnel method it was not possible to derive a reliable paleointensity value for every sample. Even though paleointensity values using the multispecimen method could be determined for the site SAB we query these results, as site SAB is studded with minerals with shrinkage cracks. Thus again, reliable values could be determined for the site CCO (see Tab. 4.2).

4.1.4 Discussion

The remanence directions of the sister samples used for the Dekkers-Böhnel method can be adopted for the calculation of paleodirections. We compare the mean direction of the site CCO (geographic coordinates: $D_g = 18°$, $I_g = -17.3°$ and k= 29.8; stratigraphic coordinates: $D_s = 23°$, $I_s = -24.1°$ and k = 29.7) to nearby sites from the Piñon Block (Luzieux *et al.*, 2006; Roperch *et al.*, 1987) (see Table 4.3). Site 03LL23 (Luzieux *et al.*, 2006) is the same as our site CCO. The paleodirections of these two sites are comparable as expected (the site 03LL23 is the one red circle within the blue α_{95} cone of confidence of our site in Fig. 4.6).

The lower inclination of our site compared to 03LL23 could be attributed to different bedding attitudes. Luzieux *et al.* (2006) did not measure dip and dip direction at the site itself but used the attitude of nearby sites to bedding correct the in situ directions. But also the geographic coordinates differ, thus another possibility has to be taken into account. An explanation attempt for the steeper inclinations can be found in the model of the Gorgona Plateau, which should have collided with the South American western margin in the Eocene (Kerr and Tarney, 2005). While the Caribbean Plateau CCOP might have formed the Pallatanga Formation, another oceanic plateau, the Gorgona Plateau was argued to have formed the Piñon Formation. As both formations yield the same radiometric ages, these plateaus erupted contemporary at about 90 Ma within the Farallon plate. The Caribbean plateau, which formed above the Galapagos hotspot collided with the western margin of South America about 10 Myr later, the Gorgona plateau accreted to the Ecuadorian coast at about 45Ma. Taking the direction and speed of the Farallon plate in the Late Cretaceous (NNE at 5-10 cm/yr) into account, the Gorgona plateau might have formed at the Sala y Gomez hotspot, also called Easter hotspot (26 - 30°). However, an acquisition of a magnetic remanence at a paleolatitude of 26 - 30° would result in an inclination of 44 - 49°, which is substantially steeper than our remanences from site CCO. Thus, we cannot confirm neither descent theory of the Piñon Formation with just one site.

As only one site is by far too less to determine paleosecular variation, we draw upon the previous paleomagnetic works in Ecuador to calculate the paleosecular variation. The classical S value of the virtual geomagnetic poles (VGPs) and also the simple k on directions were determined from the 13 sites of the Piñon Formation (Luzieux *et al.*, 2006). The concentration of the sites around the mean inclination I_m = -2.2° and declination D_m = 50.5° is described with a k = 32.7. The Piñon block moved from the eruption site above the Galapagos Hotspot to the Ecuadorian coast, thus for the calculation of the VGPs assumptions about the

Author	Sites	Attitude	N	D_g	I_g	k_g	D_s	I_s	k_s	α_{95}
This work	CCO	320/14	5	18.8	-17.3	29.8	23.4	-24.1	29.7	14.3
Luzieux *et al.* (2006)	03LL23	210/20*	14	38.2	-33.0		37.3	-18.2	183	2.8
Luzieux *et al.* (2006)	Piñon Fm	200/25	13	53.0	-15.0	17.5	50.5	-2.2	32.7	6.8
Roperch *et al.* (1987)	AN33-36	150/30	4	62.5	-5.9	54.3	60.1	-18.0	23.1	

Table 4.3: Paleodirections of site CCO compared to the same site in previous publications (Roperch *et al.*, 1987; Luzieux *et al.*, 2006) and to mean directions of Piñon Formation. Shown are the Authors of the studies, the site names, the bedding dip direction and dip (asterisk denotes that bedding attitude was determined from nearby site), the number of samples N measured from the site or the number of sites, respectively, declination D, inclination I and concentration parameter k in geographic and stratigraphic coordinates.

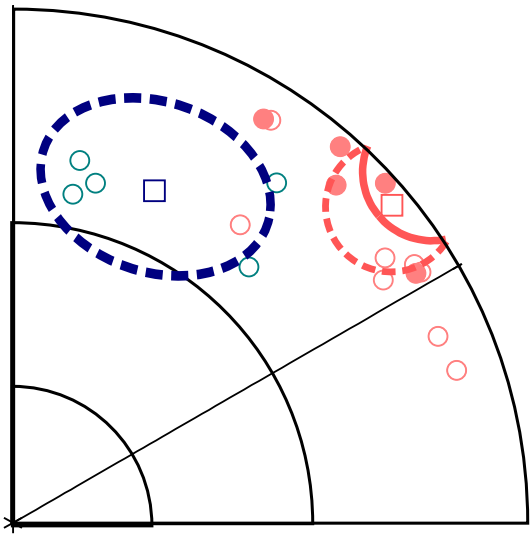

Figure 4.6: Stereographic projection of paleodirections from Ecuador. Filled circles denotes a positive inclination, empty circles a negative inclination. In the same way, filled squared and solid lined ellipse – Fisher mean direction and its corresponding α_{95} confidence cone – are on the upper hemisphere, empty square and dashed lined ellipse on the lower hemisphere. Our results from 5 different samples of site CCO are shown in blue, while previous paleomagnetic site means from the Piñon block (Luzieux *et al.*, 2006) are shown in red.

true site latitude (paleolatitude λ_P = -1.1° determined from mean inclination) and longitude have to be made. Also, the declinations can be rotated by D_m to move the VGPs to the geographic pole, but this will have no effect of the S value. The S value determined from the VGPs is $12.9^{17.7}_{10.2}$. This S value might be a bit overestimated as block rotations, which smeared the declinations, cannot be ruled out.

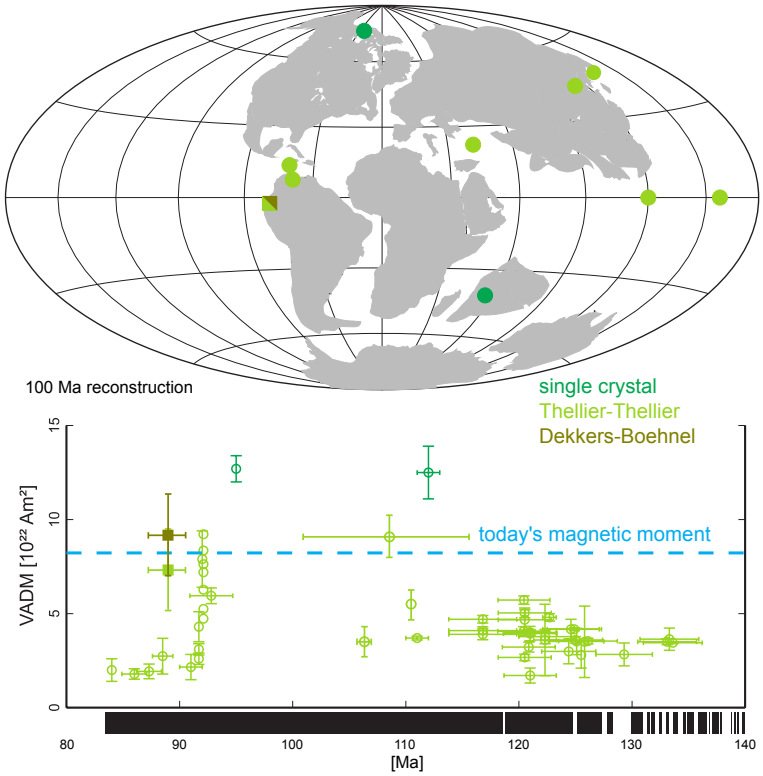

Figure 4.7: Virtual axial dipole moments (VADMs) during the Cretaceous Normal Superchron. Shown are the sites on a 100Ma paleogeographic reconstruction. Our study is denoted with solid squares, previous studies with circles (Zhu *et al.*, 2004; Tanaka and Kono, 2002; Zhu *et al.*, 2001, 2003; Zhao *et al.*, 2004; Tarduno *et al.*, 2002, 2001; Pick and Tauxe, 1993; Juarez *et al.*, 1998; Tauxe and Staudigel, 2004; Granot *et al.*, 2007; Shi *et al.*, 2005; Hill *et al.*, 2008; Tsunakawa *et al.*, 2009). The applied technique for paleointensity determination is codified in the color of the symbols: dark green for Thellier-Thellier determinations on single crystals, light green for classical Thellier-Thellier on bulk rock and olive-green for Dekkers-Böhnel methods. Below the VADMs are plotted against the age. Again, our weighted results are shown as color-coded squares at 88.8 Ma.

Determining a paleointensity value from Ecuador of the Cretaceous Normal Superchron age was disillusioning. However, even though most of the sites were too oxidized for paleointensity measurements the site CCO gave trustworthy results. With the Thellier-Thellier technique a mean intensity of 26.2 $\pm$ 8.1 μT was determined, the Dekkers-Böhnel method resulted in a mean paleointensity of 35.1

$\pm$ 8.7 μT. These two results are in agreement as the error bars are overlapping. When using the weighted mean paleointensities (28.2 $\pm$ 8.1 μT and 35.2 $\pm$ 8.7 μT), the agreement improves and the means are within the error bars of each other. The virtual dipole moments (VDMs) calculated from those two paleointensities are 6.8 $\pm$ 2.0 $\cdot$ 10^{22}Am^2 (or 68 $\pm$ 20 ZAm^2 using the metric prefix system) from the Thellier-Thellier result and 8.5 $\pm$ 2.1 $\cdot$ 10^{22}Am^2 from the Dekkers-Böhnel result. Using the mean inclination from the Piñon block (λ_P = -1.3°) and the Thellier-Thellier results the virtual axial dipole moment (VADM) of the Earth was 7.3 $\pm$ 2.1 $\cdot$ 10^{22}Am^2 at the end of the Cretaceous Normal Superchron. Using the Dekkers-Böhnel results the VADM is found to a higher 9.1 $\pm$ 2.5 $\cdot$ 10^{22}Am^2. If it is supposed that the Piñon Formation is a part of the Gorgona plateau, this VADM has no meaning, as the exact position of the Gorgona Plateau is not known. For this scenary only the calcuated VDM has a meaning. As the VDMs and VADMs do not differ substantially in our case, only the VADMs are used for further comparison.

Our VADM results will be compared with other CNS paleointensities from all over the globe (Fig. 4.7). From previous studies (e.g. Zhu *et al.*, 2004; Tanaka and Kono, 2002; Zhu *et al.*, 2001, 2003; Zhao *et al.*, 2004; Tarduno *et al.*, 2002, 2001; Pick and Tauxe, 1993; Juarez *et al.*, 1998; Tauxe and Staudigel, 2004; Granot *et al.*, 2007; Shi *et al.*, 2005; Hill *et al.*, 2008; Tsunakawa *et al.*, 2009) two distinct values of the virtual axial dipole moment were prominent: a high value, only found in studies using single crystals to determine the paleointensity (Tarduno *et al.*, 2002, 2001) and a low value (about half of today's moment) from the other studies. Only a study from the Troodos ophiolite (Granot *et al.*, 2007) showed higher values. The Ecuadorian values agree quite well with these results from the Troodos ophilite, which is only slightly older with an age of 92.1 Ma. Both studies show a VADM similar to today's magnetic moment of the Earth.

4.1.5 Conclusion

Of course, one successful site is far too less to determine the geodynamo's 'energy state' during the CNS on Ecuadorian volcanics. But as the preliminary paleointensities from this site determined with two different methods agree quite well with each other we are confident about our results. Based on our results, the field intensity towards the end of the superchron seems to be quite similar to today's magnetic moment. Also the paleosecular variation of coastal sites in Ecuador is comparable to the S value of the last 5 Myr. This agrees with our study in Northern Peru (Linder and Gilder, 2011), which also suggests a indistinguishable CNS

regime from that of the last 5 Myr. All together, it can be concluded that the geodynamo was in no substantially different 'energy state' during the Cretaceous Normal Superchron compared to reversing times.

Acknowledgments

We want to thank Cristian Fernando Vallejo Cruz, who accompanied us in the first few days of field work in the North-western Cordillera of Ecuador, and Professor Stalin Benitez and Katthy Lopez, who showed us numerous sites in the area of Guayaquil. Diego Gordon and his group from the DINAGE in Quito is thanked for help to find geological maps of the sites. Funding was provided by IDK 31 THESIS of the Elite Network of Bavaria (ENB) and grants from the Deutsche Forschungsgesellschaft (DFG-GI712/2-1 and DFG-GI712/2-2).

4.2 Outlook

Clearly, a proper alignment of subsamples is the most crucial aspect for the Dekkers-Böhnel paleointensity method. For the simple classical measurement an improper alignment could be corrected for if only the z-components of the measurements are considered. This is of course a compromise, as only if the laboratory pTRM is exactly in the direction of the remanence MD effects are unlikely to disturb the paleointensity measurement. But especially for the checks, this problem seems to be not solvable as pTRM imprinted in one check step cannot be totally removed in the following check step. This overestimates the tail imprinted to the samples. We might reconsider our sample holder for subcores and try to improve the alignment in our cryogenic magnetometer. Then the Dekkers-Böhnel method can be redone to see if better results are possible. Also, more Thellier-Thellier paleointensity measurements on site CCO can improve the statistics and check for reproducibility.

Additionally, more paleodirections will be measured to get reliable site mean directions. Paleosecular variation from these sites can then be calculated and compared to our paleosecular variation on nearby sediments from Northern Peru.

5 Conclusion

The scope of this dissertation was to infer if there was a special geodynamo regime triggering the Cretaceous Normal Superchron. Therefore, studies on paleosecular variation and paleointensity were carried out, both supposed to be a window into past geodynamo regimes.

As the S value increases with latitude λ, we searched for a suitable sites near the geomagnetic equator. A S value determined from a near-equatorial site represents the minimum scatter of virtual geomagnetic poles (VGPs) for any specific time. Thus, this S can directly be compared with other times without the knowledge of the slope of S(λ).

Paleogeographic reconstructions place Northern Peru and Ecuador near the geomagnetic equator during the Cretaceous Normal Superchron. For paleosecular variation we sampled a 1400 m long section of marine carbonates in Northern Peru. We chose this section specifically because its paleontology was well described, allowing us to correlate it both in relative and absolute time scales, and because the outcrop conditions allow for fairly continuous sampling.

We examined possible extraneous contributions to S. For example, whether instantaneous or averaged bedding corrections are applied modify S by 20% in this study. Modeling how sedimentary and volcanic rocks record the Earth's magnetic field revealed that S values from volcanic rocks are more dispersed than from sedimentary rocks, whereas sedimentary rocks will systematically underestimate

S. Because S values are strongly influenced by outliers, cut-off procedures have been advocated in several studies. But unless these outliers are proven not to be of geomagnetic origin, we argue that there is no reason to disregard them, even if the time represented by the outliers is much shorter than the total duration of the whole section. Opposed to standard deviations, quantiles are a statistically more rigorous way to treat outliers than simple cut-off colatitudes.

In our study S is quite variable during the Cretaceous normal superchron. From 108.7 to 100 Ma S values are fairly constant at ca. 9 and more variable, yet higher (ca. 21) from 96 to 87 Ma. An average S with an applied Vandamme cut-off, shows no marked dissimilarity with predicted S values from the compilation of Biggin *et al.* (2008b), but slightly higher than that of McFadden *et al.* (1991) during the Cretaceous Normal Superchron. On the other hand, the average S value from Pongo de Rentema is indistinguishable from that expected for equatorial S values for the last 5 Ma (McFadden *et al.*, 1991; Johnson *et al.*, 2008), which is in turn similar to an equatorial S value measured in sediments deposited during the Permian-Carboniferous Reversed Superchron (Haldan *et al.*, 2007). In conclusion, given the sum of all uncertainties contributing to an S value, we find it questionable whether S is a suitable parameter for characterizing paleosecular variation, and hence, unworthy to constrain geodynamo models. Otherwise, we find no statistical distinction between Cretaceous and recent fields.

Since the latitude dependency of the S value was first described (Cox, 1970) the origin of this latitude dependency remained enigmatic. Differences in the slope of the S value were attributed to varying contribution of the decoupled symmetric and asymmetric geodynamo families (e.g. McFadden *et al.*, 1988, 1991). With a simple exercise – calculating the S value from an artificial circular distribution of directions – we could show that this latitude dependency stems from the conversion of directions to poles. This finding was verified using Fisher distributed directions and observatory records. Usually, paleomagnetists are interested more in the mean VGP than in the dispersion of the VGPs around their mean. The conversion does not affect the calculation of a mean VGP. However, the dispersion of the VGPs is distorted by the the non-linear conversion. Problems surrounding the directions-to-poles conversion have long been recognized (Cox, 1970; Brock, 1971; Kono, 1997; Khokhlov *et al.*, 2001; Tauxe and Kent, 2004), but they were never associated with the latitude dependency of the S value. Our exercise implies that the latitude dependency of S owes its origin to a geometrical aberration from the mathematical conversion of directions to virtual geomagnetic poles and is not related to geomagnetic phenomena. This finding hearkens back the oft-posed question whether poles or directions are more Fisherian distributed—a fact

that is traditionally (Cox, 1962), yet arbitrarily (Kono, 1997), attributed to poles. Moreover, the conversion from directions to poles has the assumption of a dipolar field geometry built into it–defining secular variation directly from directional populations eliminates this assumption.

That latitude dependence in virtual geomagnetic pole scatter curves owes its origin to a mathematical artifact dispenses the notion that symmetric and asymmetric families are necessarily decoupled (e.g. McFadden *et al.*, 1988, 1991). Also, the elongation/inclination (E/I) method that corrects paleomagnetic data sets for inclination shallowing (Tauxe and Kent, 2004) converts poles back to directions and therewith distorts the geometric distribution of directions in the opposite way as we did.

Which parameter should now be used to quantify secular variation from directions? Of the various options, the concentration coefficient k is likely the best choice, and the uncertainty on k(N) was already worked out (Cox, 1969).

From our study in Northern Peru we found no substantially different paleosecular variation during the Cretaceous Normal Superchron compared to the reversing last 5 Ma. Paleointensities should complement the study on the state of the geodynamo during the Cretaceous Normal Superchron. We chose nearby volcanics from Northern Peru and Ecuador to reduce longitudinal effects. Oxidation of remanence carriers was a problem with the Ecuadorian samples. Only one site was classified suitable to give reliable results. Two methods of paleointensity determination were applied to the rocks of this site. Of course, one successful site is far too less to determine the geodynamo regimes during the CNS on Ecuadorian volcanics. But as the result is confirmed by two different methods and agrees quite well with other studies, we are confident. However, the field intensity towards the end of the superchron seems to be not so different from today's global magnetic moment. Also the paleosecular variation of coastal sites in Ecuador is comparable to the S value of the last 5 Myr. This agrees with our study on the sediments from Northern Peru, which also suggests a indistinguishable CNS regime from that of the last 5 Myr. All together, it can be concluded that the geodynamo was in no substantially different 'energy state' during the Cretaceous Normal Superchron compared to reversing times.

Why do superchrons exist? One possible explanation is that paleomagnetism is not able to resolve different energy states of the geodynamo, neither with paleosecular variation nor with paleointensities. This was suggested by some dynamo simulations in which the heat flux across the core-mantle boundary was kept the same, but the resulting paleosecular variation, paleointensity and frequency of reversals differed a lot (Glatzmaier *et al.*, 1999). Another possible explanation is

that a superchron is an intrinsic feature of the distribution of magnetic polarity chron lengths (e.g. Hulot and Gallet, 2003; Shcherbakov and Fabian, 2012). Thus, no changes of the convection in the outer core are needed to trigger a superchron.

A

Table of results Pongo de Rentema

Table A.1: Results from the paleomagnetic study of the Pongo de Rentema section. Sample ID, age, stratigraphic heigth, dip direction (dd) and dip (d), declination (Dg) and inclination (Ig) in geographic coordinates, magnetization of the sample and volumetric susceptibility of the measured samples.

sites PDR	age [Ma]	stratigraphic height[m]	dd [°]	d [°]	D_g [°]	I_g [°]	M [mA/m]	susceptibility [$\cdot e^{-6}$]
1	109,659	0			329,5	-27,1	0,759	132
2	109,6458	0,6	222	65	325,3	-28	0,929	101
3	109,6249	1,55			339,3	-22,6	1,25	116
4	109,5996	2,7			325,7	-27,1	1,15	129
5	109,5709	4			331,2	-31,8	1,41	102
6	109,5313	5,8	246	55	333,8	-20	0,553	85
7	109,4211	10,8			330,6	-21,9	1,04	89
8	109,4013	11,7			343,3	-18,2	0,565	100
9	109,3771	12,8			335,5	-23,8	0,621	75
10	109,3518	13,95			332,6	-23,9	0,841	57
11	109,3297	14,95	250	54	328,8	-23	0,749	53

Tab. A.1 continued

sites PDR	age [Ma]	stratigraphic height[m]	dd [°]	d [°]	D_g [°]	I_g [°]	M [mA/m]	susceptibility [$\cdot e^{-6}$]
12	109,3066	16			337,7	-21,6	1,19	137
13	109,2868	16,9	245	54	335,6	-17,4	0,891	93
14	109,2615	18,05			327,4	-24,4	0,977	45
15	109,2394	19,05			325,3	-22,2	0,769	75
16	109,2196	19,95			336,9	-16,4	0,3	48
17	109,1965	21			327,1	-22,7	2,2	124
18	109,1744	22			327,5	-26,4	1,12	45
19	109,1524	23			331,7	-25,6	1,17	80
20	109,1293	24,05			334,3	-18,6	0,861	72
21	109,1139	24,75	232	49	333,8	-21,8	0,789	75
22	109,0907	25,8			337,9	-15,2	0,334	44
23	109,0764	26,45			332	-23,5	0,46	45
24	109,0214	28,95			342,4	-15,3	1,07	71
25	108,9619	31,65	222	54	337,4	-14,2	0,198	63
26	108,9377	32,75			349,9	-2,4	0,506	92
27	108,9134	33,85			329,7	-20,5	0,151	39
28	108,8837	35,2	225	57	336,6	-20,7	0,253	38
29	108,8551	36,5			330,9	-25	0,415	53
30	108,8242	37,9			352	-13,7	3,06	124
31	108,8088	38,6			324,2	-24,8	0,642	89
33	108,7438	41,55			345,5	-12,4	0,693	95
34	108,7064	43,25			357	-1,8	0,507	143
35	108,6029	47,95			1,5	-23,6	0,348	134
36	108,5445	50,6			343,7	-20,6	0,265	111
37	108,5148	51,95			349,1	-21,1	0,44	111
38	108,4619	54,35			337,2	-20,8	0,474	111
39	108,4421	55,25			338,6	-12,4	0,618	148
40	108,4211	56,2			334,5	-32,5	0,612	91
41	108,3991	57,2	234	54	338,3	-19,9	0,756	57
42	108,3837	57,9			333,7	-23,3	0,749	69
43	108,3705	58,5			336,7	-20,9	1,72	100
44	108,3551	59,2	235	56	327,7	-21,8	1,41	86
45	108,3319	60,25			339,9	-19,6	1,46	106
46	108,3055	61,45			327,2	-23,8	1,37	62
47	108,2879	62,25			323,1	-24,9	0,801	51

Tab. A.1 continued

sites PDR	age [Ma]	stratigraphic height[m]	dd [°]	d [°]	D_g [°]	I_g [°]	M [mA/m]	susceptibility [$\cdot e^{-6}$]
48	108,2703	63,05			336,8	-13,6	0,654	47
49	108,2482	64,05			339,5	-19,8	0,76	67
50	108,224	65,15			327,8	-21,2	0,984	123
51	108,2042	66,05			324	-24,5	1,74	109
52	108,1833	67			326,9	-20,5	1,48	129
53	108,1524	68,4			336,8	-37,8	0,988	98
54	108,1348	69,2			318,6	-21,9	0,831	232
55	108,1128	70,2			316,6	-13,5	0,373	127
56	108,0963	70,95			327	-15	1,38	100
57	108,0874	71,35			331	-24,3	1,1	108
58	108,0632	72,45	219	60	330,9	-22,3	0,821	124
59	108,0434	73,35			336,1	-20,7	2,39	127
60	108,0214	74,35			342,6	-21,8	0,245	78
61	108,0037	75,15			334,9	-17,6	0,553	62
62	107,9883	75,85	205	50	337,4	-19,1	0,211	99
63	107,9751	76,45			335	-14,4	0,458	66
64	107,963	77			334	-22,1	2,91	183
65	107,9498	77,6			332,3	-22,4	0,693	42
66	107,9256	78,7			324,7	-19,5	0,716	97
67	107,9002	79,85	226	60	319	-15,8	0,912	117
68	107,8804	80,75			330,1	-19,1	1,11	120
69	107,8639	81,5			340,1	-22,3	0,469	101
70	107,8419	82,5			333,6	-21,8	0,442	126
71	107,8286	83,1			334,9	-14,6	0,795	117
72	107,8154	83,7			336,3	-24,9	0,692	124
73	107,7868	85			5,7	-2	0,639	95
74	107,7747	85,55			336,3	-17,6	1,12	164
75	107,7537	86,5	235	61	313,6	-56,4	0,455	126
76	107,7449	86,9			352,8	-11,9	0,719	113
77	107,6985	89,01			332,9	-7,9	1,17	104
78	107,6982	89,02			2	7,8	0,651	126
80	107,6934	89,24			348,3	-15	0,588	100
82	107,6877	89,5			342,4	-20,1	0,735	103
83	107,6839	89,67			348,5	3,9	0,891	76
85	107,6784	89,92			359,2	-15,2	0,883	108

Tab. A.1 continued

sites PDR	age [Ma]	stratigraphic height[m]	dd [°]	d [°]	D_g [°]	I_g [°]	M [mA/m]	susceptibility [$\cdot e^{-6}$]
86	107,6749	90,08			1,8	3,5	0,518	66
87	107,6742	90,11			350,1	-6,6	0,964	78
88	107,6696	90,32			359,4	-13	0,443	73
89	107,6661	90,48			344,2	-4,8	0,813	107
90	107,6645	90,55	230	59	341,8	-21	0,225	122
91	107,6634	90,6			342,9	-4,6	0,588	71
92	107,6606	90,73			338,7	-6,3	0,474	66
93	107,657	90,89			346,2	-6,1	0,617	57
94	107,6531	91,07			341,3	-5,6	0,76	121
97	107,6452	91,43			340	-11,1	0,376	97
98	107,6447	91,45			339,2	-36,3	0,998	131
99	107,6414	91,6			338,9	-9,9	0,328	100
100	107,6383	91,74			336	-4,8	0,572	100
101	107,6355	91,87			341	-4,3	0,439	93
102	107,6333	91,97			345,5	-13	1,45	147
104	107,6289	92,17			328,5	-13	0,187	88
105	107,6282	92,2			340,9	-12,6	0,641	125
106	107,6278	92,22			333,5	-3,6	0,227	96
107	107,6262	92,29			346,6	-7,2	0,535	117
108	107,6247	92,36			338,6	-10,1	0,422	105
109	107,6229	92,44			341,1	-2,3	0,408	100
110	107,6198	92,58			344,1	-11,8	0,401	100
112	107,6159	92,76			336,8	-14,7	0,468	86
113	107,6143	92,83			341,7	-13,9	0,494	134
115	107,6106	93	230	59	338,2	-20,7	0,706	142
116	107,6086	93,09			335,5	-14,5	0,353	64
117	107,6055	93,23			341,4	-13,1	0,495	103
118	107,6029	93,35			338,9	3,4	0,642	86
119	107,6011	93,43			336,3	-14,1	0,384	78
120	107,6	93,48			326,2	-9,8	0,382	100
121	107,5991	93,52			341,6	-11,6	0,321	115
122	107,5978	93,58			328,1	-11,7	0,499	118
124	107,5956	93,68			335,4	-24,1	0,598	78
125	107,5941	93,75			327,3	-28,9	0,339	89
126	107,5923	93,83			336,1	-18,9	0,245	84

Tab. A.1 continued

sites PDR	age [Ma]	stratigraphic height[m]	dd [°]	d [°]	D_g [°]	I_g [°]	M [mA/m]	susceptibility [$\cdot e^{-6}$]
127	107,5903	93,92			328,7	-18,3	0,316	70
130	107,5863	94,1			332,7	-24,1	0,286	109
131	107,5848	94,17			333,3	-18,5	0,38	116
132	107,5828	94,26			341,8	-10,5	0,393	106
133	107,5804	94,37			333,7	-13,5	0,523	90
134	107,5793	94,42			322,6	-18,8	0,19	77
135	107,5778	94,49			344	-26	0,555	75
136	107,5764	94,55			337,8	-13,9	0,228	112
137	107,574	94,66			327,7	-16,2	0,288	41
138	107,5698	94,85			338,3	-6,1	0,532	97
139	107,567	94,98			335,6	-14,7	0,501	106
140	107,5643	95,1			341,1	-14	1,12	120
141	107,5637	95,13			319,4	-17,4	0,566	105
142	107,5626	95,18			345,8	-12,3	0,535	74
143	107,5615	95,23			333,4	-16	0,527	78
144	107,5586	95,36			341,3	-4,3	0,579	109
145	107,5559	95,48			327,4	-2,9	0,48	86
146	107,5546	95,54			341,3	5,2	0,633	97
147	107,5529	95,62			342,6	-9,8	0,396	102
148	107,5507	95,72			339,5	-16,9	0,241	80
149	107,5485	95,82			347,5	-20,8	0,175	71
150	107,5463	95,92			341,6	-17,2	0,118	86
153	107,5401	96,2			330,4	3,6	0,745	104
155	107,5324	96,55			318,1	-4,9	0,286	75
157	107,5264	96,82			330,3	-15,5	0,617	40
158	107,5249	96,89			334,7	-15,2	0,441	62
159	107,5216	97,04			340,2	-14	0,284	54
160	107,5093	97,6			328,7	-22	0,471	97
161	107,496	98,2			327,5	-22,7	0,646	88
162	107,4674	99,5			329,7	-22,7	0,779	122
163	107,4377	100,85	229	53	339,1	-11,9	0,642	92
164	107,4024	102,45			338,9	-19,1	0,525	99
165	107,365	104,15			348,7	-13,8	0,774	106
166	107,3319	105,65	244	55	348,7	-22,3	0,248	52
167	107,3033	106,95			342,9	-15,2	0,724	72

Tab. A.1 continued

sites PDR	age [Ma]	stratigraphic height[m]	dd [°]	d [°]	D_g [°]	I_g [°]	M [mA/m]	susceptibility [$\cdot e^{-6}$]
168	107,2438	109,65			348,4	-17,5	1,04	154
169	107,2185	110,8			340,4	-10	2,35	173
170	107,2009	111,6			336,5	-17	1,35	147
172	107,1844	112,35			337,8	-21,7	0,287	77
173	107,1623	113,35			343,4	-22,8	1,06	138
174	107,1282	114,9			338,5	-21,2	1,73	151
175	107,1139	115,55			347,3	-19,6	0,533	83
176	107,0996	116,2			343	-21,2	0,998	0
177	107,0819	117			337,5	-17,4	1,08	97
178	107,0731	117,4			340,6	-6,7	0,837	107
179	107,0588	118,05			346,6	-9,7	1,24	121
180	107,0467	118,6	227	57	343,3	-16,7	2,33	168
181	107,0324	119,25			305,8	3	0,69	127
182	107,0159	120			342	-18,5	1,87	143
183	107,007	120,4			337,6	-6,6	1,71	133
184	106,9938	121			337,8	-20,2	1,69	184
185	106,9773	121,75			339	-22,8	1,34	134
187	106,9399	123,45	256	55	347,7	-15,7	0,728	84
189	106,9046	125,05	249	55	355,5	-30,4	2,79	0
190	106,9041	125,075			337,6	-16,4	0,595	58
191	106,903	125,125			335,2	-15,5	0,972	64
193	106,9012	125,205			353,3	-6,4	0,854	76
194	106,9004	125,24			1,9	-5,3	0,471	65
195	106,8994	125,285			334,2	-18,7	1,01	73
196	106,8983	125,335			345,6	-5,3	0,95	70
197	106,8975	125,375			319,4	-18,2	0,543	85
198	106,8966	125,415			336,7	-13,3	1,05	0
199	106,8958	125,45			336,4	-15,6	0,805	97
200	106,8946	125,505			338,8	-22,9	1,12	77
201	106,8937	125,545			350,3	-24,8	0,334	73
202	106,8928	125,585			336,8	-16,7	0,623	75
203	106,8922	125,615			333,1	-15,7	1,12	82
204	106,8914	125,65			324,9	-15	0,533	57
205	106,8906	125,685			345,2	-12,9	0,591	59
206	106,8899	125,72			346	-18,9	0,369	54

Tab. A.1 continued

sites PDR	age [Ma]	stratigraphic height[m]	dd [°]	d [°]	D_g [°]	I_g [°]	M [mA/m]	susceptibility [$\cdot e^{-6}$]
207	106,8887	125,775			334,7	-26,2	0,417	70
208	106,888	125,805			346,8	-4,7	0,865	75
209	106,8872	125,84			313,7	-12,9	1,04	95
210	106,8863	125,88			343,8	-10,3	0,756	77
211	106,8855	125,92			323,4	2,5	0,945	96
212	106,885	125,94			337,1	-20	0,463	58
213	106,8848	125,95			342,1	-27,3	0,573	75
214	106,8826	126,05			335,6	-19,6	0,548	69
215	106,8782	126,25			332,4	-21,4	0,358	67
216	106,876	126,35			346,4	-8,3	0,328	54
217	106,8756	126,37			345,1	-20,1	0,439	74
218	106,8727	126,5			334,2	-22,8	0,388	54
219	106,8705	126,6			354,1	-15,8	0,659	93
220	106,8694	126,65			332,8	-23,8	0,292	35
221	106,8683	126,7			336,9	-18,5	0,549	39
222	106,8672	126,75			327,7	4,9	0,247	46
223	106,8661	126,8			335,5	-21,2	0,317	50
224	106,865	126,85			336,4	-22,1	0,581	44
225	106,8617	127			332,7	-20,8	0,274	51
226	106,8612	127,02			338,3	-22,9	0,689	60
227	106,8469	127,67			338,1	-20	1,32	104
228	106,8337	128,27	254	49	338,8	-22,3	0,844	72
229	106,8194	128,92			345,2	-17,6	0,686	71
232	106,7742	130,97			342	-10,4	0,617	91
233	106,7577	131,72			357,1	-18,8	0,827	87
234	106,739	132,57			340,8	-20,1	0,602	92
235	106,7225	133,32			344	-22,7	0,461	79
236	106,7037	134,17			354,9	-9,4	1	127
238	106,6762	135,42			351,1	-23,3	0,505	0
240	106,6485	136,68			344,4	-25,5	0,593	97
241	106,6286	137,58			341,8	-20,1	0,703	71
242	106,6143	138,23			350	-25,8	0,527	73
243	106,5956	139,08	256	52	340,5	-11,4	0,717	97
245	106,5427	141,48			344,9	-32,8	0,57	74
246	106,5185	142,58			340,2	-16	0,489	76

Tab. A.1 continued

sites PDR	age [Ma]	stratigraphic height[m]	dd [°]	d [°]	D_g [°]	I_g [°]	M [mA/m]	susceptibility [$\cdot e^{-6}$]
248	106,4756	144,53			341,8	-16,1	0,42	32
249	106,4568	145,38			336,9	-23,2	0,886	65
250	106,4392	146,18			337,5	-12,7	0,747	47
251	106,4194	147,08			339,2	-20	0,402	43
252	106,4007	147,93			334	-23,3	0,565	30
253	106,3885	148,48			337,5	-10,6	1,01	51
254	106,3698	149,33			339,7	-13	0,371	55
255	106,3544	150,03			344,6	-13,2	0,787	70
256	106,3423	150,58			336,2	-3,4	0,438	51
257	106,3159	151,78			312,9	-10,1	0,326	52
258	106,296	152,68			331,9	-15,9	0,382	48
260	106,2531	154,63			325,5	-18,2	0,183	33
261	106,2311	155,63			330,2	-19,3	0,383	39
262	106,2079	156,68			332,1	-17,7	0,584	58
263	106,1804	157,93	244	53	337,7	-15,9	0,354	40
264	106,1628	158,73			229,3	-18,9	0,715	82
265	106,1463	159,48			340,2	-4,8	0,766	81
266	106,1088	161,18			342,9	-20,3	0,716	60
267	106,0923	161,93			345,1	-23,2	0,93	62
268	106,0637	163,23	254	54	343,1	-7,6	0,862	68
269	106,0427	164,18			354,4	-8,7	2,59	123
272	105,8874	171,23			348,3	-17,4	0,83	54
273	105,8709	171,98			343,3	-21,5	0,618	72
274	105,85	172,93	227	57	329,9	-12,3	0,499	32
275	105,8236	174,13			334,7	-22,1	0,428	53
276	105,8037	175,03			348,8	-14,6	0,639	43
277	105,7509	177,43			335,8	-24,3	0,719	118
278	105,7355	178,13			340,2	-10,3	0,555	108
279	105,6947	179,98	239	56	353,4	-13,4	0,35	84
280	105,6804	180,63			336,8	-19,3	0,521	34
281	105,6639	181,38			338,5	-14,7	0,562	40
282	105,6452	182,23			340,7	-19,9	0,667	70
283	105,6286	182,98			331,9	-27,5	0,226	33
284	105,6088	183,88	225	58	339,7	-23,3	0,651	61
285	105,5934	184,58			335,2	-13,5	0,925	49

Tab. A.1 continued

sites PDR	age [Ma]	stratigraphic height[m]	dd [°]	d [°]	D_g [°]	I_g [°]	M [mA/m]	susceptibility [$\cdot e^{-6}$]
286	105,5504	186,53			351,4	-17,2	0,588	56
287	105,5108	188,33			337,5	-18,9	0,255	78
288	105,4778	189,83			349,1	-16,6	0,369	44
289	105,4447	191,33			349,2	-18,3	0,461	44
290	105,4282	192,08			346,1	-24,4	0,387	42
291	105,4139	192,73			349,9	-20	0,755	49
292	105,3952	193,58	231	56	342,6	-22,1	0,35	38
293	105,3621	195,08			341,7	-15,9	0,456	40
294	105,3423	195,98			336,6	-25,8	0,343	30
295	105,3093	197,48			335,4	-23,7	0,292	23
296	105,2949	198,13			335,1	-26	0,32	25
297	105,2806	198,78			349,2	-19,1	0,455	52
298	105,2608	199,68			344,1	-25,5	0,734	46
299	105,2322	200,98			341	-19,2	0,424	13
300	105,2284	201,15	254	45	339,4	-17,3	0,51	32
301	105,2152	201,75			339,3	-18,8	0,777	37
302	105,1987	202,5			341,3	-19	0,725	35
303	105,1744	203,6			345,9	-16,7	0,573	33
304	105,1568	204,4			335,7	-20,5	0,558	73
305	105,1436	205			348,3	-8,2	0,805	55
306	105,1282	205,7			334,5	-23,2	0,768	31
307	105,104	206,8			343,7	-22,7	0,617	51
308	104,8046	220,39			341,9	-13,9	2,82	67
309	104,6416	227,79			336,8	-19,4	0,571	39
311	103,9156	260,75	212	41	0,5	-27,8	0,274	115
312	103,9002	261,45	234	47	332,4	-9,3	0,159	102
313	103,8716	262,75			0,1	-18,8	0,444	116
314	103,8363	264,35	225	58	338,6	-26,6	0,276	53
315	103,8055	265,75			341,7	-11,4	0,177	56
316	103,7868	266,6	244	59	338,5	-14,8	0,341	82
317	103,7692	267,4			340,8	-12,9	0,0736	56
318	103,7548	268,05			350,4	-15,7	0,487	73
319	103,7416	268,65			349,4	-11,5	0,26	31
320	103,7273	269,3			356,7	-12,8	0,202	61
321	103,659	272,4	214	64	344,6	-14	0,912	140

Tab. A.1 continued

sites PDR	age [Ma]	stratigraphic height[m]	dd [°]	d [°]	D_g [°]	I_g [°]	M [mA/m]	susceptibility [$\cdot e^{-6}$]
322	103,5885	275,6			356,1	-13,7	0,313	89
323	103,4806	280,5	243	52	5,7	-20,7	0,324	112
325	103,4233	283,1			355,9	-16,5	0,255	123
326	103,3771	285,2			352,1	-12,9	0,264	0
327	103,3132	288,1			342,2	-20,8	0,375	129
328	103,3	288,7	243	54	340,1	-18,1	0,286	74
329	103,2813	289,55			324,2	-23,5	0,324	117
330	103,2694	290,09			331,6	-18,3	0,318	120
332	103,2672	290,19			1,3	8,6	0,449	94
333	103,2661	290,24			323,9	-20,4	0,414	98
334	103,265	290,29			343,7	-9,6	0,312	78
335	103,2648	290,3	243	66	325	-26,6	0,2	130
336	103,2645	290,31			332,2	-17,5	0,417	120
338	103,2207	292,3			329,7	-12,5	0,235	31
339	103,1976	293,35			329,7	-21,8	0,455	57
340	103,1756	294,35			323,5	-20,2	0,446	54
341	103,1601	295,05			323,8	-26,9	0,633	29
342	103,1381	296,05			333,6	-25,6	0,505	45
343	103,1073	297,45			322,1	-23,5	0,774	37
344	103,0742	298,95			337,2	-11,4	0,439	81
345	103,0478	300,15	253	52	327,4	-24,7	0,471	0
346	103,0159	301,6			324,6	-26,9	0,582	38
347	102,9674	303,8			326,3	-22,8	0,599	37
348	102,9432	304,9			325,6	-25,4	0,465	47
349	102,941	305			321,6	-21	0,699	61
350	102,9407	305,01			343,3	-23,4	0,462	56
351	102,9341	305,31			333,3	-20,8	0,283	35
352	102,9319	305,41			330,6	-18,9	0,269	31
353	102,9311	305,45			332,8	-22,1	0,277	24
354	102,93	305,5			331,4	-15,3	0,374	25
355	102,9189	306			335	-23,6	0,493	85
356	102,9079	306,5			336,8	-23,6	0,537	74
357	102,8947	307,1			340,7	-19,6	7,05	57
358	102,8396	309,6	256	53	337,3	-17,1	0,696	127
359	102,8044	311,2			325,4	-18,7	0,776	68

Tab. A.1 continued

sites PDR	age [Ma]	stratigraphic height[m]	dd [°]	d [°]	D_g [°]	I_g [°]	M [mA/m]	susceptibility [$\cdot e^{-6}$]
360	102,7758	312,5			332,5	-20,3	1,38	103
361	102,7537	313,5			324,5	-11,1	0,739	59
362	102,7251	314,8			333,7	-21,8	0,467	73
363	102,6833	316,7			325,5	-29	2,41	106
364	102,659	317,8	231	48	326	-20,6	2,61	82
365	102,6304	319,1			324,3	-10,4	1,48	77
366	102,5952	320,7			323,4	-25,7	0,99	78
368	102,5632	322,15			359,5	11,6	0,332	32
369	102,5445	323	238	52	331,5	-22,1	0,33	51
370	102,5247	323,9			340,5	-10,1	0,413	42
371	102,4982	325,1			326	-23,3	0,196	38
375	101,3537	377,06	204	67	323,8	-20,9	0,436	86
376	100,9022	397,56	236	53	4,8	-26,8	0,236	342
377	95,29207	652,26	234	63	351,4	0,5	0,283	40
378	95,2304	655,06	241	57	339,9	-10,7	0,171	64
379	95,20837	656,06			324,1	-19,4	0,124	48
380	95,17753	657,46			347,6	8,2	0,177	95
381	95,11586	660,26	243	55	352,4	-4,2	0,251	95
382	95,08282	661,76	244	55	346,7	-8,8	0,284	196
384	94,99802	665,61			1,6	-23,4	0,204	99
385	94,95837	667,41	240	59	357	-10,3	0,25	64
386	94,92093	669,11			322,9	-3,1	0,241	33
389	94,813	674,01	241	57	328	-27,3	0,133	46
390	94,80198	674,51			347,2	1,2	0,129	37
391	94,76344	676,26			357,4	-17,8	0,942	47
393	94,69405	679,41			336,7	-2,4	0,223	43
394	94,64339	681,71	239	61	7,7	-8,7	0,0582	24
395	94,61916	682,81			347	-27,4	0,0436	31
396	94,59467	684,21			336,2	-14,3	0,168	21
397	94,58498	686,41			355,5	12,2	0,196	37
398	94,57925	687,71			354	-15,6	0,0748	47
399	94,57441	688,81	232	62	354,7	-13,2	0,142	228
400	94,5537	693,51	232	59	355	-14,7	0,837	191
402	94,53256	698,31			340,3	-14,5	0,577	127
403	94,52198	700,71	243	62	330,9	-17,5	0,148	75

Tab. A.1 continued

sites PDR	age [Ma]	stratigraphic height[m]	dd [°]	d [°]	D_g [°]	I_g [°]	M [mA/m]	susceptibility [$\cdot e^{-6}$]
404	94,51824	701,56			341,5	0,9	0,331	63
405	94,51251	702,86			348,6	-7,4	0,893	50
407	94,50018	705,66			3,5	-5,6	0,16	58
409	94,47242	711,96			348,5	-13,3	0,176	112
410	94,4667	713,26			345,6	-28,1	0,312	173
411	94,46361	713,96	237	65	359	-27	0,0798	105
415	94,39295	730			335,9	-16,8	2,01	323
416	94,39273	730,05			337,3	-17,9	1	281
417	94,38379	732,08			63,9	10,3	0,28	279
419	94,38352	732,14			89,1	55,9	0,331	265
424	94,37828	733,33			131,1	20,6	0,193	62
426	94,37811	733,37			131,6	5,7	7,78	58
432	94,37753	733,5			341,6	-25	0,215	60
433	94,3774	733,53			7,4	-25,4	0,589	46
437	94,36859	735,53			348,3	-13,3	12,9	281
438	94,36846	735,56			349,9	-7,8	7,78	235
439	94,32692	744,99			333,6	-28,4	0,91	150
440	94,23907	764,93	237	59	350,5	-7,4	1,47	96
443	93,90132	841,6			338,3	-21	1,54	94
445	93,85097	853,03	249	69	347,6	-25,1	0,24	123
446	93,83599	856,43			332,4	-16,6	0,407	187
447	93,82145	859,73	247	70	354,7	-18	0,71	303
448	93,7959	865,53	244	64	322,8	-17,7	0,0568	0
449	93,78841	867,23			1,7	-11,7	0,649	330
450	93,7796	869,23	242	65	354	-15,9	2,67	136
451	93,70026	887,24	241	69	324,9	-19,9	0,838	224
452	93,69894	887,54	237	69	0,8	-14,5	0,692	217
453	93,68793	890,04			344,3	-11,1	0,102	111
454	93,6615	896,04	234	67	347	-9,7	1,37	166
455	93,63507	902,04			354,2	-13	0,0721	74
456	93,597	921,21			352,1	-15,3	0,151	42
457	93,56843	923,21			344	-12,6	0,0501	126
458	93,48271	929,21			344,9	3,4	0,0391	122
459	93,17843	950,51	250	61	351,4	-10,4	0,0367	63
461	91,708	1053,44			358,2	-3,5	0,0417	122

Tab. A.1 continued

sites PDR	age [Ma]	stratigraphic height[m]	dd [°]	d [°]	D_g [°]	I_g [°]	M [mA/m]	susceptibility [$\cdot e^{-6}$]
463	91,419	1073,67			12,3	-46,3	0,255	81
464	91,00686	1102,52			349,5	-0,2	0,0447	4
465	90,964	1105,52			0,9	-11,6	0,109	4
466	90,94257	1107,02	249	71	346,2	4,5	0,0625	5
467	90,92829	1108,02			335,7	-13,5	0,245	5
468	90,92114	1108,52			339,2	-17,4	0,64	20
469	90,91757	1108,77	240	56	341,9	-6,1	0,142	33
470	90,90757	1109,47			348	-6,5	0,155	42
471	90,89329	1110,47			6,3	-16,7	0,192	51
474	90,73257	1121,72			338,5	-5,4	0,139	66
477	90,67257	1125,92			331,3	-9,4	0,201	144
478	90,65114	1127,42	242	74	352,1	-27,7	0,384	70
479	90,62829	1129,02			323	-9,5	0,296	138
481	90,51757	1136,77			357,6	-4,9	0,104	55
485	90,19757	1159,17			323,8	-1,1	0,114	167
489	90,03114	1170,82			301,6	-23,7	0,0864	235
490	90,024	1171,32	230	51	321,6	-29	0,0895	122
491	89,89543	1180,32			346	-33	0,479	353
494	89,75543	1190,12			343,9	-16,4	0,542	270
495	89,74543	1190,82			314,5	-15,8	0,144	273
497	89,68829	1194,82			305,5	-14,7	0,2	300
498	89,67543	1195,72	235	66	298,7	32,5	0,606	404
499	89,664	1196,52			302,1	8,9	0,0968	326
500	89,65257	1197,32			334,6	-12,6	0,102	180
501	89,63543	1198,52			323,4	-3,6	0,163	67
503	89,14157	1233,09	230	60	327,3	13,5	0,0872	170
507	88,67443	1265,79			326,8	-5,2	0,386	185
508	88,47157	1279,99			333,3	5,4	0,0561	176
511	88,31586	1290,89	223	57	318,1	-10,5	0,0789	353
514	87,98014	1314,39			350,8	-7,6	0,0907	185
516	87,80871	1326,39			337,4	-12,2	0,155	208
519	87,70586	1333,59	243	59	317,5	17,8	0,0953	131
526	87,353	1358,29			327,7	13,5	0,093	226
534	87,033	1380,69			292,7	3,4	0,0918	273

B
Sites in Ecuador

Pedernales area

First paleomagnetic sampling in the northernmost block of the Piñon Terrane was done by Roperch *et al.* (1987) for the determination of rotations. We sampled 3 sites in the Pedernales block. Sites were found using geological maps San José de Chamanga (CT-NIL-E) and Jama (CT-MIII-B) from the DINAGE. The site PED is located east of Pedernales at the road to Santa Domingo de Los Colorados. The outcrop of the Piñon Formation is located directly at the street near the entrance to a quarry. Columnar basalt could be used to estimate the bedding attitude. Due to rockfall no drilling was possible in the upper part of the site.

Two more sites can be found following a road to the east from Jama. The site VEN is located shorty after the ford through the Rio Venado just before the entrance to the village Venado Abajo. The outcrop is right in the stream bed of the Rio Venado and consists of numerous pillows with glassy rims. From the shape of the pillows the bedding attitude could be estimated. 12 oriented cores were drilled. The site SRO is located at another branch of the road up the hill near the settlement San Roque. The outcrop is in a unnamed stream bed. Bedding attitude was not clearly visible, thus a handsample for intensities was taken.

Figure B.1: Topographic overview (openstreetmap.com) over the north part of the the Pedernales block. The site PED, marked with a black star, is located at the road E382 from Pedernales to Santa Domingo de Los Colorados. Below a photography of the site is shown with the three sampled flows indicated in white.

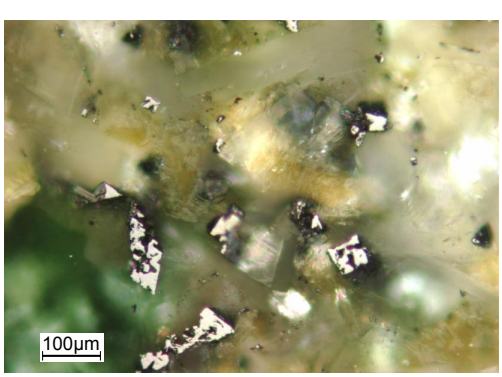

Locality:	Pedernales
Coordinates:	0°2'2.3"N 79°57'17.5"W
Block:	Pedernales
Formation:	Piñon
Age:	88.8 ± 1.6 Ma

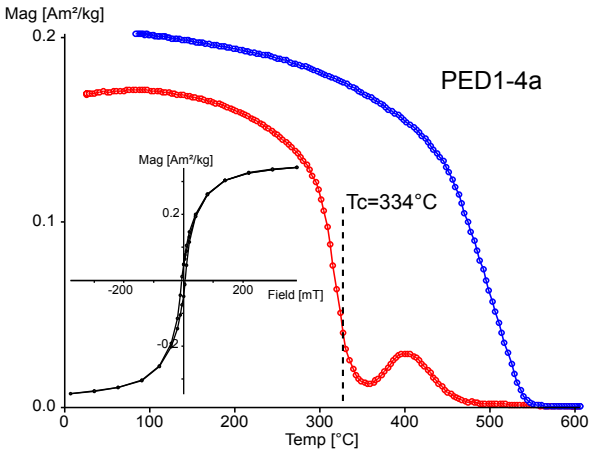

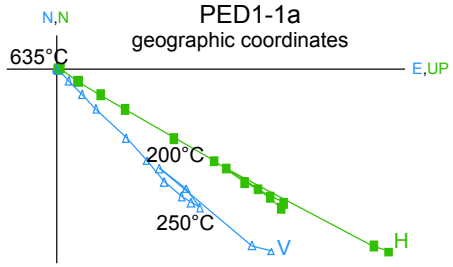

Figure B.2: Rock magnetic images of site PED together with site information. The microscopy image (50 x oil lens) shows sceletonal magnetic minerals, an indication for a late crystallization. Thermomagentic experiments indicate the presence of a magnetic phase, which alters to pure magnetite while heated. Hysteresis loops show a ferromagnetic phase. Orthogonal plots (blue triangles: declination, green squares: inclination, geographic coordinates) show a single component which gets overprintend at 200°C. This could be a hint to a partial self-reversal often observed in titanomaghemites (Krasa *et al.*, 2005). The rock magnetism of the site VEN is very similar to PED and thus not shown here.

Figure B.3: Topographic overview over the southern part of the Pedernales block. The sites SRO and VEN are marked with red stars. Below photographies of the two sites are shown.

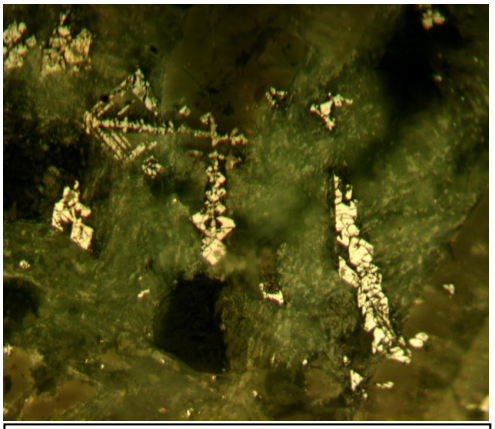

Locality:	San Rocque (SRO)
Coordinates:	0°15'18.7"S 80°10'52.2"W
Block:	Pedernales
Formation:	Piñon
Age:	88.8 ± 1.6 Ma

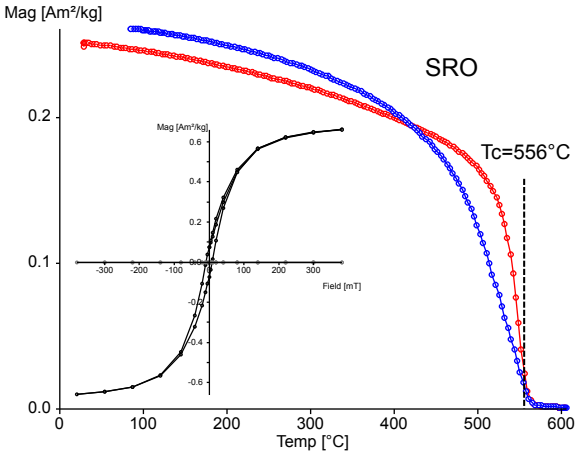

Figure B.4: Rock magnetic images of site SRO together with site information. The microscopy image (50 x oil lens) shows cruciform structures of the magnetic minerals, an indication for a late crystallization. Thermomagnetic experiments indicate the presence of pure magnetite. Hysteresis loops show a ferromagnetic phase.

Manta area

In the region between Manta and Portoviejo the San Lorenzo block of the Piñon terrane three sites of the Piñon Formation were sampled. First paleomagnetic sampling in the Manta block was done by Roperch *et al.* (1987, presumably the same sites as ours). Sites were found using geological map Montecristi (1971) from the DINAGE. The site CMC is located in at the Cerro Montecristi in the Holcim quarry, which can be accessed through El Chorillo west of Montecristi. As stratigraphy was ambiguous a handsample for paleointensities was taken. The sites Cerro de Hoja West and Cerro de Hoja East (CHW and CHE) are located in the active quarry of the Family Poggi north of La Pila. The first site CHW consists of massive columnar basalts and is located under the weathered pillows and about 100m sediments in the western part of the quarry. The pillows were too weathered to be sampled, the sediments were used to estimate the age of the volcanics (). The rock was very magnetic and deflected out orientation device. 17 oriented cores were drilled in the columnar basalts, which were used to estimate the bedding attitude. The other site CHN is located at the eastern part of the quarry.

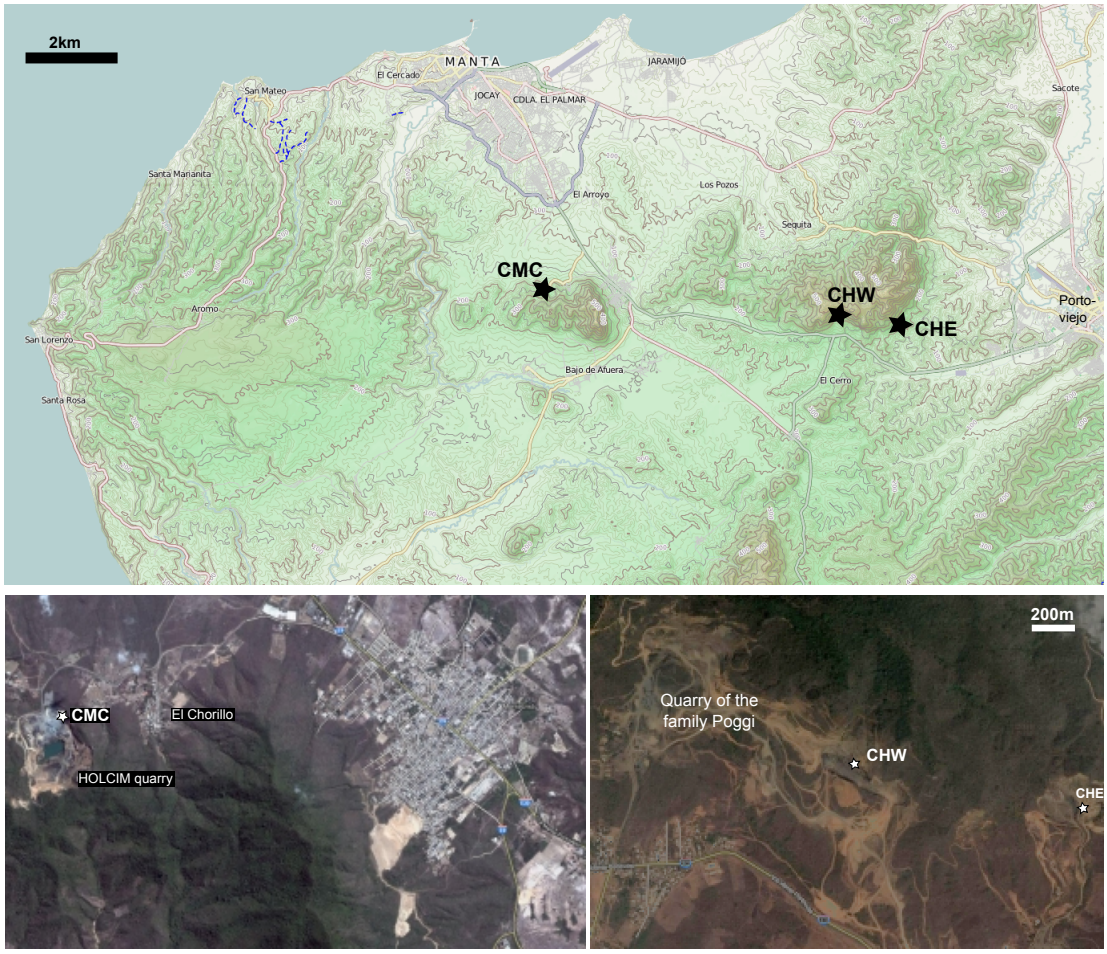

Figure B.5: Topographic overview (openstreetmap.com) over the Manta region. The sites CMC, CHW and CHE are marked with black stars. Below shown are closeup satellite image (google.com) of the site CMC in the Holcim quarry and of the sites CHW and CHE.

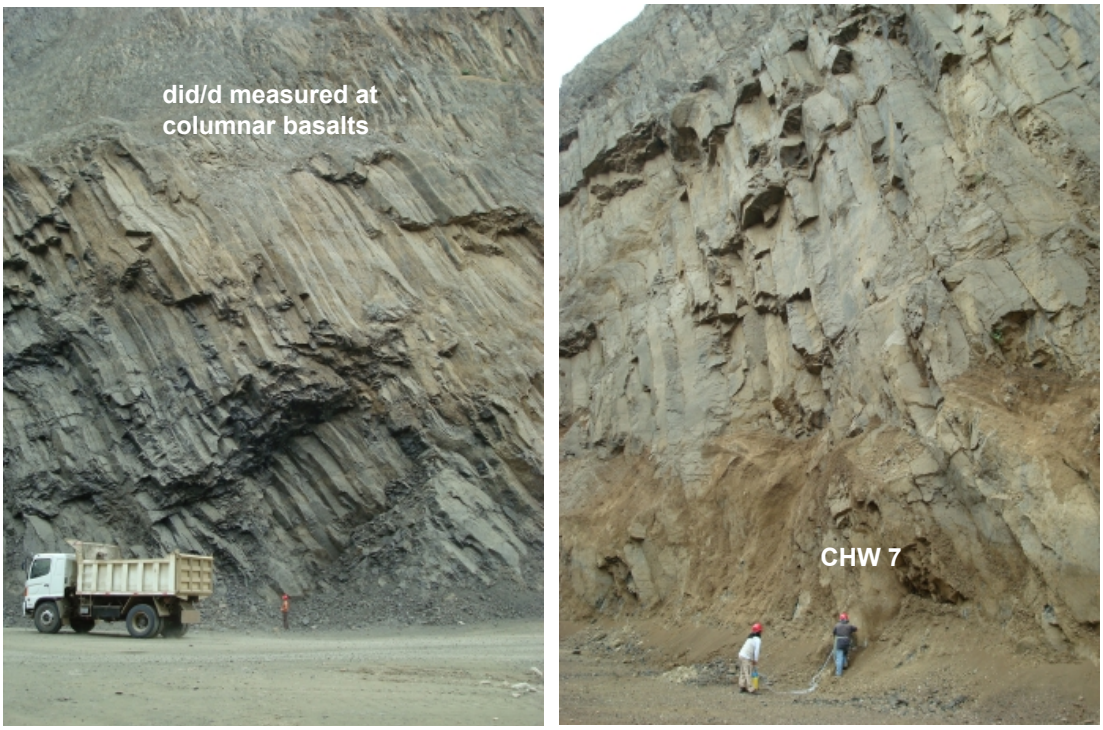

Figure B.6: Two photographs of the columnar basalt of CHW.

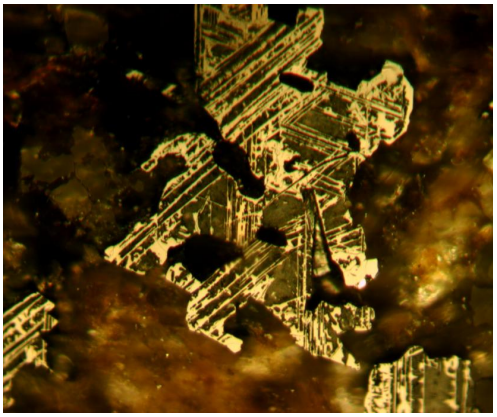

Locality:	Cerro Montecristi (CMC)
Coordinates:	1°2'38.1"S 80°41'19.7"W
Block:	San Lorenzo
Formation:	Piñon
Age:	88.8 ± 1.6 Ma

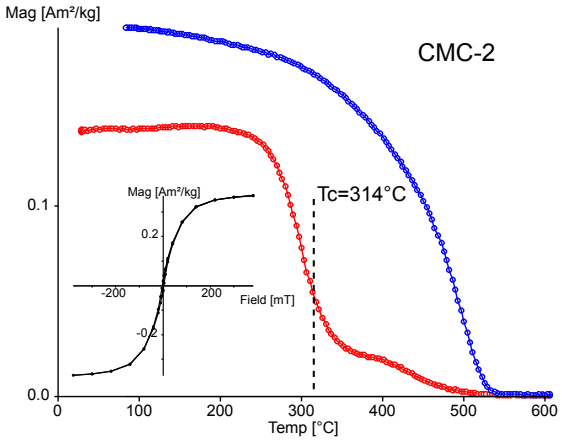

Figure B.7: Rock magnetic images of site CMC together with site information. The microscopy image (50 x oil lens) shows a magnetic mineral with exsolution lamellae, a hint for high temperature oxidation. Thermomagnetic experiments indicate the presence of a magnetic phase which alters to pure magnetite while heated (similar to site PED and VEN). Hysteresis loops show a ferromagnetic phase.

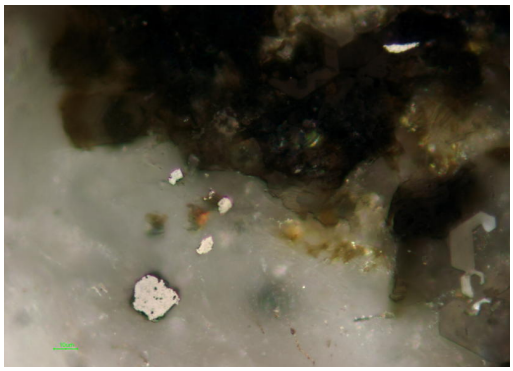

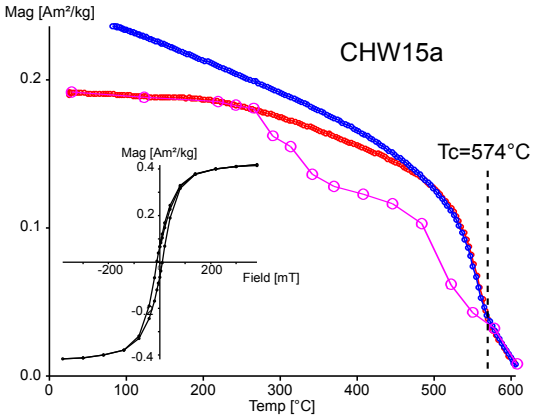

Locality:	Cerro de Hoja (CHW, CHE)
Coordinates:	1°3'20.0"S 80°33'48.7"W
Block:	San Lorenzo
Formation:	Piñon
Age:	88.8 ± 1.6 Ma

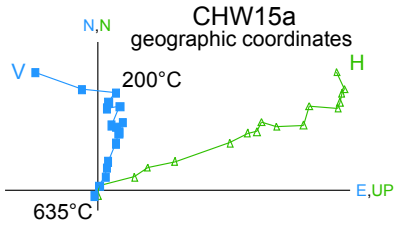

Figure B.8: Rock magnetic images of the sites CHW and CHE together with site information. The microscopy image (50 x oil lens) shows a near-euhedral magnetic mineral. Thermomagnetic experiments (heating curve in red, cooling curve in blue) indicate the presence of a magnetic phase which alters to pure magnetite while heated (similar to site PED, VEN and CMC) or the mixture of titanomagnetite and pure magnetite (can only be seen in stepwise demagnetization, decay plot in magenta). Hysteresis loops show a ferromagnetic phase. Orthogonal plots (blue triangles: declination, green squares: inclination, geographic coordinates) show a low temperature overprint under 200 °C.

Chongon-Colonche Sierra

In the low Chongon-Colonche Sierra 4 sites of the Piñon block were sampled. Roperch *et al.* (1987) and Luzieux (2007) sampled in this area earlier. Sites were found using the geological map Pedro Carbo (CT-MIV-F) from the DINAGE. The sites LMC and SAB are located south of the Highway 9 from Nobol to Jipijapa. Site SAB outcrops in the streambed of Rio Paco under the bridge of a dirt road to the south from Lomas de Sargentillo. Bedding attitude was not visible, thus an unoriented handsample was taken for paleointensities. The site LMC is can be found when following a road from Sabaneta to the east along Rio Paco passing the Hacienda Denise. The outcrop is an abandoned quarry and consists of two lava flows divided by pillows. The uppermost flow was too weathered and therefore not sampled.

Two more sites are located between Guayaquil and Nobol. Site CGE is the active quarry of the family Verdu south of Petrillo. The stratigraphy of the basalts was not visible any more due to active quarrying, but can be found in (Luzieux, 2007). Similar to the site LMC, again two flows divided by a layer of pillows can be seen.

The site CCO is located at the Guayaquil ringroad northeast of Jardin Botanico between Pascuales /Las Orquideas and the Rio Daule. At the eastern mountainside of the the Cerro Colorado oriented cores from 4 different flows were drilled. Oddly enough, the bedding attitude here suggests a dip to the north, while all other outcrops in the Piñon block dip to the south.

More outcrops of the Piñon Formation can be found on the Isla de la Plata in the formation La Plata I. (Celma *et al.*, 2005; Cantalamessa and Celma, 2004), but were not sampled by us.

Figure B.9: Topographic overview (openstreetmap.com) over the eastern part of Sierra Chongon-Colonche. Sampled sites are marked with black stars. Also shown is a photography of the site LMC with the three flows and pillows marked in white. No photography extists of site SAB.

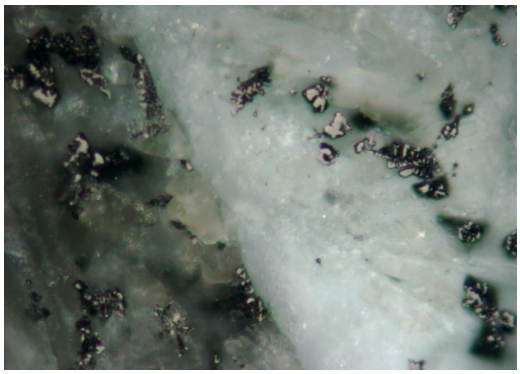

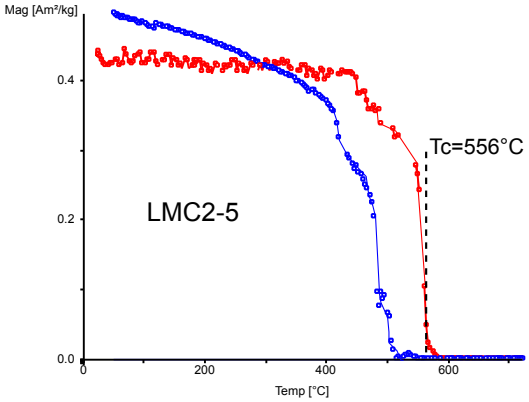

Locality:	Las Mercedes (LMC)
Coordinates:	1°57'55.4"S 80°8'58.1"W
Block:	Piñon
Formation:	Piñon
Age:	88.8 ± 1.6 Ma

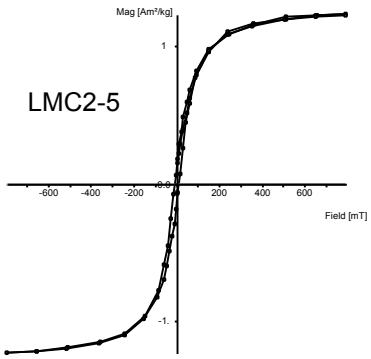

Figure B.10: Rock magnetic images of the site LMC together with site information. The microscopy image (50 x oil lens) shows skeletonal magnetic minerals, indicating a late crystallization. Thermomagnetic experiments (heating curve in red, cooling curve in blue) indicate the presence of pure magnetite. Hysteresis loops show a ferromagnetic phase.

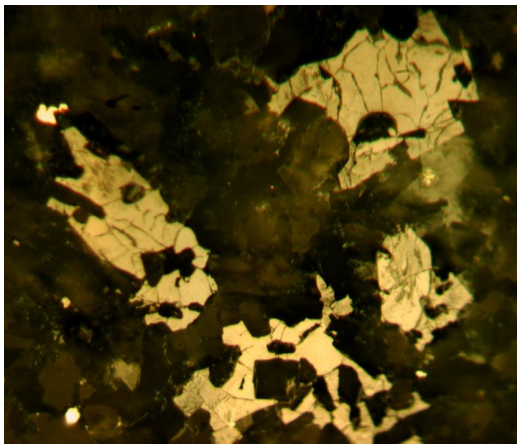

Locality:	Sabaneta (SAB)
Coordinates:	2°0'17.8"S 80°10'29.2"W
Block:	Piñon
Formation:	Piñon
Age:	88.8 ± 1.6 Ma

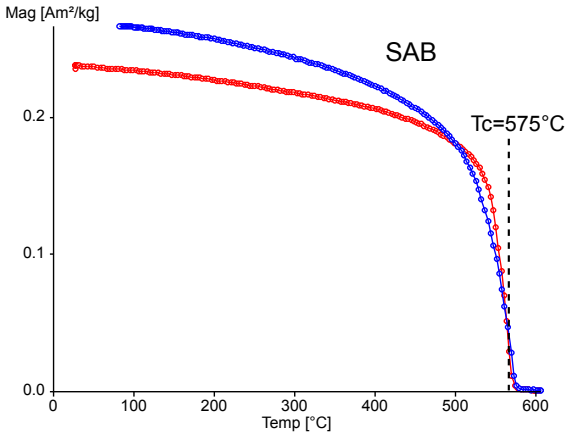

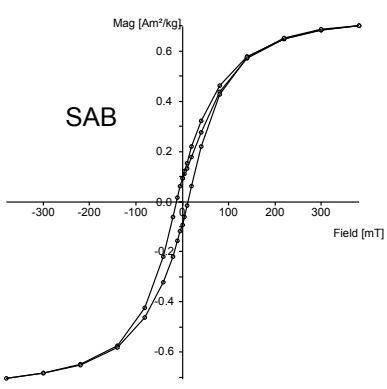

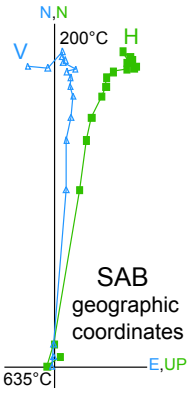

Figure B.11: Rock magnetic images of the site SAB together with site information. The microscopy image (50 x oil lens) shows magnetic minerals with numerous shrinking cracks, indicating a low temperature oxidation with accompanying reduction of mineral volume. Thermomagnetic experiments (heating curve in red, cooling curve in blue) indicate the presence of pure magnetite. Hysteresis loops show a ferromagnetic phase. Orthogonal plots (blue triangles: declination, green squares: inclination, geographic coordinates) show a low temperature overprint under 200 °C.

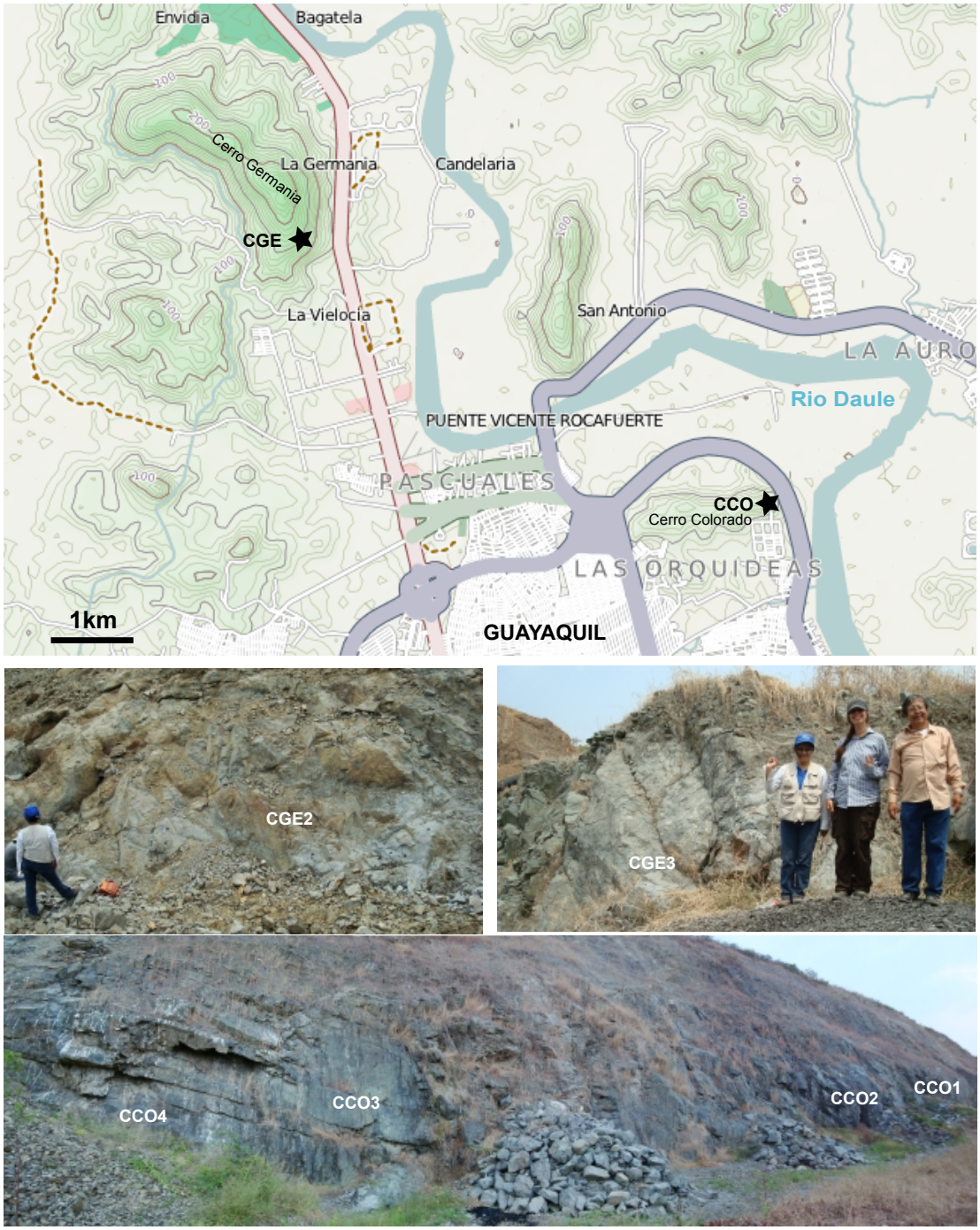

Figure B.12: Topographic overview (openstreetmap.com) over the Sierra Chongon-Colonche north of Guayaquil. The sampled sites CGE and CCO are marked with black stars. Also shown are photographs of the sites CGE and CCO LMC with the flow numbers shown in white.

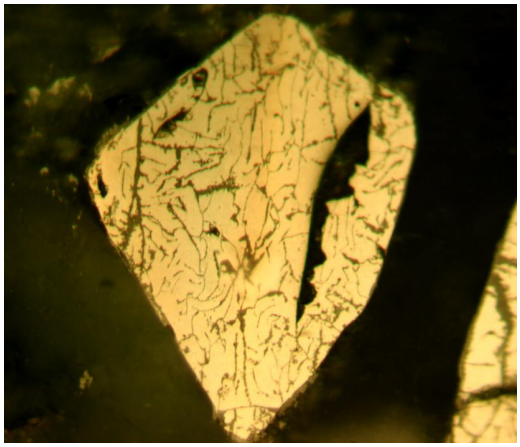

Locality:	Cerro Germania (CGE)
Coordinates:	2°2'31.3"S 79°57'1.3"W
Block:	Piñon
Formation:	Piñon
Age:	88.8 ± 1.6 Ma

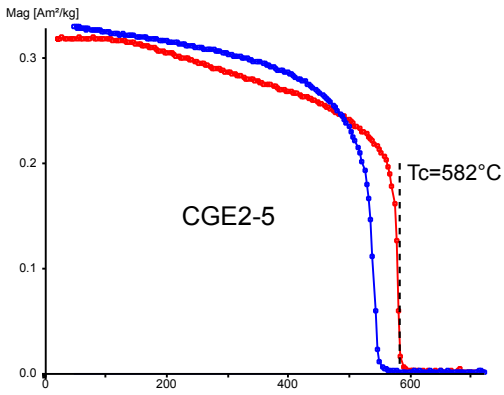

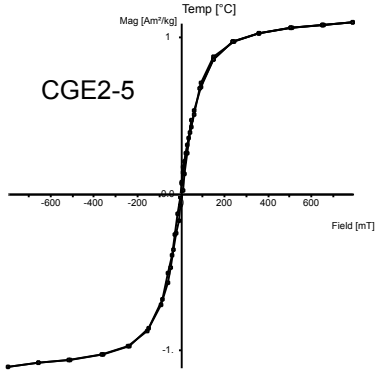

Figure B.13: Rock magnetic images of the site CGE together with site information. The microscopy image (50 x oil lens) shows magnetic minerals with numerous shrinking cracks, indicating a low temperature oxidation with accompanying reduction of mineral volume. Thermomagnetic experiments (heating curve in red, cooling curve in blue) indicate the presence of pure magnetite. Hysteresis loops show a ferromagnetic phase.

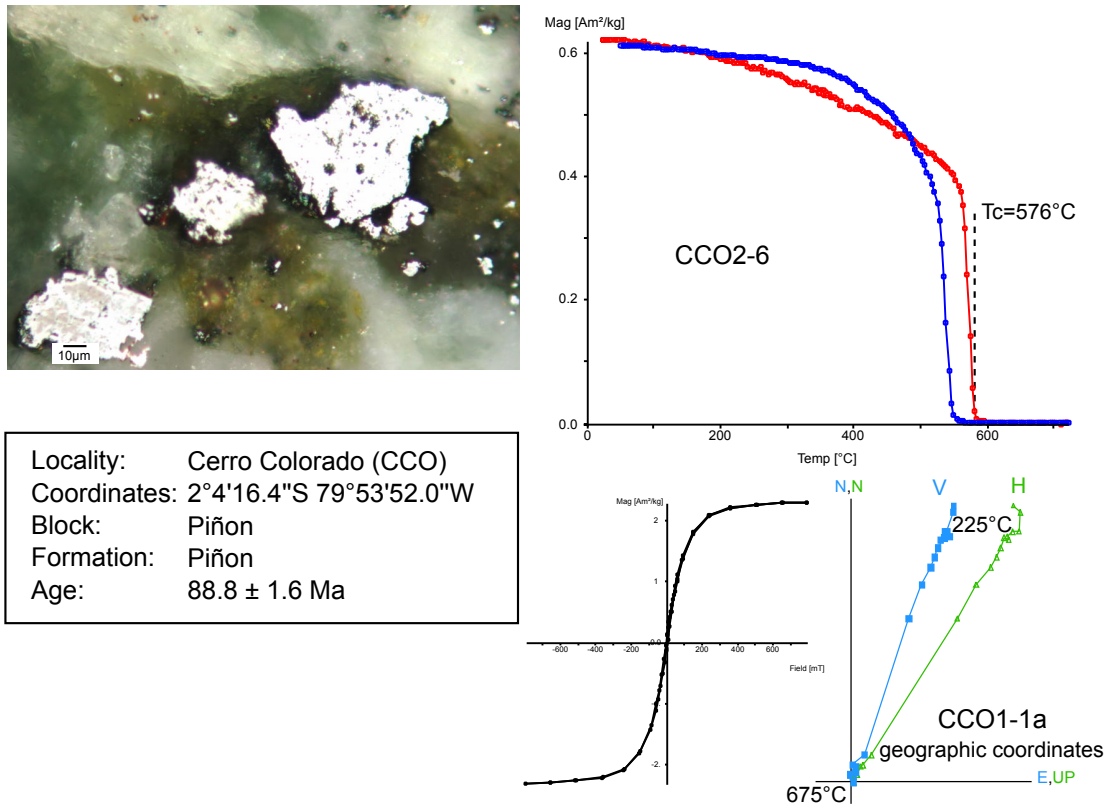

Figure B.14: Rock magnetic images of the site CCO together with site information. The microscopy image (50 x oil lens) shows a fresh magnetic minerals. Thermomagnetic experiments (heating curve in red, cooling curve in blue) suggest the presence of pure magnetite. Hysteresis loops show a ferromagnetic phase. Orthogonal plots show a single primary component.

Western Cordillera

The Pallatanga Formation (87.1 ± 1.66 Ma, U/Pb SHRIMP on zircons in layered gabbro from Vallejo Cruz, 2007), which outcrops mainly south of Guaranda and is named after the village Pallatanga north of Multitud. Sites were found using the geological map Mapa Geologico de la Cordillera Occidental del Ecuador entre 2° and 3° from the DINAGE. The site CMA (Cordillera Multitude Alausi) is located at the dirt road from Multitud to Alausi. Bedding attitude was not clearly visible at this site, thus we took unoriented handsamples for paleointensity determination.

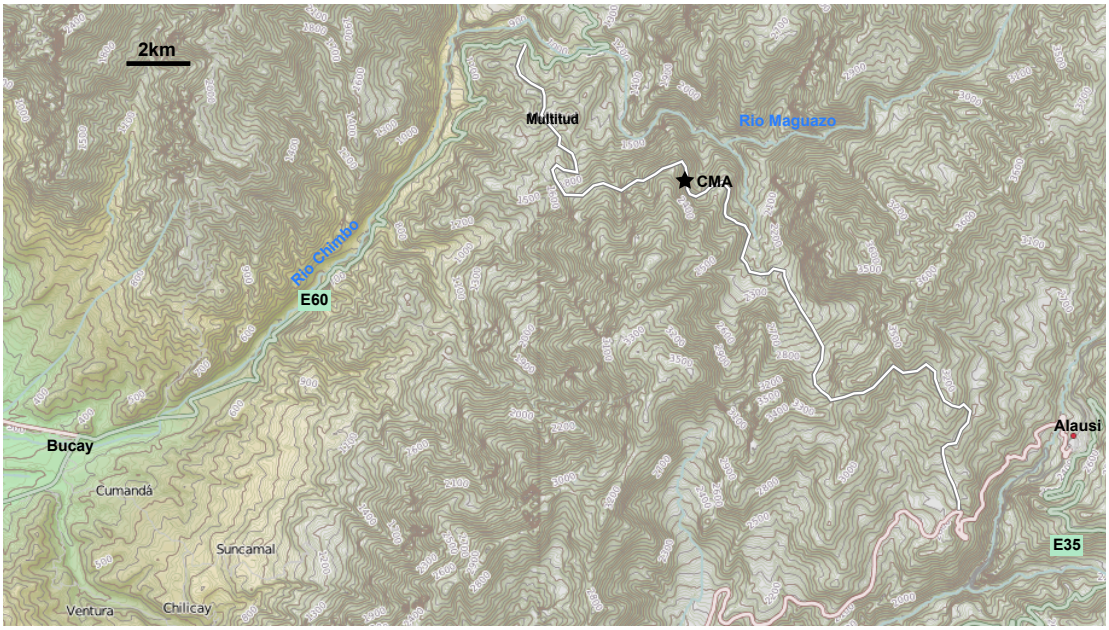

Figure B.15: Topographic overview (openstreetmap.com) the Western Cordillera east of Bucay. The site CMA marked with a black star is located at the dirt road from Multitude to Alausi (not mapped).

Locality:	Multitude Alausi (CMA)
Coordinates:	2°7'43.3"S 78°57'29.7"W
Block:	Pallatanga
Formation:	Pallatanga
Age:	87.1 ± 1.66 Ma

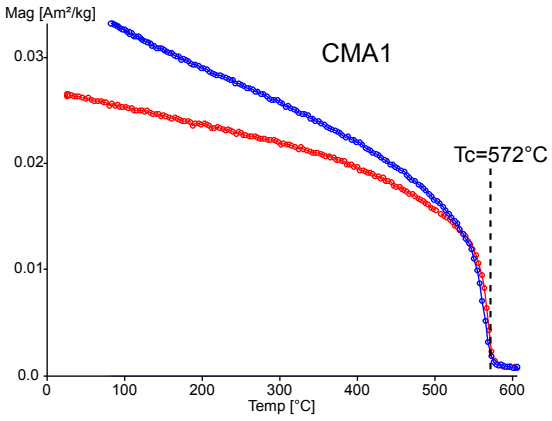

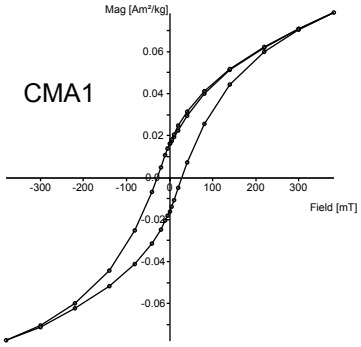

Figure B.16: Rock magnetic images of site CMA together with site information. The microscopy image (10 x air lens) shows a magnetic mineral which underwent high temperature oxidation, dividing the original titanomagnetite up into magnetite and illmenite. However, the mineral is heavily alterated, the illmenite completly dissoluted with the surrounding matrix. Thermomagnetic experiments show the presence of pure magnetite (in agreement with the microscopy image). Hysteresis loops show a ferromagnetic phase plus a paramagnetic response. No paleodirections were measured from this site.

Celica-Lancones basin

We sampled four sites in the Albian volcanics of the Peruvian Lancones formation and the Ecuadorian Celica Formation, which were deposited in the Celica-Lancones basin. Sites were found using the geological maps in Hungerbuhler *et al.* (2002); Jaillard (1996b); Mourier *et al.* (1988b). In Ecuador the site RPL is located in the stream bed of the Rio Playas west of Catacocha (Hungerbuhler *et al.*, 2002). This is also the site from which the age of the Celica formation was estimated to be Albian (Jaillard, 1996b). Due to an unclear stratigraphy of the Celica Formation at this site we took an unoriented handsample for paleointensity determination.

Following the E35 from Catacocha to the south in direction of Macará the site CEL can be found 500 m east of the village Celica along the road to El Enpalme at about 2000m altitude. The stratigraphy has a ambiguous bedding attitude, with flow CEL1 dipping to east and the succeeding flows (CEL2 and CEL3) dipping to south-east. Nevertheless, we took 11 samples from the 3 different flows.

After crossing the border to Peru at Macará the site RQU can be found after Suyo 8km down the Panamericana Norte at the bridge over the Rio Quiroz. The two sampled lava flows in the streambed could be distinguished by breccia in between.

Two more flows were sampled at the west coast of the reservoir Represa San Lorenzo (RSL) at the foot of the Andes. This site is located east of the Las Lomas.

Figure B.17: Topographic overview (openstreetmap.com) over the northern part of the Celica-Lancones basin. The sites RPL and CEL are marked with black stars. The location of nearby cities Celica, El Enpalme and Catacocha is indicated. Below shown are a closeup satellite image (google.com) and a photography of the site CEL with individual flows indicated in white. Not photography exists for the handsample site RPL.

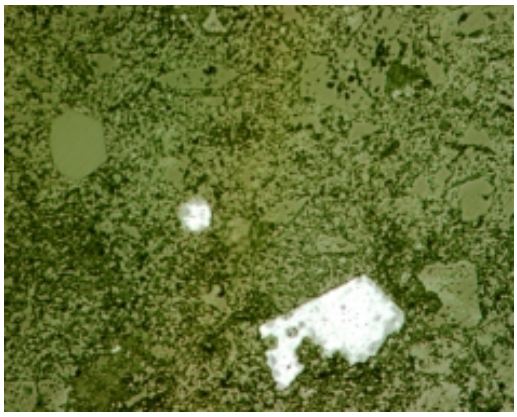

Locality:	Celica (CEL)
Coordinates:	4°6'13.1"S 79°56'48.9"W
Block:	Amotape
Formation:	Celica
Age:	Albian

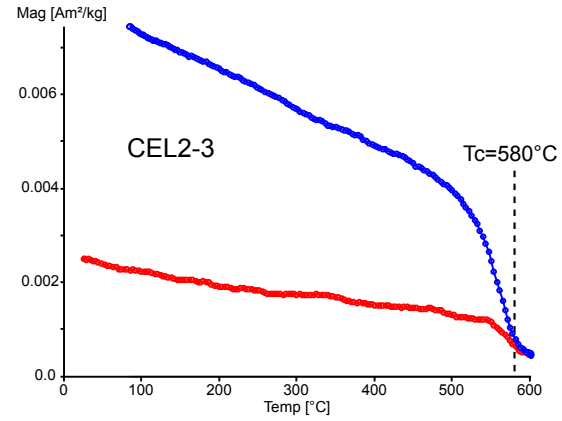

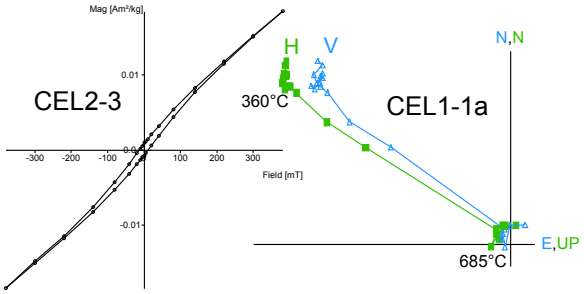

Figure B.18: Rock magnetic images of site CEL together with site information. The microscopy image (10 x air lens) shows a relatively fresh magnetic mineral. Thermomagnetic experiments show the presence of pure magnetite plus a second component which alters to magnetite while heating. Hysteresis loops indicate the presence of a ferromagnetic and a paramagnetic phase. Orthogonal plots (blue triangles: declination, green squares: inclination, geographic coordinated) show one single component.

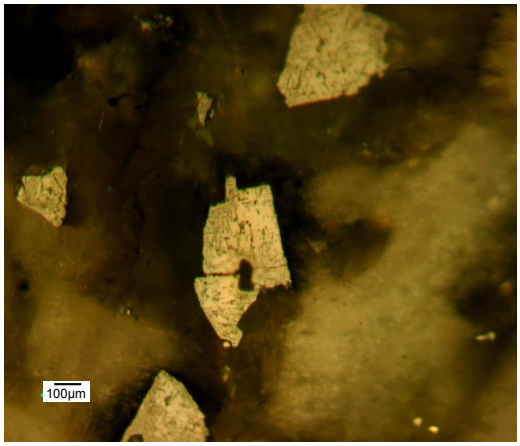

Locality:	Rio Playas (RPL)
Coordinates:	4°2'36.5"S 79°41'07.1"W
Block:	Amotape
Formation:	Amotape
Age:	Albian

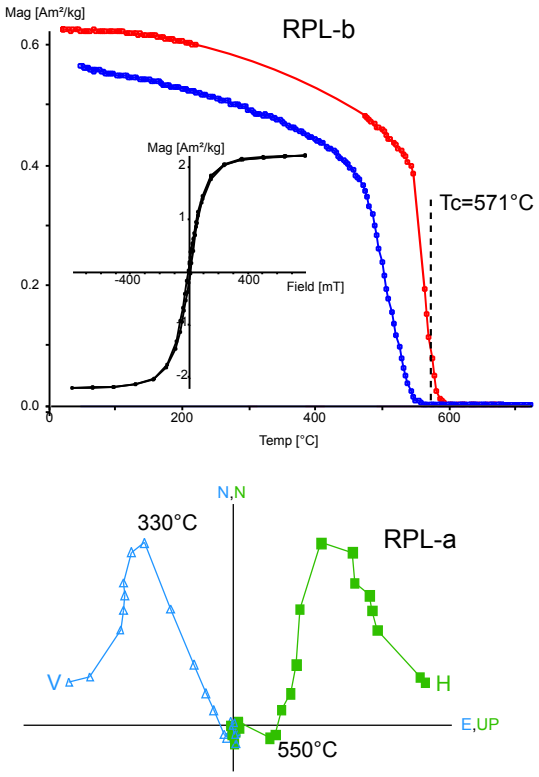

Figure B.19: Rock magnetic images of site RPL together with site information. The microscopy image (50 x oil lens) shows numerous shrinking cracks in the magnetic minerals, a hint for low temperature oxidation with accompanying lost of volume. Thermomagnetic experiments indicate the presence of pure magnetite.Orthogonal plots (blue triangles: declination, green squares: inclination, geographic coordinated as unoriented sample) show a low temperature overprint under 330°C. But also the high temperature component is most likely not primary, as it does not demagnetize into the origin.

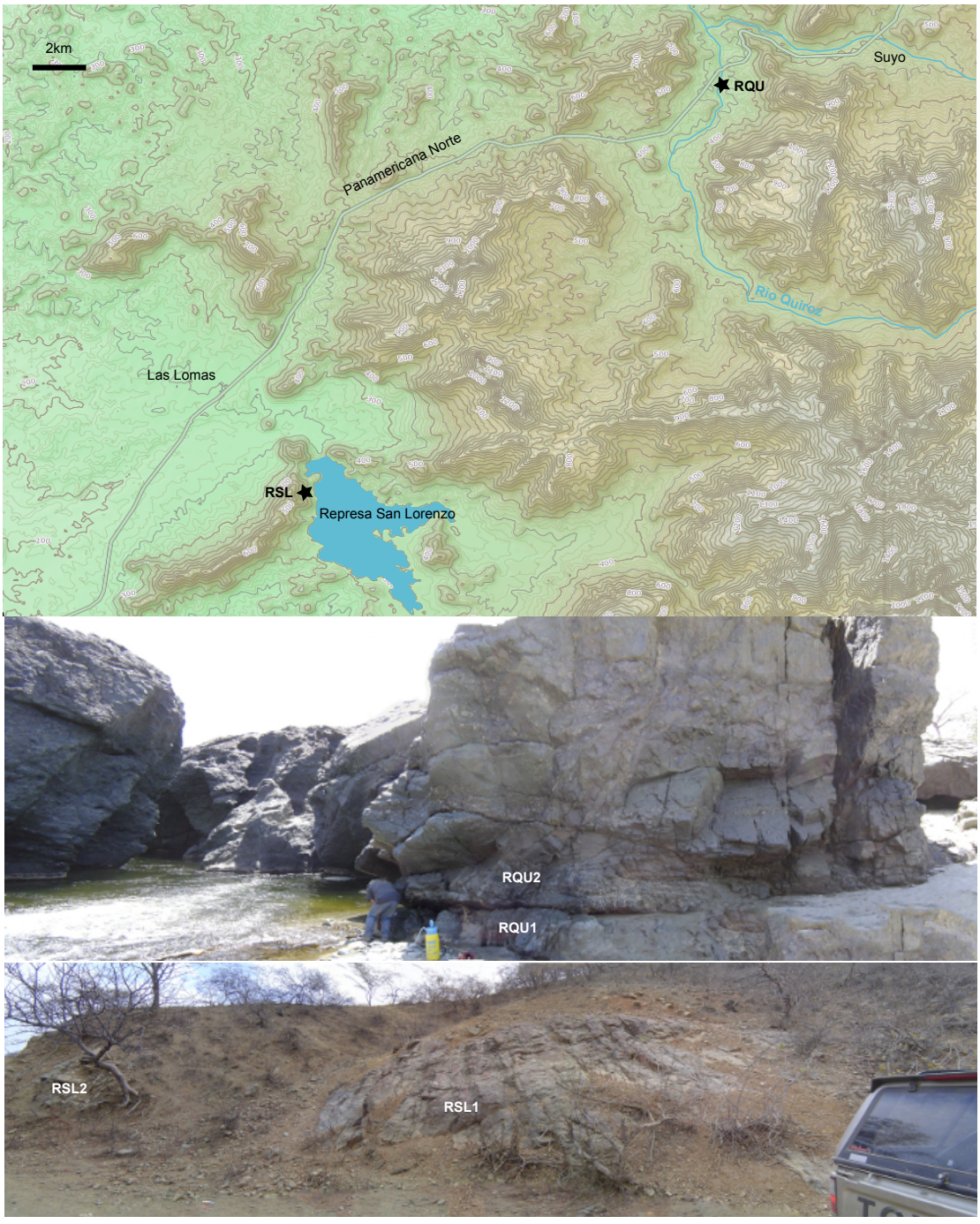

Figure B.20: Topographic overview (openstreetmap.com) over the southern part of the Celica-Lancones basin. The sites RQU and RSL are marked with black stars. The location of nearby cities Las Lomas and Suyo is indicated. Below shown are photographs of the sites RQU and RSL with flow names shown in white.

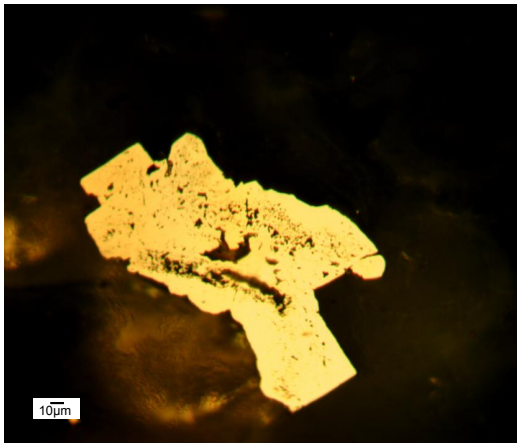

Locality:	Rio Quiroz (RQU)
Coordinates:	4°31'34.0"S 80°3'30.0"W
Block:	Amotape
Formation:	Lancones
Age:	Albian

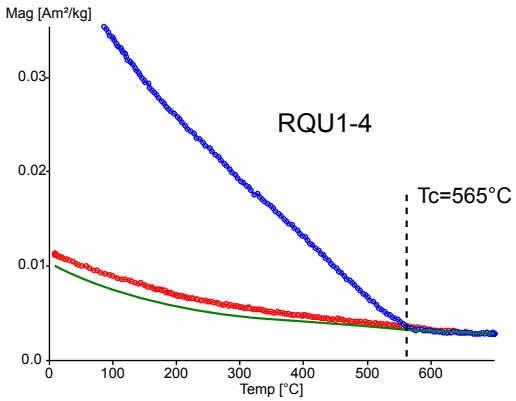

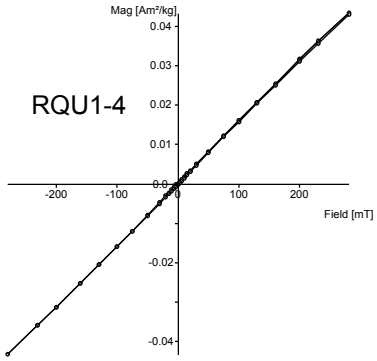

Figure B.21: Rock magnetic images of site RQU together with site information. The microscopy image (50 x oil lens) shows a relatively fresh magnetic mineral. However, thermomagnetic experiments and hysteresis loop indicate a predominantly paramagnetic response (green line indicates paramagnetic decay with temperature) to an applied field and no remanence in these samples.

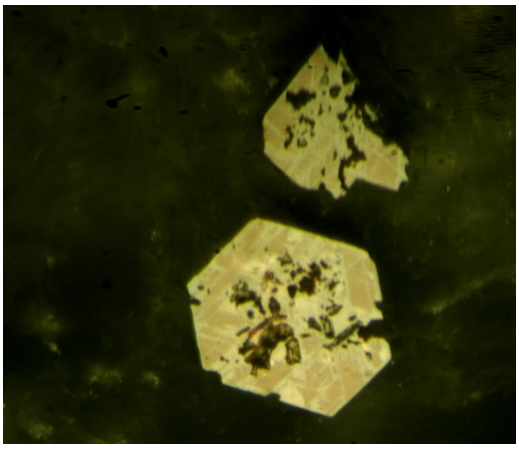

Locality:	Represa San Lorenzo (RSL)
Coordinates:	4°41'15.4"S 80°12'4.6"W
Block:	Amotape
Formation:	Lancones
Age:	Albian

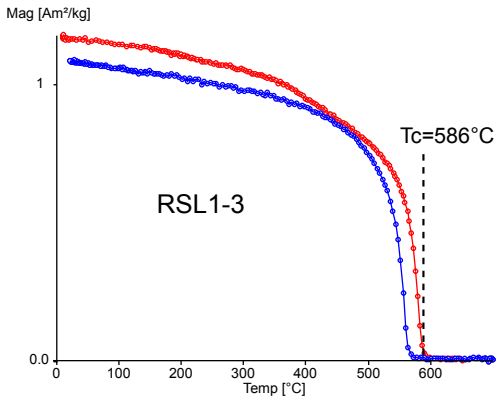

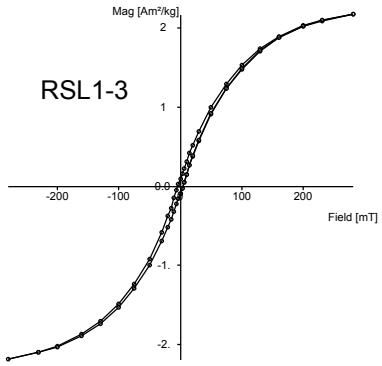

Figure B.22: Rock magnetic images of site RSL together with site information. The microscopy image (125 x oil lens) shows an euhedral magnetite with exolution lamellae, indicating high temperature oxidation of titanomagnetite to magnetite and illmenite. Thermomagnetic experiments show the presence of pure magnetite (in agreement with the microscopy image).

References

Audebaud, E., Capdevila, R., Dalmayrac, B., Debelmas, J., Laubacher, G., Lefevre, C., Marocco, R., Martinez, C., Mattauer, M., Megard, F., Paredes, J., and Tomasi, P. (1973). Les traits géologiques essentiels des Andes Centrales (Pérou, Bolivie). *Rev. Géogr. phys. Géol. dynam.*, **15**, 73–113. Cited in section(s) 2.1.3.

Baag, C.-G. and Helsley, C. E. (1974). Geomagnetic Secular Variation Model E. *Journal of Geophysical Research*, **79**(32), 4918–4922. Cited in section(s) 3.1.1.

Benavides-Cáceres, V. E. (1956). Cretaceous system in northern Peru. *Bulletin of the American Museum of the Natural History*, **108**, 352–494. Cited in section(s) 2.1.2, 2.1.2, and 2.1.2.

Benitez, S. B. (1995). Évolution géodynamique de la province côtière sud-équatorienne au Crétacé supérieur-Tertiaire The geodynamic évolution of the coastal Ecuatorian province during the upper Cretaceous-Tertiary Evolucîon geodynâmica de la provincia sur-equatoriana en el Cret. *Géologie Alpine*, **71**, 3–163. Cited in section(s) 4.1.2.

Besse, J. (2002). Apparent and true polar wander and the geometry of the geomagnetic field over the last 200 Myr. *Journal of Geophysical Research*, **107**(B11), 2300. Cited in section(s) 2.1.3 and 2.9.

Biggin, A. J., Strik, G. H. M. A., and Langereis, C. G. (2008a). Evidence for a very-long-term trend in geomagnetic secular variation. *Nature Geoscience*, **1**(6), 395–398. Cited in section(s) 3.1.1.

Biggin, A. J., van Hinsbergen, D. J. J., Langereis, C. G., Straathof, G. B., and Deenen, M. H. L. (2008b). Geomagnetic secular variation in the Cretaceous Normal Superchron and in the Jurassic. *Physics of the Earth*

and Planetary Interiors, **169**(1-4), 3–19. Cited in section(s) 2.1.1, 2.1.4, 2.1.4, 2.1.4, 2.13, 2.1.5, 3.1.1, and 5.

Bloxham, J. and Gubbins, D. (1985). The secular variation of Earth's magnetic field. *Nature*, **317**(6040), 777–781. Cited in section(s) 2.1.1 and 3.1.1.

Brock, A. (1971). An Experimental Study of Palaeosecular Variation. *Geophysical Journal International*, **24**(3), 303–317. Cited in section(s) 3.1.3 and 5.

Buffett, B. A. (2007). 8.12 - CoreMantle Interactions. In E.-i.-C. G. Schubert, Herausgeber, *Treatise on Geophysics*, Seiten 345–358. Elsevier, Amsterdam. Cited in section(s) 1.

Bullard, E. and Gellman, H. (1954). Homogeneous dynamos and terrestrial magnetism. *Phil. Trans. Roy. Soc. London*, **A247**, 213–255. Cited in section(s) 1.

Butler, R. F. (1998). *Paleomagnetism: Magnetic Domains to Geologic Terranes*. Electronic edition. Cited in section(s) 1, 3.2, and 3.2.

Calvo-Rathert, M., Goguitchaichvili, A., Bógalo, M.-F., Vegas-Tubía, N., Carrancho, A., and Sologashvili, J. (2011). A paleomagnetic and paleointensity study on Pleistocene and Pliocene basaltic flows from the Djavakheti Highland (Southern Georgia, Caucasus). *Physics of the Earth and Planetary Interiors*. Cited in section(s) 3.1.1.

Cantalamessa, G. and Celma, C. D. (2004). Origin and chronology of Pleistocene marine terraces of Isla de la Plata and of flat, gently dipping surfaces of the southern coast of Cabo San Lorenzo (Manabi, Ecuador). *Journal of South American Earth Sciences*, **16**, 633–648. Cited in section(s) B.

Cejudo Ruiz, R., Goguitchaichvili, A., Geuna, S. E., Alva-Valdivia, L. M., Sole, J., and Morales, J. (2006). Early cretaceous absolute geomagnetic paleointensities from Cordoba Province (Argentina). *Earth Planets Space*, (2), 1333–1339. Cited in section(s) 4.1.1.

Cejudo Ruiz, R., Goguitchaichvili, A., Morales, J., Trindade, R. I. F., Alva-Valdivia, L. M., and Urrutia-Fucugauchi, J. (2009). Absolute Thellier paleointensities from Ponta Grossa dikes (southern Brazil) and the early Cretaceous geomagnetic field strength. *Geofísica Internacional*, **48**(2), 243–252. Cited in section(s) 4.1.1.

Celma, C. D., Camerino, U., and Mc, I.-C. (2005). Basin physiography and tectonic influence on sequence architecture and stacking pattern: Pleistocene succession of the Canoa Basin (central Ecuador). *Geological Society of America, Bulletin*, **117**(9/10), 1226–1241. Cited in section(s) B.

Cervantes Solano, M., Goguitchaichvili, A., Sánchez Bettucci, Leda Cejudo Ruiz, Ruben Calvo-Rathert, Manuel Ruiz-Martinez, V. C., Ruth Soto, R., and Alva-Valdivia, L. M. (2010). Paleomagnetism of early cretaceous arapey formation (Northern Uruguay). *Studia Geophysica et Geodaetica*, **54**(4), 533—-546. Cited in section(s) 4.1.1.

Chatterjee, J. (1956). The crust as the possible seat of earth's magnetism. *J. Atmosph. Terr. Phys.*, **8**, 233–239. Cited in section(s) 1.

Chulliat, A. and Telali, K. (2007). World monthly means database project. *Publs. Inst. Geophys. Pol. Acad. Sc., C-99 (398)*, **268**(398). Cited in section(s) 3.1.2.

Coe, R. (1967). Paleo-Intensities of the Earths Magnetic Field Determined from Tertiary and Quaternary Rocks. *Journal of Geophysical Research*, **72**(12), 3247 – 3262. Cited in section(s) 4.1.3.

Coe, R. S., Gromme, S., and Mankinen, E. A. (1978). Geomagnetic paleointensities from radiocarbon-dated Lava Flows on Hawaii and the Question of the Pacific Nondipole Low. *Journal of Geophysical Research*, **83**(B4), 1740 —-1756. Cited in section(s) 4.1.

Constable, C. G. and Parker, R. L. (1988). Statistics of the Geomagnetic Secular Variation for the Past 5 m.y. *Journal of Geophysical Research*, **93**(B10), 11569–11581. Cited in section(s) 2.1.1 and 3.1.1.

Courtillot, V. and Besse, J. (1987). Magnetic field reversals, polar wander, and core-mantle coupling. *Science*, **237**(4819), 1140. Cited in section(s) 2.1.1.

Cox, A. (1962). Analysis of present geomagnetic field for comparison with paleomagnetic results. *J. Geomag. Geoelectr*, **13**(101), 101–112. Cited in section(s) 2.1.1, 3.1.3, 3.2, and 5.

Cox, A. (1969). Confidence Limits for the Precision Parameter k. *Geophysical Journal of the Royal Astronomical Society*, **17**(5), 545–549. Cited in section(s) 2.1.4, 3.1, 3.1.3, 3.2, and 5.

Cox, A. (1970). Latitude Dependence of the Angular Dispersion of the Geomagnetic Field. *Geophysical Journal of the Royal Astronomical Society*, **20**(3), 253–269. Cited in section(s) 2.1.1, 3.1.1, 3.1.1, 3.1.3, and 5.

Cox, A. (1975). The frequency of geomagnetic reversals and the symmetry of the nondipole field. *Reviews of Geophysics*, **13**(3), 35. Cited in section(s) 2.1.1.

Creer, K. (1962). The Dispersion of the Geomagnetic Field Due to Remote Times from Paleomagnetic Data. *Journal of Geophysical Research*, **57**(9), 3461—-3476. Cited in section(s) 1 and 3.2.

Creer, K. M., Irving, E., and Nairn, A. E. M. (1959). Palaeomagnetism of the Great Whin Sill. *Geophysical Journal of the Royal Astronomical Society*, **2**(4), 306–323. Cited in section(s) 2.1.1.

Cronin, M., Tauxe, L., Constable, C., Selkin, P., and Pick, T. (2001). Noise in the quiet zone. *Earth and Planetary Science Letters*, **190**(1-2), 13–30. Cited in section(s) 1, 2.1.1, 2.1.4, and 2.1.4.

de la Cruz Wetzell, J. and Leon Lacaros, W. (1995). 11g-Aramango. Instituto Geologico Minero y Metalurgico. Cited in section(s) 2.2.

de la Cruz Wetzell, J., Quispesilvana, L., Leon Lacaros, W., and Imana, M. (1995). 11f-San Ignacio. Instituto Geologico Minero y Metalurgico. Cited in section(s) 2.2.

Dekkers, M. and Böhnel, H. (2006). Reliable absolute palaeointensities independent of magnetic domain state. *Earth and Planetary Science Letters*, **248**(1-2), 507–516. Cited in section(s) 4.1.3.

Dhondt, A. V. and Jaillard, E. (2005). Cretaceous bivalves from Ecuador and northern Peru. *Journal of South American Earth Sciences*, **19**(3), 325–342. Cited in section(s) 2.1.2, 2.1.2, and 2.1.2.

Dorbath, C. (1996). Velocity structure of the Andes of central Peru from locally recorded earthquakes. *Geophys. Res. Lett.*, **23**, 205—-208. Cited in section(s) 2.1.3.

Eide, E. A. and Torsvik, T. H. (1996). Paleozoic supercontinental assembly, mantle flushing, and genesis of the Kiaman Superchron. *Earth and Planetary Science Letters*, **144**(3-4), 389–402. Cited in section(s) 1 and 2.1.1.

Elsasser, W. M. (1946). Induction Effects in Terrestrial Magnetism. *Physical Review*, **69**(3-4), 106 —- 116. Cited in section(s) 1.

Fabian, K. and Leonhardt, R. (2010). Multiple-specimen absolute paleointensity determination: An optimal protocol including pTRM normalization, domain-state correction, and alteration test. *Earth and Planetary Science Letters*, **297**(1-2), 84–94. Cited in section(s) 4.1.3 and 4.2.

Fabian, K., Sherbakov, V., and Shcherbakov, V. (2010). Poisson goes , random walker comes : Explaining the power-law distribution of the durations of stable-polarity intervals. *Geophysical Research Abstracts*, **12**(EGU General Assembly 2010), 11717–11717. Cited in section(s) 2.1.1.

Fisher, R. (1953). Dispersion on a sphere. *Proceedings of the Royal Society of London. Series A, Mathematical and Physical Sciences*, **217**(1130), 295–305. Cited in section(s) 3.2.

Frank, U., Nowaczyk, N. R., and Negendank, J. F. W. J. F. W. (2007). Rock magnetism of greigite bearing sediments from the Dead Sea, Israel. *Geophysical Journal International*, **168**(3), 921–934. Cited in section(s) 2.1.3.

Fu, Y., von Dobeneck, T., Franke, C., Heslop, D., and Kasten, S. (2008). Rock magnetic identification and geochemical process models of greigite formation in Quaternary marine sediments from the Gulf of Mexico (IODP Hole U1319A). *Earth and Planetary Science Letters*, **275**(3-4), 233–245. Cited in section(s) 2.1.3 and 2.1.3.

Gallet, Y. and Hulot, G. (1997). Stationary and nonstationary behaviour within the geomagnetic polarity time scale. *Geophysical Research Letters*, **24**(15), 1875–1878. Cited in section(s) 1 and 2.1.1.

Gilder, S., Rousse, S., Farber, D., Mcnulty, B., Sempere, T., Torres, V., and Palacios, O. (2003). Post-Middle Oligocene origin of paleomagnetic rotations in Upper Permian to Lower Jurassic rocks from northern and southern Peru. *Earth and Planetary Science Letters*, **210**(1-2), 233–248. Cited in section(s) 2.1.3.

Glatzmaier, G. A., Coe, R. S., Hongre, L., and Roberts, P. H. (1999). The role of the Earth's mantle in controlling the frequency of geomagnetic reversals. *Nature*, **401**(October), 885–890. Cited in section(s) 1, 2.1.1, and 5.

Goguitchaichvili, A., Cejudo Ruiz, R., Bettucci Sanchez, L., Aguilar Reyes, B., Alva-Valdicia, L. M., Urrutia-Fucugauchi, J., Morales, J., and Calvo Rathert, M. (2008). New absolute paleointensity results from the Parana Magmatic Province (Uruguay) and the Early Cretaceous geomagnetic paleofield. *Geochemistry Geophysics Geosystems*, **9**(11), 1–12. Cited in section(s) 4.1.1.

Gradstein, F. M., Ogg, J. G., Smith, A. G., and Others (2004). *A geologic Time Scale*. Cited in section(s) 1, 2.1.1, 2.1.2, 2.3, 2.1.2, and 2.1.3.

Granot, R., Tauxe, L., Gee, J. S., and Ron, H. (2007). A view into the Cretaceous geomagnetic field from analysis of gabbros and submarine glasses. *Earth and Planetary Science Letters*, **256**, 1–11. Cited in section(s) 4.7 and 4.1.4.

Gubbins, D. (1999). The distinction between geomagnetic excursions and reversals. *Geophysical Journal International*, **137**, pp.F1–F3. Cited in section(s) 2.1.4.

Haldan, M. M., Langereis, C. G., and Evans, M. E. (2007). Paleosecular variation during the PCRS based on a new database of sedimentary and volcanic records. In *AGU Fall Meeting Abstracts*, Ausgabe 1, Seite 921. Cited in section(s) 2.1.4, 2.1.5, and 5.

Haldan, M. M., Langereis, C. G., Biggin, A. J., Dekkers, M. J., and Evans, M. E. (2009). A comparison of detailed equatorial red bed records of secular variation during the Permo-Carboniferous Reversed Superchron. *Geophysical Journal International*, **177**(3), 834–848. Cited in section(s) 1 and 3.1.1.

Harrison, C. G. A. (1995). Secular Variation of the Earth's Magnetic Field. *Journal of Geomagnetism and Geoelectricity*, **47**, 131–147. Cited in section(s) 2.1.1.

Heunemann, C. (1998). *Gesteinsmagnetische und elektronenmikroskopische Untersuchungen an rezenten Seesedimenten*. Diplomarbeit, Institut für Allgemeine und Angewandte Geophysik Ludwig-Maximilians-Universität München. Cited in section(s) 2.1.3.

Hext, G. R. (1963). The estimation of second-order tensors, with related tests and designs. *Biometrika*, **50**(3-4), 353. Cited in section(s) 2.8.

Hill, M., Pan, Y., and Davies, C. (2008). An assessment of the reliability of palaeointensity results obtained from the Cretaceous aged Suhongtu section, Inner Mongolia, China. *Physics of the Earth and Planetary Interiors*, **169**(1-4), 76–88. Cited in section(s) 4.7 and 4.1.4.

Hulot, G. and Gallet, Y. (1996). On the interpretation of virtual geomagnetic pole (VGP) scatter curves. *Physics of The Earth and Planetary Interiors*, **95**(1-2), 37–53. Cited in section(s) 3.1.1.

Hulot, G. and Gallet, Y. (2003). Do superchrons occur without any palaeomagnetic warning ? *Earth and Planetary Science Letters*, **210**(1-2), 191–201. Cited in section(s) 1, 2.1.1, and 5.

Hungerbuhler, D., Steinmann, M., Winkler, W., Seward, D., Egüez, A., Peterson, D. E., Helg, U., and Hammer, C. (2002). Neogene stratigraphy and Andean geodynamics of southern Ecuador. *Earth-Science Reviews*, **57**(1-2), 75–124. Cited in section(s) 4.1.2 and B.

Inglis, D. (1955). Theories of the Earth's magnetism. *Rev. Mod. Phys.*, **27**, 212–248. Cited in section(s) 1.

Irving, E. and Pullaiah, G. (1976). Reversals of the geomagnetic field, magnetostratigraphy, and relative magnitude of paleosecular variation in the phanerozoic. *Earth-Science Reviews*, **12**(1), 35–64. Cited in section(s) 3.1.1.

Irving, E. and Ward, M. a. (1964). A statistical model of the geomagnetic field. *Pure and Applied Geophysics*, **57-57**(1), 47–52. Cited in section(s) 2.1.1.

Jackson, A. and Bloxham, J. (1991). Mapping the fluid flow and shear near the core surface using the radial and horizontal components of the magnetic field. *Geophysical Journal International*, **105**(1), 199–212. Cited in section(s) 1 and 2.1.1.

Jacobs, J. A. (2001). The cause of superchrons. *Astronomy & Geophysics*, **42**(6), 6–30. Cited in section(s) 2.1.1.

Jaillard, E. (1987). Sedimentary evolution of an active margin during middle and upper cretaceous times: the north Peruvian margin from late aptian up to senonian. *Geologische Rundschau*, **76**(3), 677–697. Cited in section(s) 2.1.2.

Jaillard, E. (1996a). Cretaceous to early Paleogene tectonic evolution of the northern Central Andes (018S) and its relations to geodynamics. *Tectonophysics*, **259**(1-3), 41–53. Cited in section(s) 2.1.2 and 2.1.2.

Jaillard, E. (1996b). Sedimentary and tectonic evolution of the arc zone of Southwestern Ecuador during Late Cretaceous and early Tertiary times. *Journal of South American Earth Sciences*, **9**(1-2), 131–140. Cited in section(s) 4.1.2 and B.

Jaillard, E. and Arnaud-Vanneau, A. (1993). The Cenomanian Turonian transition on the Peruvian margin. *Cretaceous Research*, **14**, 585–605. Cited in section(s) 2.1.2.

Jaillard, E., Sempere, T., Soler, P., Carlier, G., and Marocco, R. (1995). The role of Tethys in the evolution of the northern Andes between Late Permian and Late Eocene times. *The Ocean Basins and Margins*, **8**, 463–492. Cited in section(s) 2.1.2.

Jaillard, E., Bengtson, P., and Dhondt, A. V. (2005). Late Cretaceous marine transgressions in Ecuador and northern Peru: a refined stratigraphic framework. *Journal of South American Earth Sciences*, **19**(3), 307–323. Cited in section(s) 2.1.2, 2.1.2, and 2.1.2.

Jiang, W.-T., Horng, C.-S., Roberts, A. P., and Peacor, D. R. (2001). Contradictory magnetic polarities in sediments and variable timing of neoformation of authigenic greigite. *Earth and Planetary Science Letters*, **193**(1-2), 1–12. Cited in section(s) 2.1.3.

Johnson, C. L., Constable, C. G., Tauxe, L., Barendregt, R., Brown, L. L., Coe, R. S., Layer, P., Mejia, V., Opdyke, N. D., Singer, B. S., Staudigel, H., Stone, D. B., and Others (2008). Recent investigations of the 05 Ma geomagnetic field recorded by lava flows. *Geochemistry Geophysics Geosystems*, **9**(4), Q04032. Cited in section(s) 2.1.4, 2.13, 2.1.5, and 5.

Jordan, T. E., Isacks, B. L., Allmendinger, R. W., Brewer, J. A., Ramos, V. A., and Ando, C. J. (1983). Andean tectonics related to geometry of the subducted Nazca plate. *Geol. Soc. Am. Bull.*, **94(27)**, 341–361. Cited in section(s) 2.1.3.

Juarez, M., Tauxe, L., Gee, J., and Pick, T. (1998). The intensity of the Earth's magnetic field over the past 160 million years. *Nature*, **394**(August), 878–881. Cited in section(s) 4.7 and 4.1.4.

Kent, D. V., Wang, H., and Rochette, P. (2010). Equatorial paleosecular variation of the geomagnetic field from 0 to 3 Ma lavas from the Galapagos Islands. *Physics of the Earth and Planetary Interiors*, **183**(3-4), 404–412. Cited in section(s) 3.1.1.

Kerr, A. C. and Tarney, J. (2005). Tectonic evolution of the Caribbean and northwestern South America : The case for accretion of two Late Cretaceous oceanic plateaus. *Geology*, **33**(4), 269–272. Cited in section(s) 4.1.4.

Khokhlov, A., Hulot, G., and Carlut, J. (2001). Towards a self-consistent approach to palaeomagnetic field modelling. *Geophysical Journal International*, **145**(1), 157–171. Cited in section(s) 3.1.3 and 5.

Khokhlov, A., Hulot, G., and Bouligand, C. (2006). Testing statistical palaeomagnetic field models against directional data affected by measurement errors. *Geophysical Journal International*, **167**(2), 635–648. Cited in section(s) 3.1.3.

Kirschvink, J. L. (1980). The least-squares line and plane and the analysis of palaeomagnetic data. *Geophysical Journal of the Royal Astronomical Society*, **62**(3), 699–718. Cited in section(s) 2.1.4.

Kono, M. (1997). Distributions of paleomagnetic directions and poles. *Physics of The Earth and Planetary Interiors*, **103**(3-4), 313–327. Cited in section(s) 3.1.3 and 5.

Korte, M., Mandea, M., and Matzka, J. (2009). A historical declination curve for Munich from different data sources. *Physics of the Earth and Planetary Interiors*, **177**(3-4), 161–172. Cited in section(s) 1.

Krasa, D., Shcherbakov, V. P., Kunzmann, T., and Petersen, N. (2005). Self-reversal of remanent magnetization in basalts due to partially oxidized titanomagnetites. *Geophysical Journal International*, **162**, 115–136. Cited in section(s) B.2.

Kruiver, P. P., Langereis, C. G., Dekkers, M. J., Davies, G. R., and Smeets, R. J. (2002). The implications of non-suppressed geomagnetic secular variation during the Permo-Carboniferous Reversed Superchron. *Physics of the Earth and Planetary Interiors*, **131**(3-4), 225–235. Cited in section(s) 1 and 2.1.4.

Labrosse, S., Poirier, J.-p., and Moue, J.-l. L. (2001). The age of the inner core. *Earth and Planetary Science Letters*, **190**, 111–123. Cited in section(s) 1.

Larmor, J. (1919). Possible rotational origin of magnetic fields of sun and earth. *Elec. Rev.*, **85**, 412. Cited in section(s) 1.

Larson, R. L. (1991). Latest pulse of Earth: Evidence for a mid-Cretaceous superplume. *Geology*, **19**(6), 547. Cited in section(s) 2.1.1.

Larson, R. L. and Olson, P. (1991). Mantle plumes control magnetic reversal frequency. *Earth and Planetary Science Letters*, **107**(3-4), 437–447. Cited in section(s) 1 and 2.1.1.

Lawrence, K. P., Tauxe, L., Staudigel, H., Constable, C. G., Koppers, A., McIntosh, W., and Johnson, C. L. (2009). Paleomagnetic field properties at high southern latitude. *Geochemistry Geophysics Geosystems*, **10**(1). Cited in section(s) 3.1.1.

Lee, S. (1983). *A study of the time-averaged paleomagnetic field for the last 195 million years*. Dissertation, Australian National University. Cited in section(s) 2.1.1, 2.1.4, 2.1.4, and 2.1.4.

Leonhardt, R. (2004). Analyzing absolute paleointensity determinations: Acceptance criteria and the software ThellierTool4.0. *Geochemistry Geophysics Geosystems*, **5**(12), 1–11. Cited in section(s) 4.1.3, 4.1.3, and 4.1.

Linder, J. and Gilder, S. A. (2011). Geomagnetic secular variation recorded by sediments deposited during the Cretaceous normal superchron at low latitude. *Physics of the Earth and Planetary Interiors*, **187**(3-4), 245–260. Cited in section(s) 2.1, 4.1.1, and 4.1.5.

Linder, J. M. and Gilder, S. A. (2012). Latitude dependency of the geomagnetic secular variation S parameter: A mathematical artifact. *Geophysical Reseach Letters*, **39**, L02308. Cited in section(s) 3.1 and 3.2.

Loper, D. E. and McCartney, K. (1986). Mantle plumes and the periodicity of magnetic field reversals. *Geophysical Research Letters*, **13**(13), 1525. Cited in section(s) 1 and 2.1.1.

Luzieux, L. (2007). *Origin and late Cretaceous-Tertiary evolution of the Ecuadorian Forearc*. Dissertation. Cited in section(s) 4.1.2, 4.1.2, 4.1.2, 4.1, 4.1.2, and B.

Luzieux, L., Heller, F., Spikings, R., Vallejo, C., and Winkler, W. (2006). Origin and Cretaceous tectonic history of the coastal Ecuadorian forearc between 1N and 3S: Paleomagnetic, radiometric and fossil evidence. *Earth and Planetary Science Letters*, **249**(3-4), 400–414. Cited in section(s) 4.1.4, 4.1.4, 4.3, and 4.6.

Macellari, C. E. (1988). Cretaceous paleogeography and depositional cycles of western South America. *Journal of South American Earth Sciences*, **1**(4), 373–418. Cited in section(s) 2.1.2 and 2.1.2.

McElhinny, M. W. and Merrill, R. T. (1975). Geomagnetic secular variation over the past 5 m.y. *Reviews of Geophysics*, **13**(5), 687. Cited in section(s) 1.1, 2.1.1, and 3.1.1.

McFadden, P. L. and Lowes, F. J. (1981). The discrimination of mean directions drawn from Fisher distributions. *Geophysical Journal International*, **67**(1), 19–33. Cited in section(s) 2.1.3.

McFadden, P. L. and McElhinny, M. W. (1984). A physical model for palaeosecular variation. *Geophysical Journal of the Royal Astronomical Society*, **78**(3), 809–830. Cited in section(s) 2.1.1 and 3.1.1.

McFadden, P. L. and Merrill, R. (1986). Geodynamo energy source constraints from palaeomagnetic data. *Physics of the Earth and Planetary Interiors*, **43**(1), 22–33. Cited in section(s) 1 and 2.1.1.

McFadden, P. L. and Merrill, R. T. (1995). Fundamental transitions in the geodynamo as suggested by paleomagnetic data. *Physics of the Earth and Planetary Interiors*, **91**(4), 253–260. Cited in section(s) 2.1.1.

McFadden, P. L. and Merrill, R. T. (1997). Asymmetry in the reversal rate before and after the Cretaceous Normal Polarity Superchron. *Earth and Planetary Science Letters*, **149**(1-4), 43–47. Cited in section(s) 2.1.1.

McFadden, P. L., Merrill, R. T., and McElhinny, M. W. (1988). Dipole/quadrupole family modeling of paleosecular variation. *Journal of Geophysical Research*, **93**(B10), 11583. Cited in section(s) 1, 1.1, 2.1.1, 3.1.1, 3.1.3, and 5.

McFadden, P. L., Merrill, R. T., McElhinny, M. W., and Lee, S. (1991). Reversals of the Earth's Magnetic Field and Temporal Variations of the Dynamo

Families. *Journal of Geophysical Research-Solid Earth*, **96**(B3), 3923–3933. Cited in section(s) 1, 1.2, 2.1.1, 2.1.4, 2.1.4, 2.13, 2.1.5, 2.2, 2.3, 3.1.1, 3.1.3, 3.3, and 5.

Menning, M., Alekseev, A., Chuvashov, B., Davydov, V., Devuyst, F.-X., Forke, H., Grunt, T., Hance, L., Heckel, P., Izokh, N., Jin, Y.-G., Jones, P., Kotlyar, G., Kozur, H., Nemyrovska, T., Schneider, J., Wang, X.-D., Weddige, K., Weyer, D., and Work, D. (2006). Global time scale and regional stratigraphic reference scales of Central and West Europe, East Europe, Tethys, South China, and North America as used in the DevonianCarboniferousPermian Correlation Chart 2003 (DCP 2003). *Palaeogeography, Palaeoclimatology, Palaeoecology*, **240**(1-2), 318–372. Cited in section(s) 2.1.1.

Mitouard, P., Kissel, C., and Laj, C. (1990). Post-Oligocene rotations in southern Ecuador and northern Peru and the formation of the Huancabamba deflection in the Andean Cordillera. *Earth and Planetary Science Letters*, **98**(3-4), 329–339. Cited in section(s) 2.1.3.

Mitouard, P., Laj, C., Mourier, T., and Kissel, C. (1992). Paleomagnetic study of an arcuate fold belt developed on a marginal orogen: The Cajamarca deflection, northern Peru. *Earth and Planetary Science Letters*, **112**(1-4), 41–52. Cited in section(s) 2.1.3.

Mourier, T., Laj, C., Mégard, F., Roperch, P., Mitouard, P., and Farfan Medrano, A. (1988a). An accreted continental terrane in northwestern Peru. *Earth and Planetary Science Letters*, **88**(1-2), 182–192. Cited in section(s) 4.1.2.

Mourier, T., Bengtson, P., Bonhomme, M., Buge, E., Cappetta, H., Crochet, J.-Y. Y., Feist, M., Hirsch, K. F., Jaillard, E., Laubacher, G., Lefranc, J. P., Moullade, M., Noblet, C., Pons, D., Rey, J., Sige, B., Tambareau, Y., Taquet, P., and Others (1988b). The Upper Cretaceous - Lower Tertiary marine to continental transition in the Bagua basin, northern Peru. *Newsletter on Stratigraphy*, **19**(3), 143–177. Cited in section(s) 2.1.2 and B.

Noble, D. C. and McKee, E. H. (1977). Comment on paper by Barazangi, M and Isacks, B. L. ,1976: Spatial distribution of earthquakes and subduction of the Nazca plate beneath South America. *Geology*, **5**, 576–578. Cited in section(s) 2.1.3.

Noble, D. C., McKee, E. H., Mourier, T., and Megard, F. (1990). Cenozoic stratigraphy, magmatic activity, compressive deformation, and uplift in northern Peru. *Geol. Soc. Am. Bull.*, **102**, 1105–1113. Cited in section(s) 2.1.3.

Opdyke, N. D., Hall, M., Mejia, V., Huang, K., and Foster, D. a. (2006). Time-averaged field at the equator: Results from Ecuador. *Geochemistry Geophysics Geosystems*, **7**(11), 1–16. Cited in section(s) 3.1.1.

Opdyke, N. D., Kent, D. V., Huang, K., Foster, D. a., and Patel, J. P. (2010). Equatorial paleomagnetic time-averaged field results from 05 Ma lavas from Kenya and the latitudinal variation of angular dispersion. *Geochemistry Geophysics Geosystems*, **11**(5), 1–20. Cited in section(s) 3.1.1.

Özdemir, O. and O'Reilly, W. (1982). Magnetic hysteresis properties of synthetic monodomain titanomaghemites. *Earth and Planetary Science Letters*, **57**, 437–447. Cited in section(s) 4.1.3.

Parés, J. M., van der Pluijm, B. A., and Dinares-Turell, J. (1999). Evolution of magnetic fabrics during incipient deformation of mudrocks (Pyrenees, northern Spain). *Tectonophysics*, **307**(1-2), 1–14. Cited in section(s) 2.1.3.

Pavlov, V. and Gallet, Y. (2005). A third superchron during the Early Paleozoic. *Episodes*, **28**(002), 78–84. Cited in section(s) 1, 2.1.1, and 2.1.1.

Petersen, N. and Vali, H. (1987). Observation of shrinkage cracks in ocean floor titanomagnetites. *Physics of the Earth and Planetary Interiors*, **46**, 197–205. Cited in section(s) 4.1.3.

Pétrélis, F., Fauve, S., Dormy, E., and Valet, J.-P. (2009). Simple Mechanism for Reversals of Earths Magnetic Field. *Physical Review Letters*, **102**(14), 1–4. Cited in section(s) 2.1.4.

Pick, T. and Tauxe, L. (1993). Geomagnetic paleointensities during the Cretaceous normal superchron measured using submarine basaltic glass. *Nature*, **366**, 238 —- 242. Cited in section(s) 4.7 and 4.1.4.

Pilatsig, L., Gordon, D., Palacios, O., and Sanchez, J. (2008). Mapa Geologico binacional region sur del Ecuador y norte del Peru - Mapa en revision final. Cited in section(s) 2.2 and 4.1.

Pindell, J. L. and Kennan, L. (2009). Tectonic evolution of the Gulf of Mexico, Caribbean and northern South America in the mantle reference frame: an update. *Geological Society, London, Special Publications*, **328**(1), 1–55. Cited in section(s) 4.1.2.

Reynolds, R. L., Tuttle, M. L., Rice, C. A., Fishman, N. S., Karachewski, J. A., and Sherman, D. M. (1994). Magnetization and geochemistry of greigite-bearing Cretaceous strata, North Slope Basin, Alaska. *American Journal of Science*, **294**(4), 485–528. Cited in section(s) 2.1.3.

Reynolds, R. R. L., Rosenbaum, J. J. G., van Metre, P., Tuttle, M. L., Callender, E., and Goldin, A. (1999). Greigite (Fe3S4) as an indicator of droughtThe 19121994 sediment magnetic record from White Rock Lake, Dallas, Texas, USA. *Journal of Paleolimnology*, **21**(2), 193–206. Cited in section(s) 2.1.3.

Riisager, J., Perrin, M., Riisager, P., and Vandamme, D. (2001). Paleomagnetic results and paleointensity of Late Cretaceous Madagascan basalt. *Journal of African Earth Sciences*, **32**(3), 503–518. Cited in section(s) 2.1.1.

Robert, E. (2001). *La transgression albienne dans le Bassin Andin (Pérou): Biostratigraphie, paléontologie (Ammonites) et stratigraphie séquentielle.* Dissertation, Université Paul Sabatier Toulouse III. Cited in section(s) 2.1.2, 2.1.2, and 2.3.

Robert, E., Bulot, L. G., Jaillard, E., and Peybernès, B. (2003). Revision bioestratigrafica del Albiano inferior a superior basal en la Cuenca Andina peruana (Peru central y norte). *Boletin de la Sociedad geologica del Per{ù}*, **95**, 59–74. Cited in section(s) 2.1.2.

Roberts, A. P. (1995). Magnetic properties of sedimentary greigite (Fe3S4). *Earth and Planetary Science Letters*, **134**(3-4), 227–236. Cited in section(s) 2.1.3.

Roberts, A. P. (2005). Assessing the timing of greigite formation and the reliability of the Upper Olduvai polarity transition record from the Crostolo River, Italy. *Geophysical Research Letters*, **32**(5), 10–13. Cited in section(s) 2.1.3 and 2.1.3.

Roberts, A. P. and Weaver, R. (2005). Multiple mechanisms of remagnetization involving sedimentary greigite (Fe3S4). *Earth and Planetary Science Letters*, **231**, 263–277. Cited in section(s) 2.1.3.

Roberts, A. P., Reynolds, R. L., Verosub, K. L., and Adam, D. P. (1996). Environmental magnetic implications of greigite (Fe3S4) formation in a 3 m.y. lake sediment record from Butte Valley, northern California. *Geophysical Research Letters*, **23**(20), 2859–2862. Cited in section(s) 2.1.3.

Roberts, A. P., Chang, L., Rowan, C. J., Horng, C.-S., and Florindo, F. (2011). Magnetic properties of sedimentary greigite (Fe3S4): an update. *Reviews of Geophysics*, **49**(2010RG000336), RG1002. Cited in section(s) 2.1.3.

Roberts, P. H. and Stix, M. (1972). alpha-Effect Dynamos, by the Bullard-Gellman Formalism. *Astronomy and Astrophysics*, **18**(18), 453–466. Cited in section(s) 2.1.1 and 3.1.1.

Roperch, P., Megard, F., Laj, C., Mourier, T., Clube, T., and Noblet, C. (1987). Rotated Oceanic Blocks in Western Ecuador. *Geophysical Reseach Letters*, **14**(5), 558–561. Cited in section(s) 4.1.4, 4.3, B, B, and B.

Rousse, S., Gilder, S., Farber, D., McNulty, B., Patriat, P., Torres, V., and Sempere, T. (2003). Paleomagnetic tracking of mountain building in the Peruvian Andes since 10 Ma. *Tectonics*, **22**(5), 1048. Cited in section(s) 2.1.2 and 2.1.3.

Sébrier, M., Lavenu, A., Fornari, M., and Soulas, J.-P. (1988). Tectonics and uplift in the central Andes (Peru, Bolivia and Northern Chile) from Eocene to Present. *Geodynamique*, **3**, 85—-106. Cited in section(s) 2.1.3.

Shcherbakov, V. and Fabian, K. (2012). The geodynamo as a random walker: a view on reversal statistics. *Journal of Geophysical Research*, **in press**. Cited in section(s) 5.

Shi, R., Hill, M. J., Zhu, R., He, H., and Shaw, J. (2005). 40 Ar / 39 Ar dating and preliminary paleointensity determination on a single lava flow from Chifeng , Inner Mongolia. *Physics of the Earth and Planetary Interiors*, **152**, 78–89. Cited in section(s) 4.7 and 4.1.4.

Sinton, C., Duncan, R., Storey, M., Lewis, J., and Estrada, J. (1998). An oceanic flood basalt province within the Caribbean plate. *Earth and Planetary Science Letters*, **155**(3-4), 221–235. Cited in section(s) 4.1.2.

Smirnov, A. V., Tarduno, J. a., and a.D. Evans, D. (2011). Evolving core conditions ca. 2 billion years ago detected by paleosecular variation. *Physics of the Earth and Planetary Interiors*. Cited in section(s) 3.1.1.

Snedecor, G. and Cochran, W. (1989). *Statistical methods*. Blackwell Publishers, Oxford. Cited in section(s) 3.2.

Stahel, W. A. (2009). *Statistische Datenanalyse*. Vieweb+Teubner. Cited in section(s) 3.2.

Suk, D., Peacor, D. R., and der Voo, R. (1990). Replacement of pyrite framboids by magnetite in limestone and implications for paleomagnetism. *Nature*, **345**, 611–613. Cited in section(s) 2.1.3.

Tanaka, H. and Kono, M. (2002). Paleointensities from a Cretaceous basalt platform in Inner Mongolia , northeastern China. *Physics of the Earth and Planetary Interiors*, **133**, 147–157. Cited in section(s) 4.7 and 4.1.4.

Tarduno, J. A., Lowrie, W., Sliter, W. V., Bralower, T. J., and Heller, F. (1992). Reversed polarity characteristic magnetizations in the Albian Contessa section, Umbrian apennines, Italy: Implications for the existence of a Mid-Cretaceous mixed polarity interval. *Journal of Geophysical Research*, **97**(B1), 241–271. Cited in section(s) 2.1.3.

Tarduno, J. a., Cottrell, R. D., and Smirnov, A. V. (2001). High geomagnetic intensity during the mid-Cretaceous from Thellier analyses of single plagioclase crystals. *Science*, **291**(5509), 1779–83. Cited in section(s) 1, 4.7, and 4.1.4.

Tarduno, J. a., Cottrell, R. D., and Smirnov, A. V. (2002). The Cretaceous superchron geodynamo: observations near the tangent cylinder. *Proceedings of the National Academy of Sciences of the United States of America*, **99**(22), 14020–5. Cited in section(s) 2.1.1, 2.2, 4.7, and 4.1.4.

Tarduno, J. A. J. (1990). Brief reversed polarity interval during the Cretaceous normal polarity superchron. *Geology*, **18**(8), 683. Cited in section(s) 2.1.3.

Tauxe, L. (2005). *Lectures in Paleomagnetism*. Cited in section(s) 3.2 and 3.2.

Tauxe, L. and Kent, D. (2004). A simplified statistical model for the geomagnetic field and the detection of shallow bias in paleomagnetic inclinations: Was the ancient magnetic field dipolar. In J. Channell, D. V. Kent, W. Lowrie, and J. G. Meert, Herausgeber, *Timescales of the Paleomagnetic Field*, Ausgabe 145, Seiten 101–116. AGU Book, Washington, geophysica edition. Cited in section(s) 3.1.3 and 5.

Tauxe, L. and Staudigel, H. (2004). Strength of the geomagnetic field in the Cretaceous Normal Superchron: New data from submarine basaltic glass of the Troodos Ophiolite. *Geochemistry Geophysics Geosystems*, **5**(2). Cited in section(s) 4.7 and 4.1.4.

Thellier, E. and Thellier, O. (1959). Sur l'intensité du champ magnétique terrestre dans le passé historique et géologique. *Ann. Geophys.*, **15**, 285 – 376. Cited in section(s) 4.1.3.

Tric, E., Laj, C., Jehanno, C., Valet, J.-P., Kissel, C., Alain, M., and Iccarino, S. (1991). High-resolution record of the Upper Olduvai transition from Po Valley (Italy) sediments: support for dipolar transition geometry. *Physics of the Earth and Planetary Interiors*, **65**(3-5), 319–336. Cited in section(s) 2.1.3.

Tsunakawa, H., Wakabayashi, K.-i., Mochizuki, N., Yamamoto, Y., Ishizaka, K., Hirata, T., Takahashi, F., and Seita, K. (2009). Paleointensity study of the middle Cretaceous Iritono granite in northeast Japan: Implication for high field intensity of the Cretaceous normal superchron. *Physics of the Earth and Planetary Interiors*, **176**(3-4), 235–242. Cited in section(s) 4.7 and 4.1.4.

Tudryn, A. and Tucholka, P. (2004). Magnetic monitoring of thermal alteration for natural pyrite and greigite. *Acta Geophysica Polonica*, **52**(4), 509–520. Cited in section(s) 2.1.3.

Vallejo Cruz, C. F. (2007). *Evolution of the Western Cordillera in the Andes of Ecuador (Late Cretaceous-Paleogene)*. Dissertation. Cited in section(s) 4.1.2, 4.1, 4.1.2, and B.

Van der Voo, R. and Torsvik, T. H. (2001). Evidence for late Paleozoic and Mesozoic non-dipole fields provides an explanation for the Pangea reconstruction problems. *Earth and Planetary Science Letters*, **187**(1-2), 71–81. Cited in section(s) 2.2.

Vandamme, D. (1994). A new method to determine paleosecular variation. *Physics of The Earth and Planetary Interiors*, **85**(1-2), 131–142. Cited in section(s) 2.1.4.

Vandenberg, J., Klootwijk, C. T., and Wonders, A. A. H. (1978). Late Mesozoic and Cenozoic movements of the Italian Peninsula; further paleomagnetic data from the Umbrian Sequence. *Bulletin of the Geological Society of America*, **89**, 133–150. Cited in section(s) 2.1 and 2.1.3.

Vestine, E. (1954). The earth's core. *Tran. Amer. Geophys. Union*, **35**, 63–72. Cited in section(s) 1.

Watkins, N. D. and Walker, G. P. L. (1977). Magnetostratigraphy of eastern Iceland. *American Journal of Science*, **277**(5), 513. Cited in section(s) 2.1.4.

Wicht, J. (2005). Palaeomagnetic interpretation of dynamo simulations. *Geophysical Journal International*, **162**(2), 371–380. Cited in section(s) 2.1.4 and 2.1.4.

Wignall, P. B., Newton, R., and Brookfield, M. E. (2005). Pyrite framboid evidence for oxygen-poor deposition during the Permian-Triassic crisis in Kashmir. *Paleogeography, Paleoclimatology, Paleoecology*, **216**, 183–188. Cited in section(s) 2.1.3.

Wilson, J. J. (1963). Cretaceous stratigraphy of central Andes of Peru. *Assoc. Petroleum Geologists Bull*, **47**(1), 1–34. Cited in section(s) 2.1.2.

Wilson, R. L. (1959). Remanent magnetism of late secondary and early tertiary british rocks. *Philosophical Magazine*, **4**(42), 750–755. Cited in section(s) 3.2.

Zhao, X., Riisager, P., Riisager, J., Draeger, U., Coe, R. S., and Zheng, Z. (2004). New palaeointensity results from Cretaceous basalt of Inner Mongolia , China. *Physics of the Earth and Planetary Interiors*, **141**, 131–140. Cited in section(s) 4.7 and 4.1.4.

Zhu, R., Pan, Y., Shaw, J., Li, D., and Li, Q. (2001). Geomagnetic palaeointensity just prior to the Cretaceous normal superchron. *Physics of the Earth and Planetary Interiors*, **128**, 207–222. Cited in section(s) 4.7 and 4.1.4.

Zhu, R., Hoffman, K. A., Pan, Y., Shi, R., and Li, D. (2003). Evidence for weak geomagnetic field intensity prior to the Cretaceous normal superchron. *Physics of the Earth and Planetary Interiors*, **136**, 187–199. Cited in section(s) 4.7 and 4.1.4.

Zhu, R., Hoffman, K. A., Nomade, S., Renne, P. R., Shi, R., Pan, Y., and Shi, G. (2004). Geomagnetic paleointensity and direct age determination of the ISEA (M0r?) chron. *Earth and Planetary Science Letters*, **217**(3-4), 285–295. Cited in section(s) 2.1.3, 4.7, and 4.1.4.

Acknowledgements

Beside all the people who were already thanked in the particular chapters I would like to express my gratitude to some special collegues who accompanied me during my time as a Phd student at the LMU Munich. Stuart Gilder is thanked for the exciting and funny field trips to Peru and Ecuador and for the open-door he had for his PhD students. During my Phd project I could discuss anything anytime with Ramon Egli, who has the gift to explain difficult topics on every needed level. Help and support of Roman Leonhardt and Annika Ferk with questions regarding paleointensities are greatly appreciated. My gratitude goes to Tobias Megies and Simon Kremers for the patience with a Python learning paleomagnetist. The detailed proof-reading of Ramon Egli, Rob Coe, Mike Volk, Annika Ferk, Jochen Kollofrath and Andre Horbach was very much appreciated. Our yellow 10-Euro coffee machine is acknowledged for reliably preparing coffee at least twice a day for more than 4 years now.

Thanks are also expressed to all the people who feel forgotten in these last-minute acknowledgements. Danke.